Expanding the Organometallic Chemistry of 4d and 4f Arene Metal Complexes

Christopher Bamforth

A thesis submitted in partial fulfilment of the requirements for the Doctorate in Philosophy degree in Chemistry

Department of Chemistry and Biomolecular Sciences

Faculty of Science

University of Ottawa

Abstract

Organometallic chemistry is a discipline which grants sophisticated control over metal ions' electronic properties, facilitating the design of materials with tailorable physical properties. **Chapter 1** gives an overview of organometallic chemistry, with a focus on transition metal and lanthanide π-bonded systems, and an introduction to ligand Field theory and molecular magnetism. In **Chapter 2**, the magnetic and fluorescent characterisation of the dysprosium (III) piano-stool complex, [DyCp*$(BH_4)_2$(THF)], and its borodeuteride congener, [DyCp*$(BD_4)_2$(THF)], are described. Analysis of these results shows that the relatively low-symmetry complexes show slow magnetic relaxation *via* a through-barrier mechanism, because of the strong crystal field imposed by the Cp* Ligand. Computational methods were utilised to show that the bonding in these complexes has significant covalent character, contrary to the classical view of 4f bonding. In **Chapter 3**, we discuss the organometallic chemistry of palladium cyclobutadiene complexes, and report the synthesis and structural characterisation of the zerovalent palladium metallocene [$Pd(C_4Ph_4)_2$], the first structurally-authenticated tetraphenylcyclobutadiene metallocene. In **Chapter 4**, we discuss the use of asymmetric alkynes to synthesise cis and trans isomers of bisphenylbis(trimethylsilyl)cyclobutadienediide (Cb), for which the organometallic chemistry is hitherto unreported. The reactivity of these salts with lanthanide ions was explored for the first time. We report two structurally authenticated coordination polymers, varying by ratio of Li:BH_4 ions within the lattice. In **Chapter 5**, we discuss the synthesis of the dysprosium (III) 9-borabicyclononane hydroborate THF solvate, [$K(THF)_6$][$Dy(HBBN)_2(THF)_2$], and its reactivity with the aforementioned lithium cyclobutadienediide salts. We report two complexes, [$Dy(HBBN)_2$(THF)(μ-Cb^{trans})Li(THF)]. [$Dy(HBBN)_2$(THF)(μ-Cb^{trans})$K(THF)]_4$ and their structural investigation. **Chapter 6** describes the exploratory chemistry of the Cb salts described previously for the future development of multinuclear SMMs and perspectives on the organometallic chemistry presented.

Dedication

To

my mother and father, Caroline and Alistair Bamforth,

and my siblings, Ailish, Rebecca, and Matthew.

In recognition of your endless support and love.

For perspective:

"It is perfectly true, as the philosophers say, that life must be understood backwards. But they forget the other proposition, that it must be lived forwards."
"Journals - IV", Soren Kierkegaard, 1843.

And inspiration:

"Bear in mind that the wonderful things you learn in your schools are the work of many generations. All this is put in your hands as your inheritance in order that you may receive it, honor it, add to it, and one day faithfully hand it on to your children."

"The world as I see it", Albert Einstein, 1934.

Acknowledgements

First and foremost, I grateful to my supervisor, Prof. Muralee Murugesu, for giving me the opportunity to work and collaborate with such a diverse group of passionate researchers.

I'm grateful as well for having so many supportive and passionate colleagues in the Murugesu family. Katie & Dylan, your love of organometallic chemistry will always inspire me, and our pre-covid trips to Gatineau Park were a highlight of the year in Ottawa. Pink lake again? Quack. Paul you've been a brother since my first week in Canada. I can still remember chatting over Wilco late in the lab during my first Canadian winter. You've been a real support, and I wish you and Ellen all the best. Niki, thanks for having each other's backs through such strange times, the boxes will be happy that you've been taking good care of them. Roberto, we had a great time taking care of the small box (and its unquenchable thirst for solvents). I'm excited to see where your passion for 4f and main group organometallic chemistry takes you, I'm sure it'll be interesting! Darren, I'll miss being bay buddies with you. Alex, you've been a great friend here in Ottawa, and I've learned so much from our chats by the loading bay about crystallography, chemistry, and Greek cuisine. Efcharisto buddy!

To the many visiting researchers who joined the Murugesu group: Drs. Rolando Caraballo, German Gomez, and Mariana Hamer, thanks for bringing your joy and love of science to the lab. The many visiting students, Dr Qi Sun, Wen Xin Wu, Daniel Martins, Linda Zuckerman, Fanny Thorimbert and Candice Cottrez, it was a pleasure to welcome you to Canada, and I wish all the best in your studies!

Thank you also to all the support and facilities staff at uOttawa, who kept our labs running in the midst of a pandemic. Special thanks go to those at the science stores, Claude, Max, and André, for supplying us through strikes and lockdowns, and Dr. Wendy Pell and the other staff at the teaching labs for working so hard so we could teach safely.

A final thanks goes to all the members of the grad student volleyball team. La Maison may have shut down, but the spirit will live on.

Table of Contents

Table of Figures:

Table of Schemes

Table of Tables

Table of Abbreviations

2.2.2-Crypt = [2.2.2]Cryptand / 4,7,13,16,21,24-hexaoxa-1,10-diazabicyclo[8.8.8]hexacosane.

12-C-4 = 12-Crown-4 ether / 1,4,7,10-tetraoxacyclododecane.

15-C-5 = 15-Crown-5 ether / 1,4,7,10,13-pentaoxacyclopentadecane.

18-C-6= 18-Crown-6 ether /1,4,7,10,13,16-hexaoxacyclooctadecane.

9-BBN = 9-borabicyclo[3.3.1]nonane, (HBC_8H_{15}).

a **=** Crystallographic axis.

AC = Alternating Current.

b = Crystallographic axis.

B = CF parameter.

BAr^F = Tetrakis[3,5-bis(trifluoromethyl)phenyl]borate anion, $[\{3,5\text{-}(CF_3)_2C_6H_3\}_4B]^-$.

BD_4 Borodeuteride/tetradeuteroborate anion.

BF_4 = Tetrafluoroborate anion.

BH_4 = Borohydride/tetrahydroborate anion.

c **=** Crystallographic axis.

C_7H_7 = Cycloheptatrienyl cation.

CASSCF = Complete Active Space Self-Consistent Field.

Cb = 1,3-cyclobutadiene.

Cb^{2-} = Cyclobutadienediide.

Cb’’’’ = Tetrakis(trimethylsilyl)cyclobutadiene.

Cb^{Ph4} = Tetraphenylcyclobutadiene.

Cb^{Cis} = 1,2-bispheny-3,4-bis(trimethylsilyl)cyclobutadiene.

Cb^{trans} = 1,3-bisphenyl-3,4-bis(trimethylsilyl)cyclobutadiene.

CF = Crystal Field.

Cg = Arene crystallographic centroid.

cm^{-1} = Wavenumber.

CO = Carbon monoxide.

COT = Cyclooctatetraene.

COT^{2-} = Cyclooctatetraenide dianion.

COT'' = 1,3-bis(trimethylsilyl)cyclooctatetraenide dianion.

Cp = Cyclopentadienide anion.

Cp* = 1,2,3,4,5-pentamethylcyclopentadienide anion.

Cp'' = 1,3-bis(trimethylsilyl)cyclopentadienide anion.

Cp^{ttt} = 1,3,5- tris(*tert*-butyl)cyclopentadienide anion.

Cp^{ipr5} = 1,2,3,4,5-penta(*iso*propyl)cyclopentadienide anion.

CV = Cyclic Voltammetry.

d_e = Distance from external atom to Hirshfeld surface.

d_i = Distance from internal atom to Hirshfeld surface.

d_{norm} = Normalised contact distance for Hirshfeld surface.

DBA = Dibenzylideneacetone.

DC = Direct Current.

DFT = Density Functional Theory.

DME = 1,2-dimethoxyethane.

^{t}bu-DPOT = 1,8-bis(3,5-di-tert-butyl)phenyl-1,3,5,7-octatetraene.

eV = Electronvolt.

EPR = Electron Paramagnetic Resonance.

FC = Field-Cooled.

FTIR = Fourier-Transform Infrared Spectroscopy.

g = g-factor.

g_z = Crystal-Field magnetic anisotropy tensor.

***h* =** Planck's constant.

H = Magnetic field.

HBBN = 9-borabicyclononane hydroborate anion, $(H_2BC_8H_{14})^-$.

HCp = 1,3-cyclopentadiene .

HOMO = Highest-Occupied Molecular Orbital.

J = Total angular momentum.

K = Kelvin.

K_B = Boltzmann's constant.

KD = Kramer's Doublet.

L = Total orbital angular momentum.

LF = Ligand Field.

Ln = Lanthanide/Lanthanoid metal.

LUMO = Lowest-Unoccupied Molecular Orbital.

M = Magnetisation.

MCD = Magnetic circular dichroism.

***m_J* =** Crystal Field microstates/ Stark sublevels for Lanthanide ions.

MO = Molecular Orbital.

n = Principal quantum number.

n = Raman exponent.

N" = Hexamethyldisilylamide, $(HN(SiMe_3)_2)$.

NMR = Nuclear Magnetic Resonance.

Oe = Oersted.

Ph = Phenyl (C_6H_5).

RASSI = Restricted Active Space State Interaction.

REE = Rare Earth Element.

S = Total spin angular momentum.

SALC = Symmetry adapted linear combination.

SCE = Saturated calomel electrode.

SC-XRD = Single-Crystal X-ray Diffraction.

SCM = Single-chain magnet.

SIM = Single-ion magnet.

SMM = Single-molecule magnet.

SQUID = Superconducting quantum interference device.

***T* =** Temperature.

T_B = Blocking temperature.

T = Tesla.

THF = Tetrahydrofuran.

TM = Transition Metal.

TMEDA = Tetramethylethylenediamine.

TMS = Trimethylsilyl (SiC_3H_9).

V = Volt.

VO = Valence orbital.

QTM = Quantum tunnelling of the magnetisation.

ZFC = Zero-Field-Cooled.

Symbols:

Å = Angstrom.

α **=** Debye distribution factor.

α = Unit cell angle.

β = Unit cell angle.

γ = Unit cell angle.

η = Hapticity.

κ **=** Denticity.

ν = Frequency.

μ **=** Bridging coordination.

μ_B = Bohr magneton.

τ = Relaxation time.

τ^{-1} = Relaxation rate.

τ_0 = Arrhenius preexponential factor/ “attempt time”.

χ = Magnetic susceptibility.

χ_D = Diamagnetic susceptibility.

χ_P = Paramagnetic susceptibility.

χ_S = Adiabatic/equilibrium susceptibility.

χ_T = Isothermal/static susceptibility.

χ_P = Paramagnetic susceptibility.

χ' = In-phase susceptibility.

χ'' = Out-of-phase susceptibility.

ψ = Wavefunction.

Contribution Statement

I performed all the experimental work described in this thesis, including synthesis, characterisation, and analysis. I collected all of the single crystal X-ray data and solved and refined the structures in Chapters 3 and 5. The structures in Chapters 2 and 4 were solved and refined by Dr Alexandros Kitos. *ab initio* and DFT calculations in Chapter 2 were contributed by Dr. Liviu Ungur of NUS Singapore. Emission fluorimetry in Chapter 2 was measured and plotted by Dr. Diogo Alves Galico. Finally, all of this work was made possible by the supervision and support of Dr. Muralee Murugesu.

Chapter 1: You Can Have Your π and Eat It Too; Organometallic Chemistry and Arene Metal Complexes

1.1 Opening Remarks:

There is no doubt that our modern way of life is beholden to the supply of advanced materials and critical metals.[1,2] From our phones, cars, computers to energy, we are consuming not only more metals, but a more diverse range than ever before to support our increasing technological development. Indeed, a modern "smartphone" is estimated to contain at least 63 different metals in its electronic and optical components,[3] and each Nissan Leaf hybrid car for example, contains approximately two kilograms of Rare Earth permanent magnets in its motor.[4] However, a number of challenges have arisen through our use of critical metals which require a paradigm shift in materials chemistry to enable our continued technological development.

Noble metal catalysts have become a cornerstone of synthetic organic chemistry, with widespread use in the synthesis of pharmaceuticals[5], fine chemicals[6], and industrial polymers[7]. Central to this is low-valent palladium, which is utilised in some of the most well-studied C-C and C-N bond forming process, such as the Suzuki[8], Heck[9], Negishi[10], and Buchwald-Hartwig[11] cross-coupling reactions, amongst others.[7] Indeed, the enduring influence of these catalytic process can be seen in the 2010 Nobel Prize in Chemistry awarded to Heck, Negishi, and Suzuki for contributions to the aforementioned discoveries.[12,13] However, the sustainable use of noble metal catalysts has come into question when recognising the increasing criticality of these metals worldwide.[14–17]

The Lanthanide, or Lanthanoid group, make up the 15 metals on the Periodic Table from lanthanum to lutetium, and, with the d-block metals yttrium and scandium, make the Rare Earth Elements (REE) group. REEs have a number of diverse applications in the modern world from lasers, optical lenses, polymerisation catalysts, to, most notably, permanent magnets.[18–22] However their global supply has been an international concern since the "Rare Earth crisis" of the 2010s, when the first analyses of REE criticality were performed in response to fears that monopolistic supply and export restrictions would lead to global shortages.[23,24] The EU has recently estimated that Rare Earth Element demand may increase by tenfold before 2050;[25] and the U.S Department of Energy[26], and International Energy Agency[27] have declared shortages of Rare Earth Elements as a result of their ever increasing demand. This has created a global impetus to develop atom-efficient lanthanide materials, and organometallic chemistry represents a powerful tool to this end.

1.2 Organometallic Chemistry Overview:

Organometallic chemistry focuses on the synthesis and electronic characterisation of Main Group, Transition Metal, Lanthanide, and Actinide complexes with designed organic ligands. Organometallic chemistry differs from traditional Werner-type coordination chemistry as it is utilises π, or strong σ donor ligands, such as aromatic rings, scorpionates, heavy p-block elements, and carbenes.[28–32] Organometallic chemistry allows for unique metal-ligand interactions that are not seen in other areas of chemistry, making it a powerful tool for structure-property investigations. For these reasons, organometallic chemistry has been explored in areas such as drug design,[33] therapeautics,[34] catalysis[35], charge-storage batteries[36], and small molecule activation. Additionally, organometallic chemistry has played a key role in our current understanding of metal-ligand interactions, especially in the f-block,

because the wide array of ligand strengths grants access to bonding motifs not seen in any other area of chemistry.[37–40]

1.2.1 Understanding Metal-ligand Interactions:

A detailed understanding of metal-ligand interactions is necessary to understand the physical properties of materials and allows their fine-tuning through synthetic organometallic chemistry. Crystal field (CF) theory was the first model developed which can account for the spectroscopic properties of transition metal complexes. Fundamentally, it describes the splitting of the metal n*d* valence electrons' degeneracy (where n = the principal quantum number) by a sphere of anionic point charges, representing the ligands in its coordination sphere. The type of splitting is determined by the point group symmetry of the metal centre (octahedral, tetrahedral, etc.). The splitting and occupancy of the resultant orbitals can explain some of the spectroscopic properties of transition metal complexes.[28]

Crystal-field theory was further refined by describing the metal-ligand interactions in terms of their respective Molecular Orbitals (MOs) using quantum mechanics. By taking into consideration the metal and ligand orbital energies and symmetries, a new model which better represents the bonding in metal complexes, named Ligand Field (LF) theory, was developed. In this model ligands are organised in terms of their interaction strength, with strong-field ligands capable of metal-to-ligand π-backbonding (CO, CN^-) producing larger splitting energies than σ-only intermediate field (H_2O, OH^-) or weak field π-donor ligands (X^-, SCN^-). The bonding is described using symmetry adapted linear combinations (SALCs) of ligand group orbitals with the metal valence orbitals, elucidating the energy and character (bonding, non-bonding, antibonding) of the resultant MOs. By taking into consideration the orbital symmetry and energies, LF theory can account for the spectroscopic, magnetic, and hydration enthalpies of organometallic complexes well.[41]

Modern computational chemistry can describe the LF interactions in organometallic complexes utilising *ab initio* computational methods, such as Complete Active Space Self-Consistent Field (CASSCF) calculations, which agree well with experimentally derived spectra.[42–44] It is germane to note that as lanthanides are classically considered only to interact electrostatically (*vide infra*), many in the community will use the terms CF and LF interchangeably.[45]

1.2.2 Aromaticity:

Aromatic ligands are ubiquitous in organometallic chemistry, as this electronic property gives rise to electronic stability and facile tunability *via* substitution relative to their non-aromatic congeners. In traditional Kekulé systems, the presence of aromaticity can be predicted using Hückel's rules, which states that if a compound is planar, cyclic, and has continuous conjugation, then the presence of (4n+2) delocalised electrons will lead to aromatic stabilisation in the electronic ground state. A (4n) electron configuration leads to aromatic destabilisation, known as antiaromaticity.[46] For more complex polycyclic systems, Clar's rule should be invoked, however this will not be discussed further.[47] Aromaticity is based in MO theory, wherein the electronic and symmetry criteria for aromaticity give rise to a low-energy closed shell configuration, and antiaromaticity leads to higher-energy open shell states (**Fig. 1.1**). Experimental studies have corroborated the triplet ground state in tetramethylcyclobutadiene,[48] and unsubstituted cyclooctatetraene is shown to take on a deformed "tub" geometry to escape the destabilising effects of antiaromaticity.[49]

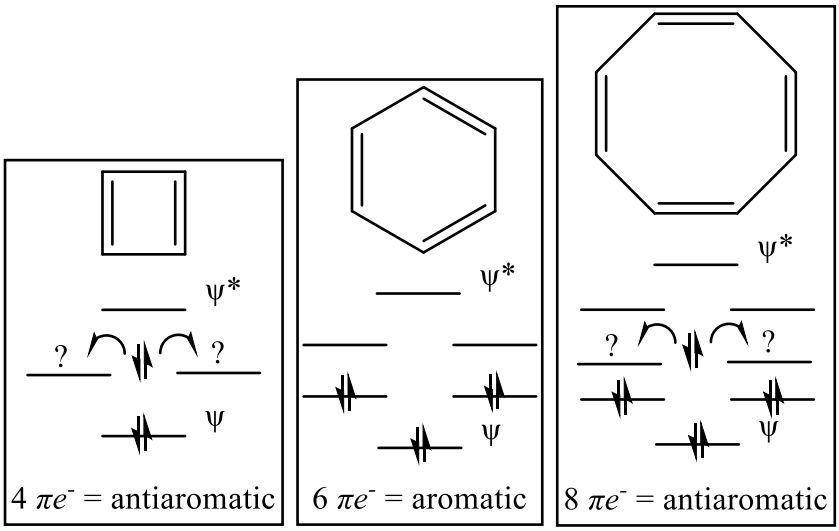

Figure 1.1 - Simplified π molecular orbital diagrams of some even carbocycles (**A** = 1,3-cyclobutadiene, **B** = benzene, **C** = 1,3,5,7-cyclooctatetraene).

Due to the ambiguous nature and varied usage of the term aromaticity, several recent computational works have suggested that aromaticity is best predicted based on the magnetic properties of conjugated systems such as the magnetic susceptibility, and NMR chemical shifts.[50]

Anionic aromatic ligands are perhaps the most observed in organometallic chemistry, as their electron rich π clouds can satisfy the electronic requirements of high valent metals. These are most often produced through reduction of a non-aromatic framework, such as in the deprotonation of non-aromatic 1,3-cyclopentadiene (HCp) to produce the aromatic anion cyclopentadieneide (Cp^-), or the reduction of non-aromatic 1,3,5,7-cyclooctatetraene (COT) to the aromatic dianion cyclooctatetraeneide (COT^{2-}).

1.2.3 Transition Metal Organometallic Chemistry:

The reactivity of Transition Metal (TM) organometallic chemistry is often inspected with respect to the 18-electron rule, which states that because TMs have a maximum of 9 Valence Orbitals (VOs) they can form a maximum of 9 Molecular Orbitals (MOs) with the LF. Due to the Pauli exclusion principle, TM complexes therefore cannot have more than 18 electrons unless higher energy atomic orbitals or ligand-based reduction is invoked.[51] While this is not an all-encompassing rule, it explains well the behaviour and stability of transition metal organometallic complexes due to their strong LF splitting, such as in metal-arenide complexes.[52–54]

The instability of palladium (II) metallocenes was evidenced by Gusev and Maitliss in 1996, who reported the electrochemical reduction of the cationic 18-electron palladium (IV) complex $[Pd(\eta^5\text{-}Cp^*)][BF_4]_2$ in the presence of $NaBF_4$ supporting electrolyte (**Scheme 1.1**). The resultant voltammogram shows two reversible reductions, the first at -0.08 V and the second at -0.78 V (Vs SCE), showing that these species are stable on the CV timescale (200 mV/s). However, the authors report that all attempts to prepare the 20-electron neutral $[Pd(\eta^5\text{-}Cp^*)]$ species chemically have given unidentified products, so the transient species could not be characterised.

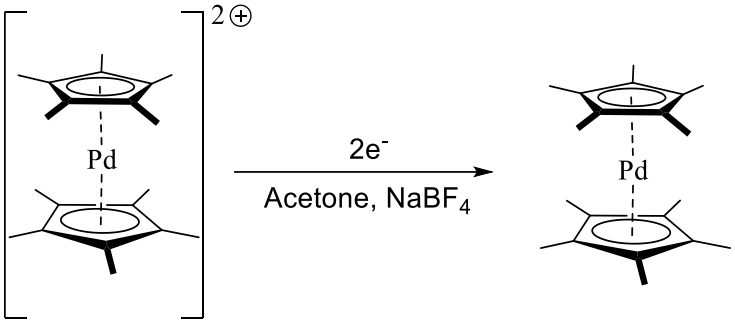

Scheme 1.1 - Synthetic scheme describing the electrochemical reduction of the 18-electron palladium (IV) cationic species $[Pd(\eta^5\text{-Cp})]^{2+}$ to yield the proposed transient 20-electron species $[Pd(\eta^5\text{-Cp})_2]$, reported by Gusev and Maitliss.

The authors reported that any attempts to prepare platinum analogues of the reported 19 or 20 electron palladium species *via* electrochemical methods had failed. Comparing the Palladocenium species reduction potentials to those of previously reported 18-electron metallocene systems, Gusev and co-workers show that the group 10 metal ions (nickel (IV), palladium (IV), platinum (IV)) all show exceptionally low first and second reduction potentials when compared to the rest of the transition metals. They argue that the stability of the 19- and 20-electron metallocenes decreases moving down transition metal series and from right to left. Considering that the 20-electron neutral nickelocene is stable, it appears that isolation of a neutral platinum or palladium metallocene can be achieved *via* organometallic chemistry if the correct LF is designed which satisfies the metal's electronic requirements.

Indeed, neutral low-valent palladium systems have been reported utilising bulky electron poor organometallic ligands to stabilise these catalytically active species (**Figure 1.2**). Shown first is $[Pd_2(\eta^2, \eta^2, \text{-dba})_3]$ (dba = dibenzylideneacetone), first reported in 1970 and the subject of extensive spectroscopic and computational studies, it is a commercially available bench-stable source of zerovalent palladium and is ubiquitous in research and industrial settings.[55–57] The remarkable stability of this species is attributed two factors – first, the π-donor α,β-eneones are electron poor due to tautomeric delocalisation with the ketone moiety, allowing synergistic π-back bonding from the zerovalent metal into the ligand's π system. Detailed synthetic and computation studies by Fairlamb and co-workers examining the reaction kinetics of low-valent palladium systems have disclosed that the rate of dissociation of free zerovalent palladium into solution in substituted $[Pd_2(\eta^2, \eta^2, \text{-dba})_3]$ systems is dominated by the strength of the metal-to-ligand π-backbonding interaction.[58–60] Strongly electron donating species, such a para-substituted aryl ethers, are shown to increase the concentration of dissociated palladium in solution; whereas strongly electron withdrawing groups, such as para trifluoromethyl substituted phenyl, show a decreased concentration of free palladium. In addition to these electronic effects, $[Pd_2(\eta^2, \eta^2, \text{-dba})_3]$ is also kinetically stabilised by the large phenyl rings of the dba ligands which decrease lability and block additional coordination at the palladium centres. The widespread use of $[Pd_2(\eta^2, \eta^2, \text{-dba})_3]$ is a salient reminder of the power of organometallic chemistry in designing catalytically active materials with TMs, especially when aided with advanced computational methods.[59]

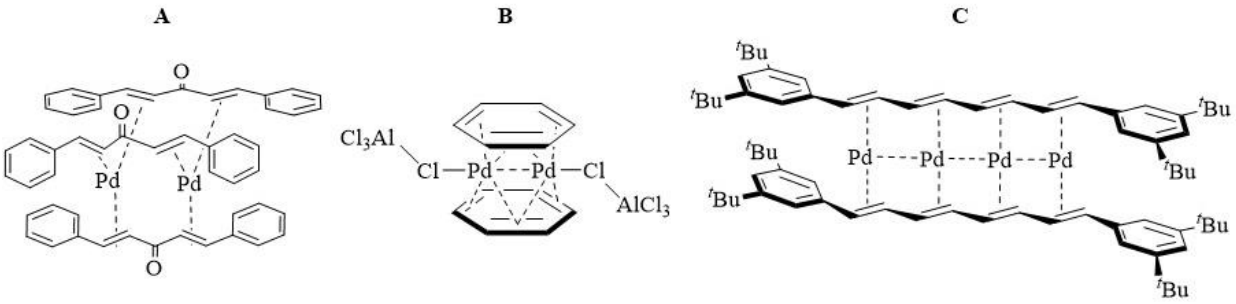

Figure 1.2 - Schematic representation of selected structurally authenticated low-valent palladium organometallic species $[Pd_2(\eta^2, \eta^2, \text{-dba})_3]$ (**A**), $[Pd_2AlCl_4(\eta^4\text{-}C_6H_6)_2]$ (**B**), and $[Pd_4(\eta^2\text{-}^t\text{Bu-DPOT})_2]$ (**C**).

The second species shown, $[Pd_2Al_2Cl_8(\eta^3\text{-}C_6H_6)_2]$, is a neutral bis arene sandwich dimer, comprising two monovalent palladium centres charged balanced by two$\{(\mu\text{-}Cl)(AlCl_4)\}^-$ moieties. This species was reported in 1970 and is one of the only structurally-authenticated example of an arene sandwiching a metal-metal σ-bonded dimer, giving a total count of 18 valence electrons for each palladium (I) centre.[61,62] The nature of the metal-metal and metal-ligand interactions have been extensively investigated because of their relevance in cross-coupling and CO activation reactions.[63–70] The ability of a neutral arene ligand to stabilise an unsupported palladium-palladium bond demonstrates the power of organometallic chemistry in investigating Transition Metal complexes such as these with catalytic relevance.

The final species shown is one of the first in a series of multinuclear low-valent palladium clusters reported by Murahashi and Kurosawa over the past two decades.[71,72] Through careful selection of organometallic ligands and low-valent palladium precursors, Murahashi's group have reported families of low-valent palladium clusters with precise control of nuclearity, from dinuclear[73] to decanuclear[74] (**Figure 1.3, A**), and elegant control over topology, with chain[75], triangle[76], square[77], and even spherical cluster[78] (**Figure 1.3, B**) geometries structurally authenticated. Catalytic studies utilising these clusters have only recently been performed, but some examples of highly selective reactions, such as the E/Z isomerisation of dienes have been reported.[79–81] They have also been suggested in the development for molecule machines due to their facile redox-switchable behaviour.[82]

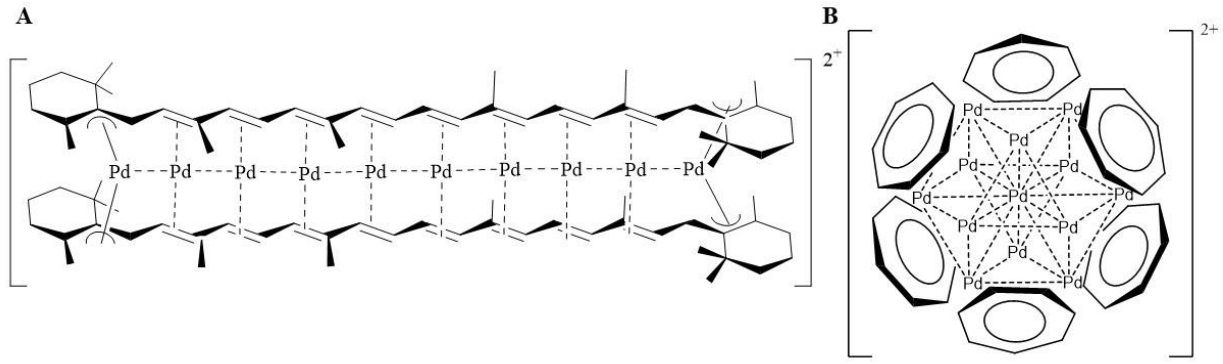

Figure 1.3 - Schematic representation of the cations in two low-valent palladium clusters reported by Murahashi and co-workers. $[Pd_{10}(\mu^{10}\text{-}\beta\text{-carotene})_2][B(ArF)_4]_2$ (**A**), and $[Pd_{13}(\mu^4\text{-}C_7H_7)_6][B(ArF)_4]_2$ (**B**).

These examples demonstrate the breadth of sophistication granted through TM organometallic chemistry. Designer organometallic complexes such as these may represent the future of catalysis or molecular machines, with nuclearity and topology precisely modulated to design materials with high selectivity, activity, and low metal loading with respect to traditional materials.

1.2.4 Electronic Structure of Lanthanides:

The Lanthanide metals are most commonly seen in their trivalent state, giving the stable $4f^n$ valence electron configuration, and act as hard Lewis acids with coordination numbers between 8 and 12. Unlike the Transition Metals, the Lanthanide Metals stability cannot be explained in terms formal electron counting, instead their reactivity has been rationalised in terms of steric and electronic satisfaction *via* mainly electrostatic interactions with the CF.[83] The 4f orbitals of trivalent Lanthanide ions have limited radial extension and are described as "core-like" (**Figure 1.4**), characterised by the near degeneracy of the 4f orbitals, significant spin-orbit coupling, and weak CF interactions; giving rise to huge single-ion anisotropy and ladder-like energy levels of the CF microstates, denoted m_J (J = total angular momentum quantum number) (**Figure 1.5**).

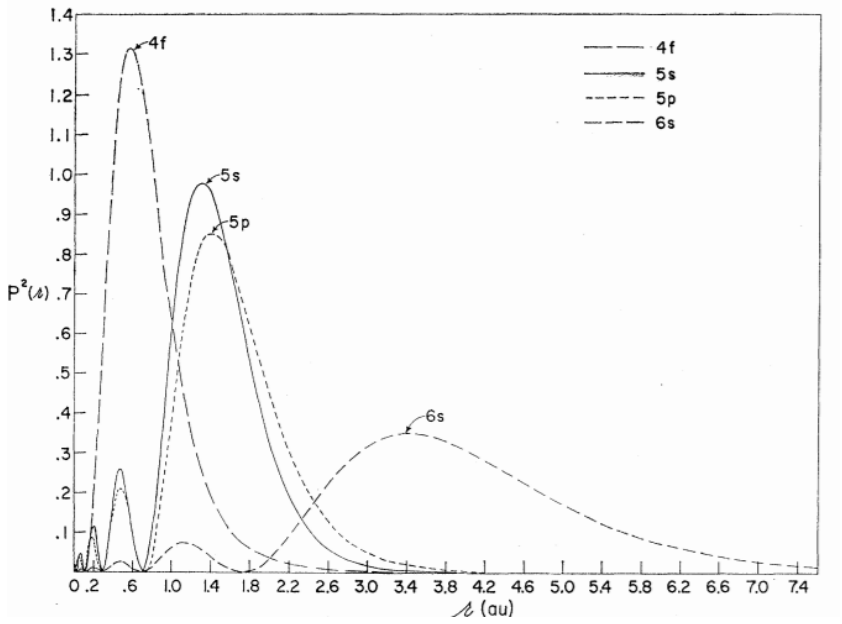

Figure 1.4 - Probability distribution function for gadolinium (III), showing electron probability density as a function of radius for selected electron shells. Note that the 4f valence electrons are localised close to the nucleus and are "shielded" from their environment by the 5s and 5p shells. Reproduced from ref. 190 with permission.

Because of the significant unquenched orbital moment present in Lanthanide (III) ions, the total spin (S) is not a good quantum number to describe their magnetic properties. Instead, we must invoke Russel-Saunders coupling, whereby the spin and orbital (L) quantum numbers are used to compute a total angular momenta quantum number (J).[84] We can see this visually in **Figure 1.5 B**, where spin-orbit coupling separates the ^6H term for a dysprosium (III) ion into multiplets by the value of J, which are well separated. Once in a coordination environment, the CF interactions will cause these levels to split into 2J+1 sublevels, often referred to as CF microstates or Stark sublevels. Due to the relatively invariant nature of metal-ligand bonding in Lanthanide complexes, these sublevels will often give sharp "fingerprint" emission spectra at low temperatures, due to forbidden f -> f transitions unique

to each ion.[85] The large energy gaps and long lifetimes of Lanthanide ion excited states have prompted their use in a number of optical fields, such as upconversion and labelling.[18,86–88] Finally, in the presence of an external magnetic field the electrons will experience Zeeman splitting, and will be (de)stabilised based on the alignment of the microstates' g-tensor with the field.[89]

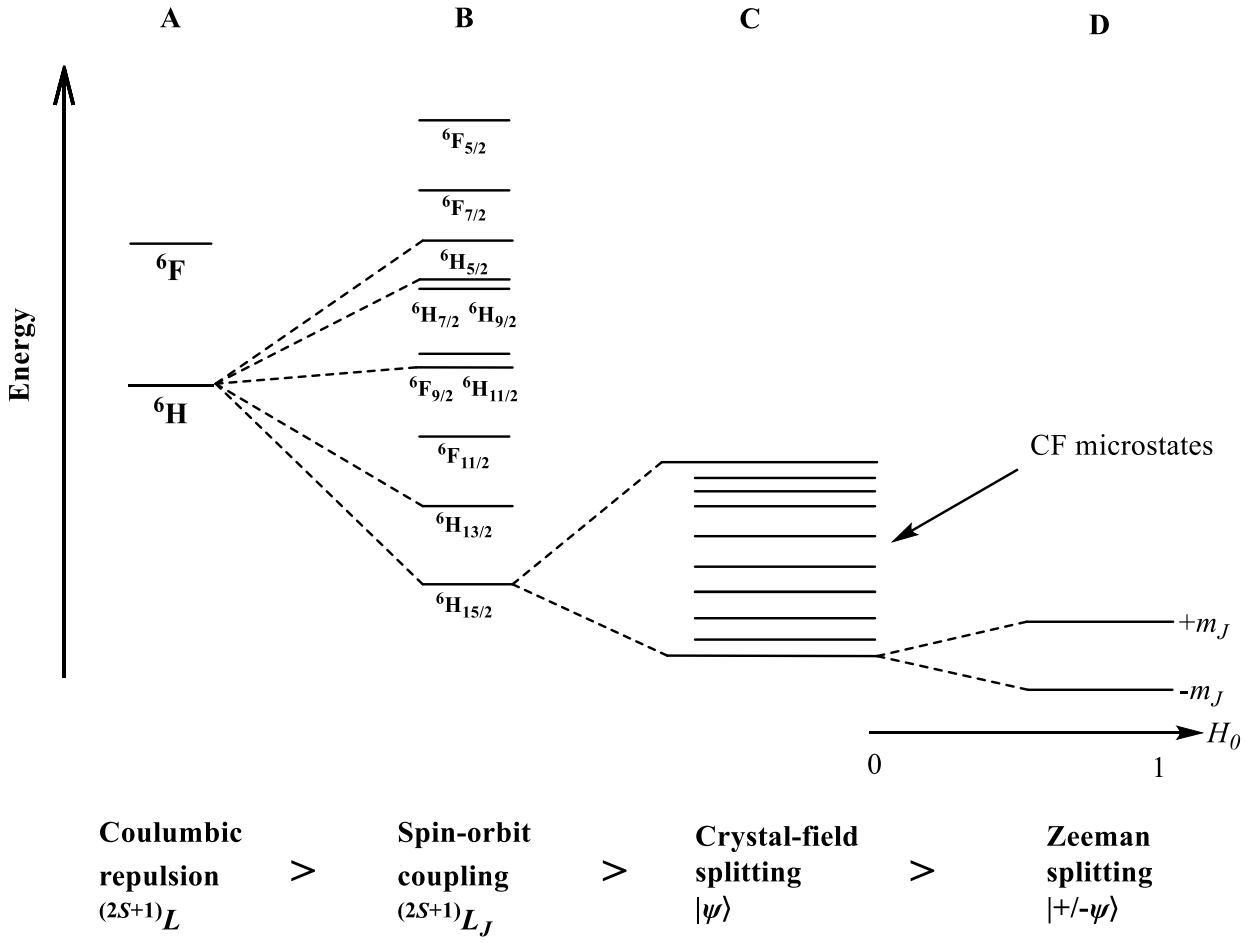

Figure 1.5 - Schematic representation of some of the electronic interactions felt by the dysprosium (III) 4f electrons in order of decreasing magnitude: electron-electron or columbic repulsion 0 – 30,000 cm^{-1}, described using Russel-Saunders term symbols (**A**); spin-orbit coupling 0 – 20,000 cm^{-1}, described using Russel-Saunders levels (**B**); CF splitting 0 – 1,000 cm^{-1}, described using the bra-ket notation for each projection of J (**C**); The Zeeman interaction further splits the projections of J by their orientation with respect to an applied field on the order of 0 – 10 cm^{-1} (**D**).

1.2.5 Lanthanide Organometallic Chemistry:

Organometallic lanthanide, and similarly actinide, chemistry differ greatly TM organometallic chemistry as the 4 and 5f metals are extremely oxophillic, and their complexes tend to be strongly air and moisture sensitive and pyrophoric. Air and moisture stable lanthanide coordination complexes have been reported through the use of strong *O* donor ligands, such as bulky phosphine oxides or acetylacetonates, to great effect. However, only non-aqueous organometallic lanthanide chemistry will be discussed further.

The organometallic chemistry of the rare earth elements has made great strides through the use of anionic π-donor ligands, as they are shown to interact strongly with the 4f

electrons and can be used to stabilise a number of non-classical electronic structures.[90] A fascinating example of this is the work of the Lappert and Evans in isolating the entire series of rare earths in the divalent state, many of which (Y, Ho, Er, Pr, Gd, Tb, Lu) had not previously been observed.[91] This was achieved through the reduction of the trivalent species [Ln(η^5-Cp')$_3$] (Ln = La – Lu, Y; Cp` = trimethylsilylcyclopentadieneide) with potassium intercalated graphite (KC_8), a powerful reducing agent with an exceptionally high surface area, in the presence of the macrocyclic alkali-metal chelating agent 2.2.2-cryptand under an inert atmosphere (**Scheme 1.2**).[92–94]

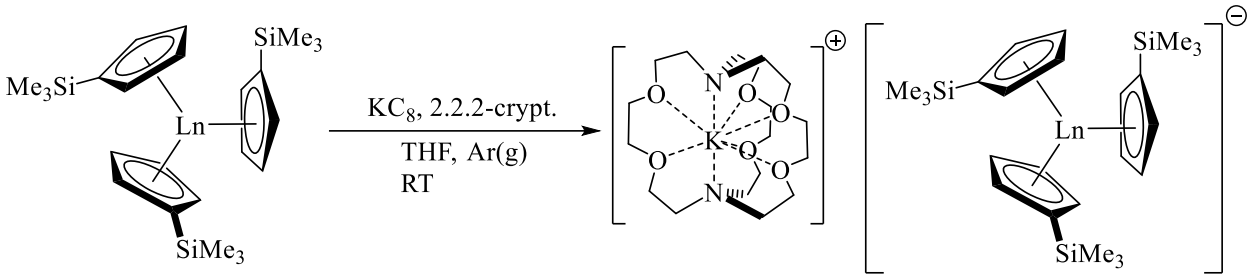

Ln = La, Ce, Pr, Nd, Sm, Eu, Gd, Tb, Dy, Ho, Er, Tm, Yb, Lu, Y

Scheme 1.2 - Synthetic scheme representing the synthesis of divalent rare earth complexes reported by Evans and Lappert. Note: an atmosphere of argon was used as these species are shown to undergo reduction of gaseous nitrogen while in solution, emphasizing the extreme thermodynamic instability of these species.

The Lanthanide (II) ions are stabilised by a coordination sphere of three anionic (η^5-Cp') ligands, and the charge balance is completed by a potassium counter cation chelated by 2.2.2-cryptand, allowing full structural and spectroscopic characterisation of these extremely unstable species *via* single-crystal X-ray diffraction (SC-XRD) analysis, electron paramagnetic resonance (EPR) spectroscopy, and SQUID (superconducting quantum interference device) magnetometry. Structural analysis and computational collaborations have given insight into the electronic properties of these systems, identifying a trend whereby the "non-classical" Lanthanide (II) ions with more negative reduction potentials (La, Ce, Pr, Gd, Tb, Ho, Er, Lu, Y) adopt a $4f^n\ 5d^1$ valence electron configuration, and the "classical" Lanthanide (II) ions with more positive reduction potentials (Sm, Eu, Tm, Yb) adopt a $4f^{n+1}$ configuration. Between these two regimes lie dysprosium (II) and neodymium (II) ions, which are considered "configurational crossover" ions, as they exhibit moderate reduction potentials and can vary between $4f^n\ 5d^1$ and $4f^{n+1}$ configurations depending on the CF.[95,96] The functionalised Cp arenide is the only ligand system that has been successfully utilised to isolate Lanthanide (II) species for the entire series, demonstrating the power of organometallic chemistry in manipulating the electronic properties of Lanthanide systems.[91]

1.3 Molecular Magnetism:

Molecular magnetism describes the study of materials wherein discrete molecules act as independent magnetic domains, as opposed to the bulk phase in traditional magnetic materials. Within this umbrella lies single-molecule-magnets (SMMs), single-ion magnets/mononuclear single-molecule magnets (SIMs), and single chain magnets (SCMs).[97] This field has grown rapidly since the discovery of magnetic bi-stability in Mn_{12}-acetate in the early 90s by Sessoli, Henderson, and Christou,[98–101] as it was postulated that such a material could be used in the development of ultra-high-density data storage, quantum computing, and spintronics.[102] The barrier to relaxation of the magnetisation in molecular

systems is a consequence of magnetic anisotropy, which can be imparted through inherent single-ion properties – such as spin orbit coupling - or bonding interactions such as molecular symmetry, Jahn-teller distortion and magnetic exchange coupling. Because of the importance of magnetic anisotropy in generating a significant barrier to spin relaxation, the Lanthanide ions have moved to the forefront of SMM research; their 4f valence electrons have massive inherent anisotropy due to their core-like nature, leading to unquenched orbital-angular momentum and large spin-orbit coupling (*vide supra*). Additionally, their "ladder-like" CF microstates with significant energy gaps give rise to multi-step thermally activated spin-relaxation, which is desired in the design of high-performance SMMs.[103]

1.3.1 Spin-Lattice Relaxation:

Paramagnetic spins will reach thermodynamic equilibrium with their surroundings if sufficient energy-transfer pathways exist between the spin and the thermal bath, (the crystalline lattice in a solid-state system). This simple relationship is what drives the demagnetisation of paramagnetic materials, such as SMMs, on the removal of an applied field.[104,105]

This behaviour was first observed and named spin-lattice relaxation by Orbach, Van Vleck, and contemporaries, who examined the temperature dependence of the spin-relaxation in bulk paramagnetic salts and developed models to rationalise them in terms of the electronic CF interacting with harmonic vibrations of the crystalline lattice.[106,107] This energy transfer is mediated by phonons, quasiparticles representing harmonic oscillations propagating through the crystalline lattice with discrete energy. If a phonon mode possesses the correct symmetry and energy, it can introduce dynamic interactions into the spin's CF g-tensors *via* modulation of Zeeman and hyperfine interactions, a process called spin-phonon coupling, allowing transfer of energy between the spin and the bath.[108–112] Understanding the microscopic nature of spin-phonon coupling has been a challenge historically, though by identifying their respective field and temperature dependencies, four major processes to spin-relaxation are commonly identified.[113–117]

The **direct process** is a single phonon relaxation mechanism, whereby the spin transitions between microstates (m_s in the case of SMMs, m_J in the case of Lanthanide SIMs) with a corresponding emission or absorption of a single lattice phonon. The direct process is only operative under an applied magnetic field, when there exists a finite energy gap between the opposing spin-states due to Zeeman splitting (**Fig. 1.6, A**). The **Orbach process** describes the excitation of the spin through the absorption of a phonon, followed by relaxation of the spin and emission of a second phonon. As the Orbach process requires the spin system to "climb" many of the CF microstates before relaxing, it offers the largest possible thermal barrier to demagnetisation and is highly desired in the design of SMMs (**Fig. 1.6, B**).[118] In the **Raman process**, spin-relaxation is driven through the simultaneous absorption and emission of a lattice phonon. The superposition, or energy difference, of the two phonon modes corresponds to the energy released from the relaxing spin. This process is described as occurring through "virtual" excited states, meaning transient quantum states that are too short lived to be observable. In the first order, or **Van Vleck Raman process**, the spin is described as relaxing directly while the bath interacts *via* a virtual phonon intermediate (**Fig. 1.6, C**). In the **second-order Raman process**, both the spin and the bath interact *via* virtual intermediate states (**Fig. 1.6, D**). The Raman process is perhaps the least understood of the four major spin relaxation processes. It is considered a limiting property of high-performance SMMs, as it allows "through-barrier" relaxation without reaching the highest microstate.[119,120] Not shown is a process known as **quantum tunnelling of the magnetisation** (QTM). This is a temperature independent process whereby the spins can relax directly without any transfer of

energy to the lattice.[121] QTM is highly desired in spintronics, where the superposition of two microstates has been suggested as a potential quantum bit (qubit).[122] However, in molecular magnetism this interaction is undesirable as it leads to faster spin relaxation. This process is attributed theoretically to off-diagonal terms in the CF matrix, which can be eliminated through high point-group symmetry[123,124] and through utilisation of Kramer's theorem[104,125], which states that mixing of microstates with half-integer angular momenta is forbidden (such as in the $H_{12/5}$ dysprosium (III) ground state doublet), however this is often not the case experimentally.[126,127]

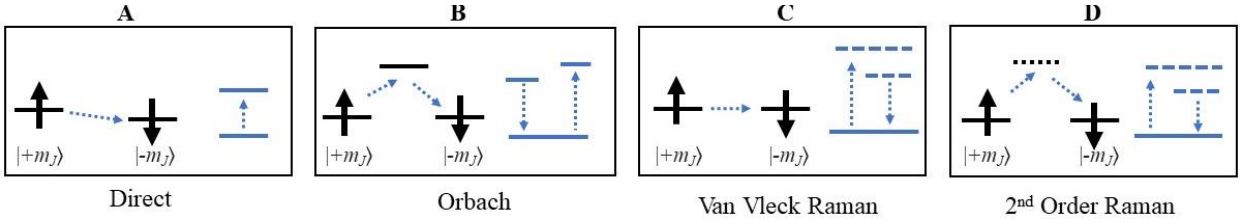

Figure 1.6 - Schematic representations of commonly described spin-relaxation pathways in SMMs. Black lines represent CF microstates, blue lines represent phonon modes. Dotted lines represent virtual states. The direct process, involving absorption or emission of a single phonon accompanied by relaxation of the spin (**A**). Orbach process, involving excitation of the spin to an electronic excited state then relaxation via the absorption and emission of a phonon (**B**). Van Vleck Raman, involving direct relaxation via simultaneous absorption and emission of lattice phonons (**C**). 2nd order Raman, involving excitation of the spin to a virtual state then relaxation via the simultaneous absorption and emission of lattice phonons (**D**).

Each of these processes is defined by its unique temperature and field dependence, and spin relaxation dynamics can thus be compared with the equation[105,128]:

$$\tau^{-1}(T,H) = \tau_{QTM}{}^{-1}(T,H) + \tau_{Orbach}{}^{-1}(T) + \tau_{Raman}{}^{-1}(T) + \tau_{Direct}{}^{-1}(T,H) \quad \textbf{1.1}$$

Where τ^{-1} describes the relaxation rate for the whole system and the respective processes. When comparing the temperature dependence of the relaxation rate this becomes:

$$\tau^{-1}(\mathrm{T}) = \tau_{QTM}{}^{-1} + [\tau_0{}^{-1}\mathrm{e}^{(-U\mathrm{eff}/k\mathrm{B}T)}] + [CT^n]\ (1.3) \quad \textbf{1.2}$$

Where the rate of quantum tunnelling is assumed to be constant; the Orbach process is described using an Arrhenius law with preexponential factor τ_0, often referred to as the "attempt time", and an effective energy barrier U_{eff}. Finally, the Raman process is described with parameter C representing the lattice phonon distribution (but most often used as a free fitting parameter) and the Raman exponent n, which has an expected value of n = 9 for a Kramer's ion and n = 7 for a non-Kramer's ion, however values between 1-9 are often reported. This is often prescribed either to over parameterisation of the model or the interaction of high energy optical phonons within the lattice.[129,130] It is noteworthy that only the Orbach process shows an exponential temperature dependence, allowing it to be distinguished *via* a plot of the relaxation rate against the temperature (**Figure 1.7, A**).

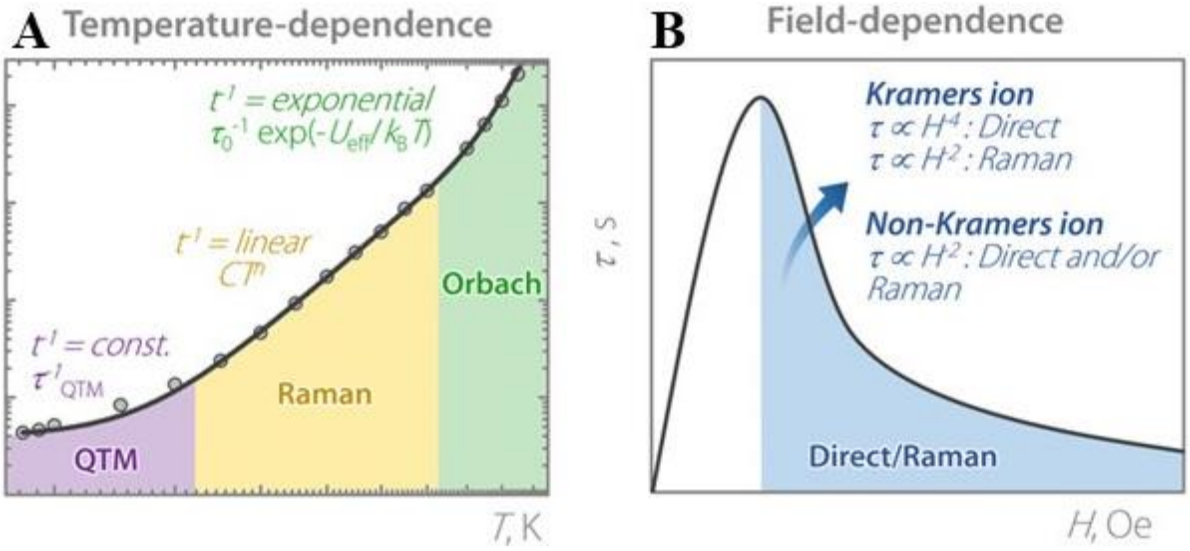

Figure 1.7 - Hypothetical plot of the temperature dependence of the rate of spin relaxation in an SMM (**A**). The three regimes represent the commonly observed relaxation processes and their associated temperature dependencies. QTM regime at low temperatures with a constant rate; Raman at intermediate-high temperature with power-law temperature dependence. Orbach regime at high temperatures with exponential temperature dependence. Hypothetical plot of the field dependence of the rate of spin relaxation in an SMM (**B**). Direct process shows exponential field dependence. Reproduced from ref. 88 with permission.

When comparing the frequency dependence of the spin relaxation we must take into consideration the QTM, Raman, and direct processes:

$$\tau^{-1}(\mathrm{H}) = [B_1/\ 1 + B_2H^2] + [C\ (1 + C_1H^2\ /1 + C_2H^2)T^{n_2}] + AT\mathrm{H}^4 \qquad \textbf{1.3}$$

We must take into consideration here that the direct process is not operative at low fields but increases with field strength. Conversely, QTM rate has a strong inverse relationship with the field strength, and low fields are often used in the characterisation of "field-induced magnets" for this reasons. In order to prevent activating a Direct regime, a plot of the field dependence of the relaxation rate should be generated to pick an "optimal field" which can suppress QTM but isn't so strong as to facilitate Direct relaxation **(Figure 1.7, B)**.

1.3.2 Squid Magnetometry:

The behaviour of paramagnetic materials can be evaluated using a superconducting quantum interference device (SQUID) magnetometer.[131] SQUID magnetometers can detect extremely subtle changes in sample magnetisation by taking advantages of the Josephson effect, whereby the voltage across two superconductors bridged by an insulator is proportionate to the rate of quantum tunnelling of electron pairs across the gap and is modulated by the presence of external magnetic fields.[132] By moving a sample through the SQUID coils while applying a constant magnetic field, we can observe the static magnetic properties of a sample, manifesting as a change in voltage across this gate. This technique is known as direct current (DC) magnetometry and is a routine measurement in the characterisation of paramagnetic systems. If we carry out the same experiment but instead apply a dynamic oscillating magnetic field, we can examine the spin-relaxation behaviour of a sample. This technique is known as (AC) magnetometry and is ubiquitous in spintronics and SMM research.

1.3.3 DC Magnetometry:

There are two routine DC magnetometry experiments used to characterise a paramagnetic sample. The first is measuring the magnetic susceptibility of the sample. The magnetic susceptibility is the response of a sample to an external field, either attractive or repulsive, and is defined as the change in magnetisation of a sample with respect to the external field (**eq. 1.4**):

$$\chi = \frac{\delta M}{\delta H} \qquad \textbf{1.4}$$

In weak external fields, χ is independent of H, allowing this to be reduced to:

$$\chi = \frac{M}{H} \qquad \textbf{1.5}$$

The magnetic susceptibility can be broken down into additive diamagnetic and paramagnetic susceptibilities, with the former being negative and the latter positive by convention:

$$\chi = \chi_D + \chi_P \qquad \textbf{1.6}$$

The diamagnetic susceptibilities of common materials are well known, and can be evaluated using Pascal's constants, or estimated as[133]:

$$\chi_D = \text{a MW x } 10^{-6} \text{ (cm}^3 \text{ Mol}^{-1}\text{)} \qquad \textbf{1.7}$$

Where a is a factor between 0.4 – 0.5 and MW is the material's molecular weight. These data are often quoted in the form of volume (unitless), mass (cm^3g^{-1}), or molar (mol^{-1}) susceptibilities.

For simple paramagnetic systems with no magnetic communication, the temperature dependence of the magnetic susceptibility is expected to follow a Curie-law relationship, with deviations at low temperature indicative of magnetic ordering:

$$\chi = \frac{N g^2 \beta^2}{3 K_B T} S(S+1) \qquad \textbf{1.8}$$

Where N = Avogadro's number, g = the Landé g-factor, β = the Bohr magneton, K_B = the Boltzmann constant, and S = the total spin of the system. As ($N\beta^2/3K_B$) is a constant, this can be simplified to:

$$\chi T = \frac{g^2}{8} S(S+1) \qquad \textbf{1.9}$$

In the case of 4f ions where significant spin-orbit coupling must be taken into consideration, we can use the Russel-Saunders method to evaluate the g-factor:

$$g_J = \frac{3}{2} + \frac{S(S+1) - L(L+1)}{2J(J+1)} \qquad \textbf{1.10}$$

Where L = the total orbital angular momentum and J = the total angular momentum. With this in hand we can fit the 4f ions' susceptibility:

$$\chi T = \frac{g_J^2}{8} J(J+1) \qquad \textbf{1.11}$$

Experimental values at room temperature are usually consistent with the Curie-law values. At lower temperatures the χT product often drops precipitously, not due to magnetic ordering, but due to depopulation of CF microstates and the presence of significant magnetic

blocking. Accurate computation of these values thus requires an in-depth analysis of the CF microstates and their populations, for which *ab initio* methods have proved highly successful.[134]

The second routine characterisation carried out is examining the magnetisation and reduced magnetisation behaviour under applied fields. In the case of highly-anisotropic Lanthanide ion samples, we expect to see gaps between the isothermal magnetisation curves on increasing field strength, where the saturation magnetisation can be determined utilising the effective *g*-tensor of the magnetic ground state:

$$M_{SAT} = \frac{1}{4} g_{eff} N\beta \qquad \textbf{1.12}$$

Thus, a dysprosium (III) ion with perfectly axial anisotropy ($g_z = 20$) would yield a saturation magnetisation value of approximately 5 β, which is often observed. Reduced magnetisation analysis compares the magnetisation of the sample to the strength of the external field divided by the absolute temperature of the sample and gives further insight into the anisotropy of the system.

Utilising these experimental methods, and corroborating them with computational methods, we can learn a great deal of insight into the static magnetic properties of paramagnetic systems, such as the exchange coupling strength, spin ground state, and anisotropy of the ground state. However, to analyse dynamic processes, such as magnetic relaxation, we must utilise alternating current (AC) magnetometry.

1.3.4 AC Magnetometry:

Instead of a static external field, in AC magnetometry experiments a small oscillating magnetic field is applied to induce a time-dependent moment in the sample. When the frequency of the oscillating field is faster than the rate of relaxation, the magnetisation of the sample "lags" behind the external field. This response can be decomposed into real and imaginary components, where the peak maxima of the imaginary, or "out-of-phase" susceptibility corresponds to the spin relaxation time:

$$\tau = (2\pi\upsilon)^{-1} \qquad \textbf{1.13}$$

The spin relaxation time is an important quantity for comparing SMMs and is routinely extracted by fitting the frequency dependence of the in-phase and out-of-phase susceptibilities to the generalised Debye model:

$$\chi' = \chi_S + \frac{(\chi_T - \chi_S)[1+(2\pi\nu\tau)^{1-\alpha}\sin(\frac{\pi\alpha}{2})]}{1+2(2\pi\nu\tau)^{1-\alpha}\sin(\frac{\pi\alpha}{2})+2(2\pi\nu\tau)^{2(1-\alpha)}} \qquad \textbf{1.14}$$

$$\chi'' = \frac{(\chi_T - \chi_S)[1+(2\pi\nu\tau)^{1-\alpha}\sin(\frac{\pi\alpha}{2})]}{1+2(2\pi\nu\tau)^{1-\alpha}\sin(\frac{\pi\alpha}{2})+2(2\pi\nu\tau)^{2(1-\alpha)}} \qquad \textbf{1.15}$$

Where χ' represents the in-phase or real part of the susceptibility, χ'' represents the out-of-phase or imaginary part of the susceptibility, χ_T represents the isothermal, or static susceptibility, and χ_S the adiabatic, or equilibrium susceptibility. When the sample relaxes *via* one of the processes described previously it will result in an increase in the χ'' signal and a decrease in the χ'signal. This model assumes that each peak represents a single relaxation process, and extracts from them their distribution parameter, α, which ranges from 0 - 1 and represents the peak broadness; and the relaxation rate, τ as the peak maximum. This model has become standard in the analysis of high performance SMMs over the past decade with great success; prior to this Arrhenius only or Gaussian functions were commonplace,

however these will not be discussed further.[135,136] The popular software CC-FIT2 published by Chilton and Reta in 2019 was developed to automate fitting these data, which can contain upwards of dozens of datasets in the case of high-performing SMMS.[137] However manually fitting data is still preferred by many as not all peaks can be cleanly resolved automatically. Error bars for the relaxation rate can be generated as a log normal distribution of the peak widths using a method described by Chilton and Reta.[137]

After the relaxation rate has been extracted by fitting the frequency dependence of the out-of-phase susceptibility to equation **1.14**, a plot of the temperature or field dependence of the rate can be generated to analyse the individual relaxation mechanisms as described in section 1.3.1 using equations **1.2** and **1.3** respectively **(Figure 1.7)**. In the case that multiple relaxation processes are operative simultaneously, as has been observed for some high-performing SMMs, a double Debye model has been invoked to explain these data with good success, however this will not be discussed further.[138,139]

Magnetic hysteresis and zero-field-cooled field-cooled (ZFC-FC) experiments are the final tool used to routinely characterise SMMs. These tools measure the strength, or coercivity, of the magnetisation *via* sweeping a dynamic field at a fixed temperature or sweeping a temperature gradient at a fixed field. From these data we can obtain the blocking temperature, T_B, a contentious parameter which fundamentally represents the highest temperature at which the sample can retain magnetisation in the absence of an external field. Historically, T_B has been defined as the temperature at which the hysteresis "loops" close in M vs H hysteresis measurements (**Fig. 1.8, A**). Valid discussion has emerged on the utility of this method for comparisons, as the field sweep rate is often not reported, and can vary by orders of magnitude (10 – 500 Oe s^{-1} for commercial PPMS systems). By increasing the sweep rate, the sample may not reach saturation magnetisation or fully demagnetise, and thus may imply the presence of slow magnetic relaxation of a molecular origin where there is in fact none. The ZFC-FC experiment (**Figure 1.8, B**) is a more recent method, complementary to hysteresis, which measures the temperature at which the magnetisation of the sample diverges when cooled under zero-field compared to when the sample is cooled under an applied field. If slow magnetic relaxation is present then we would expect the sample cooled under an applied field to bifurcate from the zero-field cooled sample at the temperature where magnetic blocking becomes active, T_B.[140] It is suggested that this experiment is a more accurate measure of T_B, however these experiments are known to be user dependant and suffer from the same obfuscation of sweeping rates as hysteresis measurements. A new consensus is emerging within the field that these measurements must be standardised and corroborated with computational methods to allow real insight into the microscopic origin of spin-relaxation.

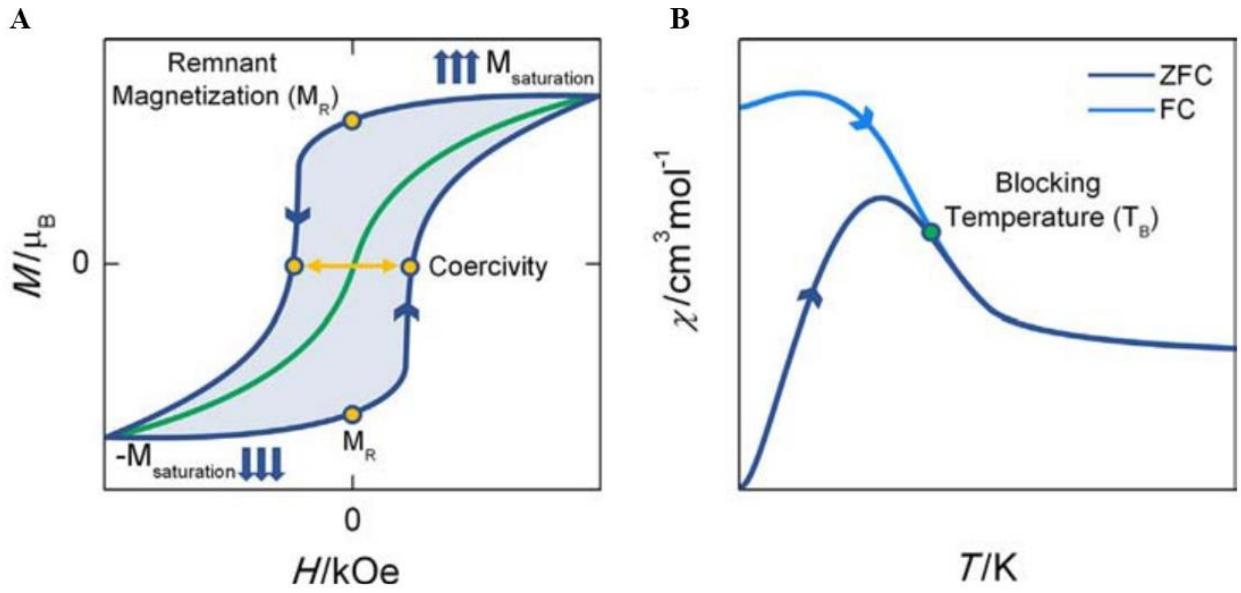

Figure 1.8 - Schematic representations of the M v H hysteresis experiment (**A**), and the χ v T ZFC-FC experiment (**B**). In the M v H hysteresis experiment, the field is swept to saturation and the magnetisation of the sample is measured at a constant temperature. If SMM behaviour is present, then the "loops" (blue) are open, and their width at zero-field determines the Coercivity. The temperature at which the loops close determines the blocking temperature (TB). In the χ v T ZFC-FC experiment the sample is cooled to 1.8 K either in the presence (navy) or absence (blue) of an external field. After cooling, the sample is heated to 300 K in the presence of an applied field in both cases. If SMM behaviour is present, we expect the ZFC and FC susceptibilities to bifurcate (diverge) at the temperature where magnetic blocking is lost, T_B. Adapted from from ref 140 with permission.

1.3.5 Modern SMM Design Principles:

Taking into consideration the anisotropic model proposed by Reinhart and Long,[141] and the CF interactions impact on the m_J states as discussed by Chibotaru and Ungur and others,[103,118,142] modern high-performing SMM designs aim to prepare Lanthanide complexes with specific features:

-Kramer's ions, such as dysprosium (III), or erbium (III), to suppress quantum tunnelling.

-Strong-field ligands whose coordination geometry stabilises the ground state with the highest angular momenta: **axial** ligand fields complement the **oblate** electron distribution in dysprosium (III)'s $^6H^{15}/_2$ ground state, whereas **equatorial** ligand fields complement the **prolate** electron distribution in erbium (III)'s $^4I_{15/2}$ ground state.

-Low coordination numbers and high point group symmetry, such as the pseudolinear metalloceniums or the D_{5h}[143] group, to eliminate transverse CF terms and optimise the CF energy levels for multistep relaxation.

Because of the strict CF requirements of high performance SMMs, organometallic Lanthanide systems have overtaken classic Werner-type coordination complexes and broken significant milestones within the field, such as overcoming the liquid nitrogen barrier (T_B > 77 K) in 2019, only 9 years after the first reported organometallic Lanthanide SMM was published.[144,145]

1.3.6 Organometallic Lanthanide SMMs:

Following these computational insights, a number of record-breaking organometallic Lanthanide SMMs have been disclosed, offering experimental insight into the frontier of these fields. Three milestone organometallic SMMs are shown in **Figure 1.9**. Reported by Gao and co-workers in 2011, **[Er(COT)(Cp*)]** was one of the first reported organometallic SMMs, and the first to harness arenide ligands to stabilise the single-ion anisotropy of a Lanthanide (III) ion.[146,147] This neutral complex comprises a Lanthanide (III) centre coordinated to an η^5-Cp* and an η^8-COT^{2-} ligand in a bent geometry with C_s point group symmetry. The dynamic magnetic properties were examined for Ln = terbium, dysprosium, holmium, erbium, and thulium, with the erbium metallocene showing the highest performance. This complex was shown to relax through two thermally activated processes, with U_{eff} = 136 and 223 cm^{-1}, and showed open hysteresis below 5 K. The high performance of the erbium congener was rationalised as the prolate electron density of its $^4I_{15/2}$ m_J microstate is stabilised by the relatively broad, equatorial CF imposed by the bulky COT^{2-} ligand. Follow-up investigations of homoleptic COT^{2-} sandwiches by us[148,149] and others[150] have corroborated this.

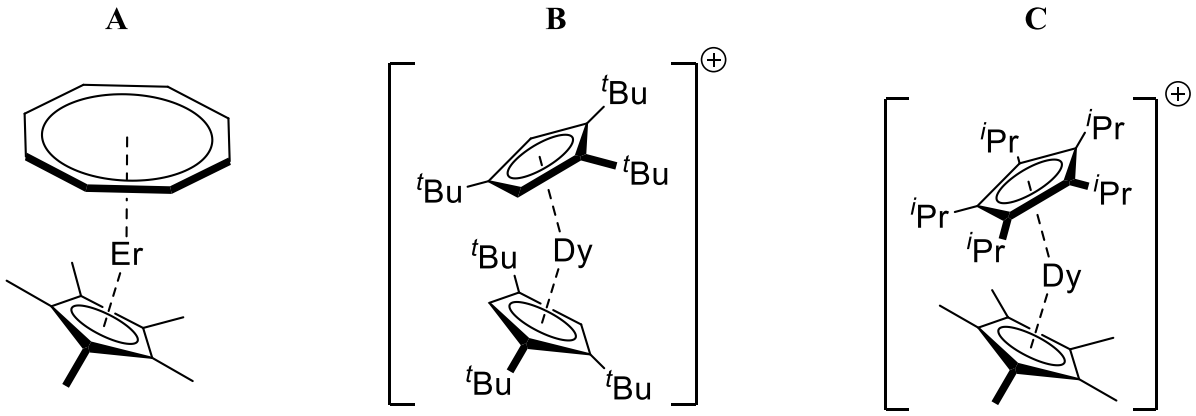

Figure 1.9 - Chemdraw representations of three milestone organometallic SIMs: [ErCOTCp*] (**A**), $[DyCp^{ttt}_2]^+$ (**B**), and $[Cp^*Dy(Cp^{ipr5})]^+$ (**C**).

Shown next is the first of the so-called "Dysprosocenium" class of organometallic SMMs, whose design was based on utilising a two identical Cp ligands to create a low-coordinate, pseudoaxial CF which would stabilise the highly anisotropic oblate CF ground state of a dysprosium (III) ion.[151–154]It is suggested that the smaller ring size of Cp compared to COT would offer a more narrow distribution of electron density, removing transverse interactions and better approximating a pseudolinear CF. **$[Dy(Cp^{ttt})_2][B(C_6F_5)_4]$** created a paradigm shift in organometallic Lanthanide chemistry, as it displayed open hysteresis up to 60 K with moderate sweep rates and an energy barrier of 1223 cm^{-1}. Prior to this, the highest blocking temperature reported was 14 K.[155] *Ab initio* calculations support these results, and show that the lowest 8 Kramer's Doublets (KDs) possess near-perfect uniaxial anisotropy with pure microstates.

The final example represents the current record in blocking temperature for an SMM. By considering the balance between the arenide-metal distance and the bending angle, a heteroleptic sandwich was designed to maximise the strength of the metal-ligand interaction while retaining a low-coordinate axial CF. Reported in 2018 by Layfield and Tong, **$[(Cp^*)Dy(Cp^{iPr5})][B(C_6F_5)_4]$** shows open hysteresis until 80 K with moderate sweep rates, above the boiling point of liquid nitrogen, and has an effective energy barrier of U_{eff} = 1541 cm^{-1}. The smaller Cp* size allows the two rings to approach slightly closer than in the

original Dysprosocenium complex, which is invoked as an explanation for the improved magnetic performance, in addition to the higher symmetry environment.[156]

While staggering results have been obtained using substituted cyclopentadieneide ligands, recent computational studies have questioned the gains from further functionalisation of the Dysprosocenium family. Instead, focus should instead move to the intramolecular origin of spin-phonon coupling and developing strategies to supress it.[115,117,157–159] *ab initio* methods that can describe the spin-phonon coupling in molecular systems were only developed recently,[108,109,112,160] and the first *ab initio* model that can accurately describe one and two phonon processes was reported this year.[161]

1.4 Cyclobutadiene Organometallic Chemistry:

Cyclobutadiene (Cb) metal complexes were predicted in 1956 by Longuet-Higgins and Orgel,[162] four years before the first structurally authenticated example in an Iron carbonyl complex by Dodge and Schomaker at Union Carbide Research Institute NY.[163] The neutral cyclobutadiene ring has an unstable antiaromatic 4π electron configuration (*vide supra*), and it was predicted that coordination to a d-block metal would lower the energy of the Cb MOs to give a stable singlet ground state.[164] Criegee and Schröder's route (**Scheme 1.3 A**) was the first developed, and leveraged the reductive dehalogenation of a 1,2-dihalocyclobutenes in the presence of TM carbonyl species under a nitrogen atmosphere to yield TM cyclobutadiene carbonyl complexes.[165,166] In the case of highly reductive TMs, such as zerovalent nickel, the reduction and coordination occur in one step without the need for an external reductant, such as sodium amalgam, yielding the structurally authenticated metal-halide cyclobutadiene pianostool complex, [$CbNiCl_2$].[167] A significant development in this chemistry was made by Nakamura and Hagihara, who reported the [2+2] cyclisation of alkynes mediated by TM cyclopentadienyl complexes under an inert atmosphere to yield cyclopentadienyl – cyclobutadiene mixed sandwich complexes (**Scheme 1.3 B**).[168,169] This route offers a greater substrate scope, as alkyl, aryl, and hetero-substituted alkynes can be used to prepare a range of substituted cyclobutadienes. However, the drawback to these two routes is the extreme air, moisture, and light sensitivity of these reactions, both of which must be conducted under strict Schlenk conditions. A significant advancement was described by Blomquist and Maitliss, who reported the synthesis of palladium cyclobutadiene chloride dimers in alcoholic solvents under ambient conditions (**Scheme 1.3 C**).[170] Their synthetic route utilised palladium (II) to couple bulky aryl-substituted alkynes under mild conditions to yield the bench-stable ethoxy-cyclobutenyl dimer complex, which can be converted into the cyclobutadiene dimer *via* protonolysis with HCl gas in organic solvents.

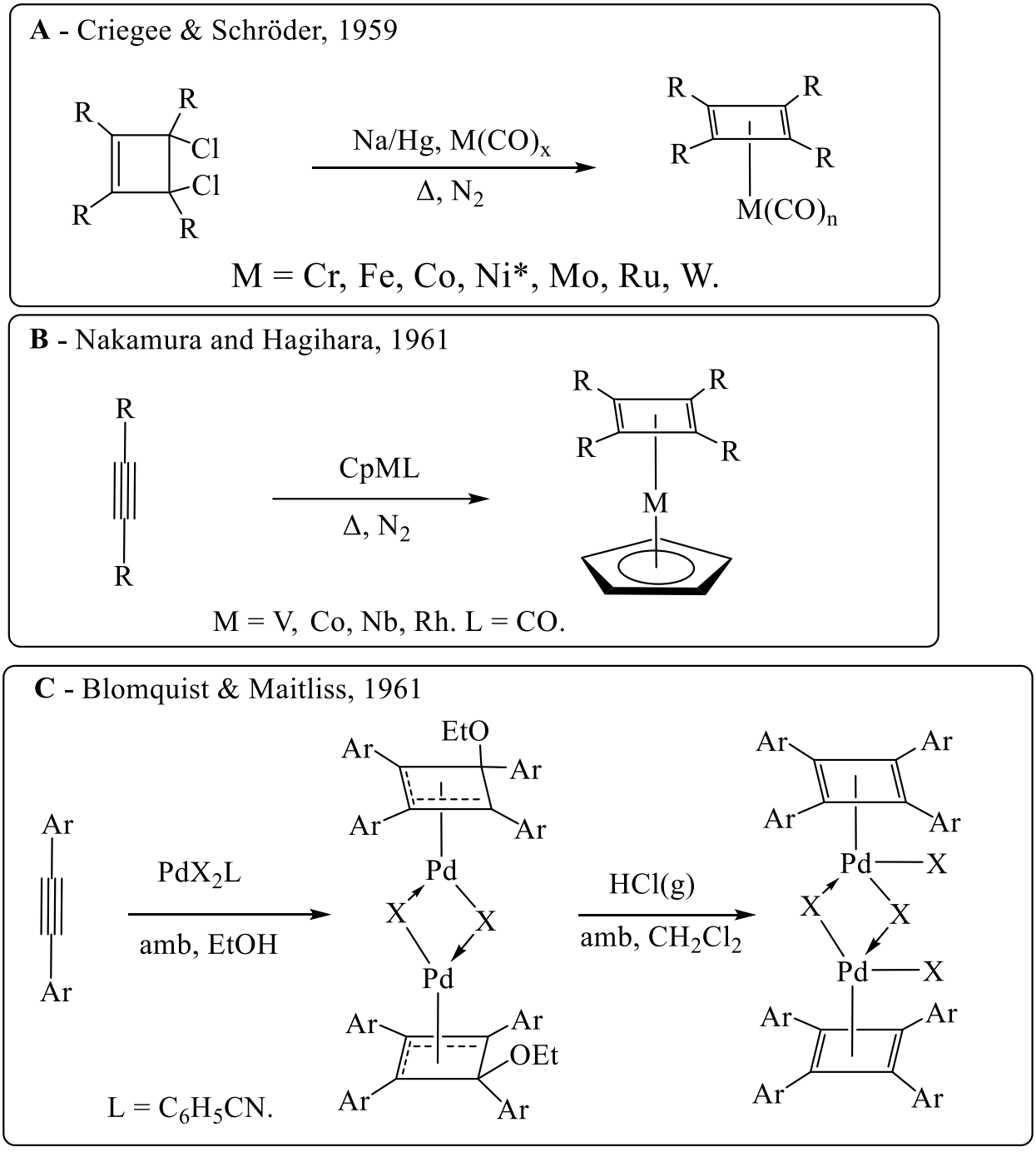

Scheme 1.3 - Synthetic schemes describing some routes to cyclobutadiene metal complexes. Reductive dehalogenation of dihalocyclobutene in the presence of TM carbonyls under an inert atmosphere, reported by Criegee and Schroder (**A**). *For highly reducing TMs, such as Ni(0), an external reductant such as sodium amalgam is not required. [2+2] cyclisation of acetylenes in the presence of cyclopentadienyl TM complexes under an inert atmosphere, reported by Nakamura and Hagihara (**B**). [2+2] cyclisation of acetylenes in the presence of palladium (II) and protonolysis under ambient condition, reported by Blomquist and Maitliss (**C**).

A detailed mechanism of the [2+2] alkyne cyclisation reaction was proposed in 2004 based on DFT methods, wherein the authors show that the thermodynamically stable TM

cyclobutadiene complexes are likely formed through unstable five-membered metallacyclic intermediates.[171] Utilising these routes, a number of TM cyclobutadiene systems have been investigated[172–176], however structurally-authenticated Cb metallocenes are rare, with the first and only reported example in a zerovalent nickel complex reported by Xi and co-workers in 2018.[177]

1.5 Cyclobutadienediide Organometallic Chemistry:

The Cb ring is also redox active[178], and has been demonstrated in a number of seminal reports by Sekiguchi and co-workers to form stable aromatic dianions when coordinated to Alkali metals, evidenced through SC-XRD analysis, NMR and MCD spectroscopies (**Scheme 1.4**).[179–182]

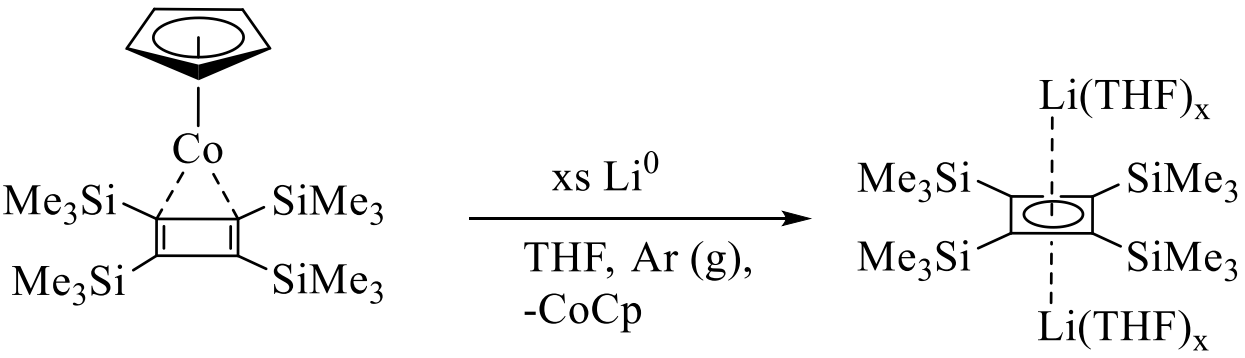

Scheme 1.4 - Synthetic scheme showing the synthesis of Li_2Cb'''' as reported by Sekiguchi and co-workers.

This elegant route leverages the strongly coordinating nature of lithium countercations to yield a cyclobutadienediide salt which can be easily purified by recrystallisation from hydrocarbon solvents. Indeed, this lithium-mediated reductive transmetallation is the only reported method to prepare cyclobutadienediide salts directly from TM complexes, and all further reported cyclobutadienediide salts have been prepared utilising the lithium salt.[183,184]

Cyclobutadienediide (Cb^{2-}) chemistry is notably different to neutral Cb chemistry; the dianion is extremely reactive, and was shown to reduce thorium (IV) into zerovalent metal by Liddle and co-workers recently.[185] Because of this, the organometallic chemistry of the dianionic cyclobutadienediide ring is currently limited only to high-valent Lanthanide and Actinide systems.[186] The Lanthanide Organometallic chemistry of cyclobutadienediide has begun to surge recently, as it was presumed that as the Cb ring is narrower than Cp it would offer a more linear CF to the metal centre. Additionally, the dianionic charge should provide a stronger interaction with the metal, giving greater CF splitting and higher energy separation between the CF microstates. These properties make dysprosium (III) cyclobutadienediide complexes highly attractive in the development of the next generation of high-performing SMMs. The reaction of $DyCl_3$ with potassium tetrakis(trimethylsilyl)cyclobutadienediide, [K_2Cb''''] in refluxing toluene (**Scheme 1.5 A**), was reported by Layfield and co-workers to yield a polymeric chain structure, wherein one of the trimethylsilyl groups had undergone C-H activation to yield a "tuck-in" coordination mode to the dysprosium centre.[187,188] They further report that when the sodium salt, [Na_2Cb''''] was utilised, further ligand activation was observed, as one of the cyclobutadienediide rings underwent protonation to form an {η^3-cyclobutenyl} moiety (**Scheme 1.5 B**).[189] As a consequence of the extreme reactivity of the Cb'''' dianion, no metallocenes of the cyclobutadienediides have been reported.

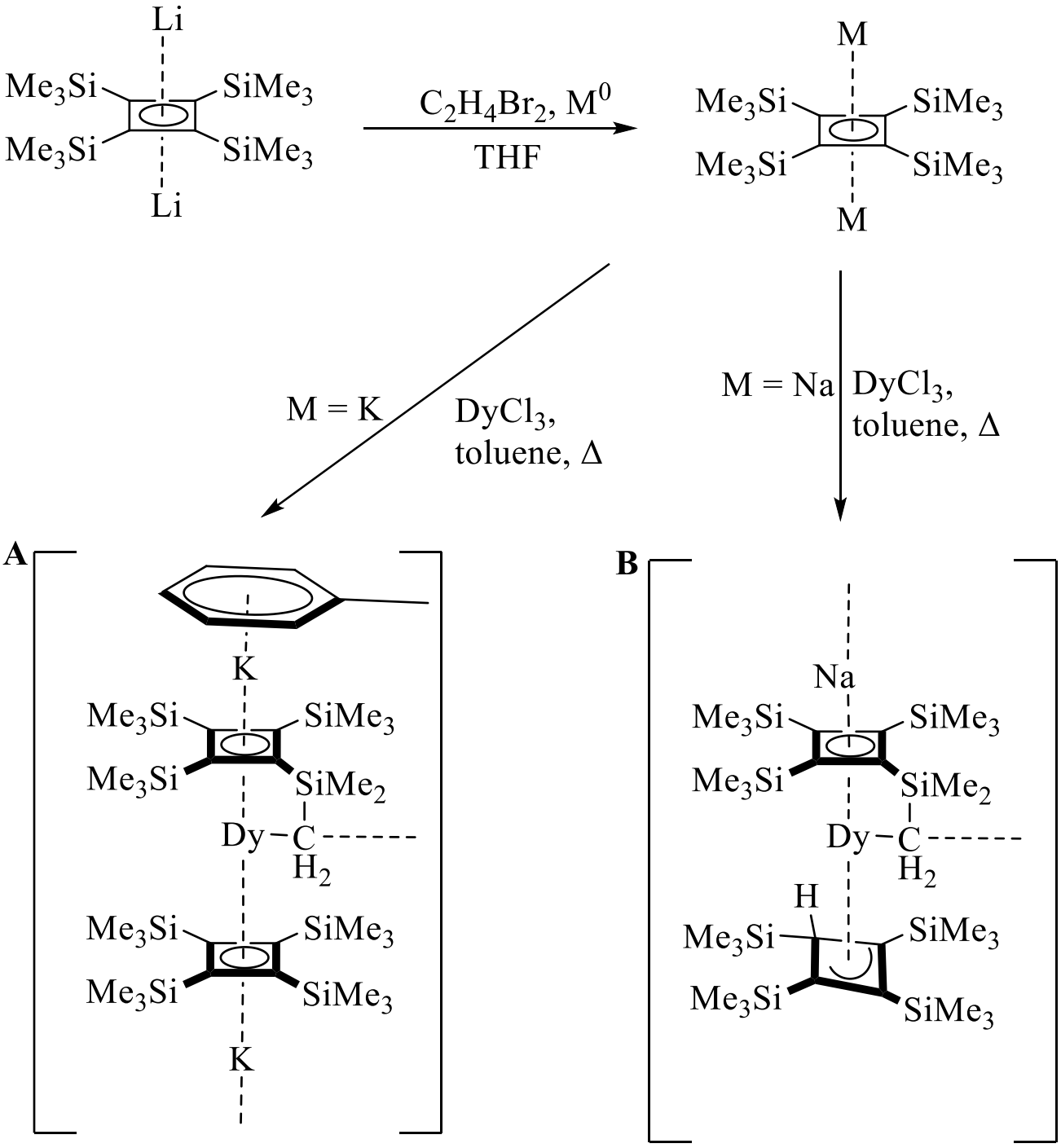

Scheme 1.5 - Synthetic scheme describing the preparation of [M2Cb’’’’] (M = Na, K), and the reaction of [K_2Cb’’’’] (**A**) or [Na_2Cb’’’’’] (**B**) with $DyCl_3$, reported by Layfield and co-workers.

Further synthetic efforts are therefore needed to design a stable dysprosium (III) Cb metallocene, which may compete with current “Dysprosocenium” class of high-performing SMMs.

1.6 Thesis scope:

As further modifications of the $[LnCp^{R}_{2}]^{+}$ framework may lead to minor improvements in T_B, we are turning our interest towards understanding the relationship between molecular structure and spin-phonon relaxation as this has been highlighted as an important area in the development of our understanding of spin-lattice relaxation. In chapter 2, we describe the structure and magnetisation dynamics of the low-symmetry dysprosium (III) Pianostool complex, [DyCp*(κ^3-BH_4)$_2$(THF)] and its borodeuteride congener [DyCp*(κ^3-BD_4)$_2$(THF)], to examine the effects of inner-sphere deuteration for the first time on an SMM.

The current organometallic chemistry of the cyclobutadiene dianion is limited to the tetrasilyl [Li_2Cb''''] moiety. We are interested in aryl-substituted derivatives, such as tetraphenylcyclobutadiene (Cb^{Ph4}), as these moieties may grant steric bulk, electronic delocalisation, and structural rigidity. In Chapter 3, we describe the synthesis and structural characterisation of the zerovalent palladium metallocene, [Pd(η^4-Cb^{Ph4})$_2$], through bond-metric analysis and group theory, we describe the possible bonding interactions within the complex, which can occur through σ-, π-, and δ - combinations. Continuing this, In Chapter 4, we describe the modified synthesis and isolation of [Li_2Cb^{cis}] and [Li_2Cb^{trans}] salts (Cb^{cis} = 1,2-bisphenyl-3,4-bis(trimethylsilyl)cyclobutadienediide, Cb^{trans} = 1,3-bispheny-2,4-bis(trimethylsilyl)cyclobutadienediide) and investigate their organometallic chemistry with Lanthanides for the first time. In chapter 5, we aim to investigate the polymeric nature of Lanthanide Cb complexes by utilising bulky cyclic organohydroboranes as co-ligands and isolate a monomeric Lanthanide cyclobutadienediide complex. Finally, in Chapter 6 we describe efforts towards Cb homoleptic metallocenes with dysprosium to prepare high performance multinuiclear SMMs, discuss efforts to further expand the organometallic chemistry of cyclobutadiene and give perspective to future studies.

1.7 References:

1 T. E. Graedel, E. M. Harper, N. T. Nassar and B. K. Reck, *Proc. Natl. Acad. Sci. U. S. A.*, 2015, **112**, 6295–6300.

2 A. Greenfield and T. E. Graedel, *Resour. Conserv. Recycl.*, 2013, **74**, 1–7.

3 B. Rohrig, *ChemMatters*, 2015, 10–12.

4 J. D. Widmer, R. Martin and M. Kimiabeigi, *Sustain. Mater. Technol.*, 2015, **3**, 7–13.

5 J. Magano and J. R. Dunetz, *RSC Catal. Ser.*, 2015, 697–778.

6 B. Matthias and H. U. Blaser, in *Organometallics as Catalysts in the Fine Chemical Industry*, Springer, Berlin, Heidelberg, 2012, pp. 1–35.

7 J. P. Corbet and G. Mignani, *Chem. Rev.*, 2006, **106**, 2651–2710.

8 N. Miyaura and A. Suzuki, *Chem. Rev.*, 1995, **95**, 2457–2483.

9 A. Dieck and R. F. Heck, *J. Am. Chem. Soc.*, 1974, **96**, 1133–1136.

10 E. Negishi, 1982, 340–348.

11 A. S. Guram, R. A. Rennels and S. L. Buchwald, *Angew. Chem. Int. Ed. English*, 1995, **34**, 1348–1350.

12 C. C. C. Johansson Seechurn, M. O. Kitching, T. J. Colacot and V. Snieckus, *Angew. Chem. - Int. Ed.*, 2012, **51**, 5062–5085.

13 P. G. Gildner and T. J. Colacot, *Organometallics*, 2015, **34**, 5497–5508.

14 T. E. Graedel, E. M. Harper, N. T. Nassar, P. Nuss, B. K. Reck and B. L. Turner, *Proc. Natl. Acad. Sci. U. S. A.*, 2015, **112**, 4257–4262.

15 S. Glöser, L. Tercero Espinoza, C. Gandenberger and M. Faulstich, *Resour. Policy*, 2015, **44**, 35–46.

16 N. T. Nassar, T. E. Graedel and E. M. Harper, *Sci. Adv.*, 2015, **1**, 1–11.

17 A. L. Gulley, N. T. Nassar and S. Xun, *Proc. Natl. Acad. Sci. U. S. A.*, 2018, **115**, 4111–4115.

18 J. C. G. Bünzli, *J. Lumin.*, 2016, **170**, 866–878.

19 S. J. Butler, M. Delbianco, L. Lamarque, B. K. Mcmahon, E. R. Neil, R. Pal, D. Parker, J. W. Walton and J. M. Zwier, *Dalton Trans.*, 2015, **44**, 4791–4803.

20 E. G. Moore, A. P. S. Samuel and K. N. Raymond, *Acc. Chem. Res.*, 2009, **42**, 542–552.

21 B. T. Kilbourn, *Inorg. Chim. Acta*, 1987, **140**, 335–338.

22 J. M. D. Coey, *Engineering*, 2020, **6**, 119–131.

23 X. Du and T. E. Graedel, *Sci. Total Environ.*, 2013, **461**–**462**, 781–784.

24 V. Balaram, *Geosci. Front.*, 2019, **10**, 1285–1303.

25 European Commission, *Critical Raw Materials Resilience: Charting a Path towards greater Security and Sustainability EN*, 2021.

26 US Department of Energy, *Report on Rare Earth Elements from Coal and Coal Byproducts*, 2017.

27 International Energy Agency (IEA), *The Role of Critical Minerals in Clean Energy Transitions*, 2021.

28 F. A. Cotton, G. Wilkin, C. A. Murillo and M. Bochmann, *Advanced Inorganic Chemistry*, 3rd edn., 199AD.

29 M. D. Rausch and R. A. Genetti, *J. Org. Chem.*, 1970, **35**, 3888–3897.

30 F. A. Cotton, *Inorg. Chem.*, 2002, **41**, 643–658.

31 M. N. Hopkinson, C. Richter, M. Schedler and F. Glorius, *Nature*, 2014, **7506**, 485–496.

32 R. H. Crabtree, *J. Organomet. Chem.*, 2005, **690**, 5451–5457.

33 G. Gasser and N. Metzler-Nolte, *Curr. Opin. Chem. Biol.*, 2012, **16**, 84–91.

34 A. L. Noffke, A. Habtemariam, A. M. Pizarro and P. J. Sadler, *Chem. Commun.*, 2012, **48**, 5219–5246.

35 D. A. Valyaev, G. Lavigne and N. Lugan, *Coord. Chem. Rev.*, 2016, **308**, 191–235.

36 D. Y. Wang, R. Liu, W. Guo, G. Li and Y. Fu, *Coord. Chem. Rev.*, 2021, **429**, 213650.

37 S. C. Bart and E. J. Schelter, *Organometallics*, 2017, **36**, 4507–4510.

38 N. Tsoureas, O. T. Summerscales, F. G. N. Cloke and S. M. Roe, *Organometallics*, 2013, **32**, 1353–1362.

39 S. A. Johnson and S. C. Bart, *Dalton Trans.*, 2015, **44**, 7710–7726.

40 S. T. Liddle, *Angew. Chem. - Int. Ed.*, 2015, **54**, 8604–8641.

41 J. S. Griffith, .

42 F. Aquilante, J. Autschbach, R. K. Carlson, L. F. Chibotaru, M. G. Delcey, L. De Vico, I. Fdez. Galván, N. Ferré, L. M. Frutos, L. Gagliardi, M. Garavelli, A. Giussani, C. E. Hoyer, G. Li Manni, H. Lischka, D. Ma, P. Å. Malmqvist, T. Müller, A. Nenov, M. Olivucci, T. B. Pedersen, D. Peng, F. Plasser, B. Pritchard, M. Reiher, I. Rivalta, I. Schapiro, J. Segarra-Martí, M. Stenrup, D. G. Truhlar, L. Ungur, A. Valentini, S. Vancoillie, V. Veryazov, V. P. Vysotskiy, O. Weingart, F. Zapata and R. Lindh, *J. Comput. Chem.*, 2016, **37**, 506–541.

43 L. Ungur and L. F. Chibotaru, *Lanthanides Actinides Mol. Magn.*, 2015, 153–184.

44 L. Ungur and L. F. Chibotaru, *Chem. Eur. J.*, 2017, **23**, 3708–3718.

45 D. Parker, E. A. Suturina, I. Kuprov and N. F. Chilton, *Acc. Chem. Res.*, 2020, **53**, 1520–1534.

46 R. Breslow, *Acc. Chem. Res.*, 1973, **6**, 393–398.

47 M. Solà, *Front. Chem.*, 2013, **1**, 4–11.

48 J. Henle, T. American, M. Monthly and N. Jan, *J. Am. Chem. Soc.*, 1964, 2530–2531.

49 L. J. Karas and J. I.-C. Wu, *Antiaromatic compounds: a brief history, applications,*

and the many ways they escape antiaromaticity, Elsevier Ltd., First Edit., 2021.

50 R. Gershoni-Poranne and A. Stanger, *Chem. Soc. Rev.*, 2015, **44**, 6597–6615.

51 P. R. Mitchell and R. V. Parish, *J. Chem. Educ.*, 1969, **46**, 811–814.

52 J. E. Ellis, *J. Organomet. Chem.*, 1975, **86**, 1–56.

53 A. G. Freeman, *Chem Rev*, 2000, **100**, 717–774.

54 J. Jin, T. Yang, K. Xin, G. Wang, X. Jin, M. Zhou and G. Frenking, *Angew. Chem. - Int. Ed.*, 2018, **57**, 6236–6241.

55 A. F. Littke and G. C. Fu, *Angew. Chem. - Int. Ed.*, 2002, **41**, 4176–4211.

56 S. S. Zalesskiy and V. P. Ananikov, *Organometallics*, 2012, **31**, 2302–2309.

57 A. R. Kapdi, A. C. Whitwood, D. C. Williamson, J. M. Lynam, M. J. Burns, T. J. Williams, A. J. Reay, J. Holmes and I. J. S. Fairlamb, *J. Am. Chem. Soc.*, 2013, **135**, 8388–8399.

58 I. J. S. Fairlamb, A. R. Kapdi and A. F. Lee, *Org. Lett.*, 2004, **6**, 4435–4438.

59 I. J. S. Fairlamb and A. F. Lee, *Organometallics*, 2007, **26**, 4087–4089.

60 I. J. S. Fairlamb, *Org. Biomol. Chem.*, 2008, **6**, 3645–3656.

61 G. Allegra, A. Immirzi and L. Porri, *J. Am. Chem. Soc.*, 1965, **87**, 1394–1395.

62 G. Allegra, G. T. Casagrande, A. Immirzi, L. Porri and G. Vitulli, *J. Am. Chem. Soc.*, 1970, **92**, 289–293.

63 E. L. Muetterties, J. R. Bleeke, E. J. Wucherer and T. A. Albright, *Chem. Rev.*, 1982, **82**, 499–525.

64 W. Dai, M. J. Chalkley, G. W. Brudvig, N. Hazari, P. R. Melvin, R. Pokhrel and M. K. Takase, *Organometallics*, 2013, **32**, 5114–5127.

65 E. S. Rudakov and G. B. Shul'pin, *J. Organomet. Chem.*, 2018, **867**, 25–32.

66 J. Åkerstedt, M. Gorlov, A. Fischer and L. Kloo, *J. Organomet. Chem.*, 2010, **695**, 1513–1517.

67 Y. Ishikawa, S. Kimura, K. Takase, K. Yamamoto, Y. Kurashige, T. Yanai and T. Murahashi, *Angew. Chemie*, 2015, **127**, 2512–2516.

68 M. Gorlov, A. Fischer and L. Kloo, *Inorg. Chim. Acta*, 2003, **350**, 449–454.

69 M. Gorlov, A. Fischer and L. Kloo, *Inorg. Chim. Acta*, 2009, **362**, 605–609.

70 H. M. Senn and T. Ziegler, *Organometallics*, 2004, **23**, 2980–2988.

71 T. Murahashi, E. Mochizuki, Y. Kai, and H. Kurosawa, *J. Am. Chem. Soc.*, 1999, 121, 45, 10660-10661.

72 T. Murahashi, T. Otani, T. Okuno and H. Kurosawa, *Angew. Chem. - Int. Ed.*, 2000, **39**, 537–540.

73 M. Yamashita, S. Horiuchi, K. Yamamoto and T. Murahashi, *Dalton Trans.*, 2019, **48**, 13149–13153.

74 S. Horiuchi, Y. Tachibana, M. Yamashita, K. Yamamoto, K. Masai, K. Takase, T. Matsutani, S. Kawamata, Y. Kurashige, T. Yanai and T. Murahashi, *Nat. Commun.*, 2015, **6**, 1–8.

75 M. Yamashita, Y. Kawasumi, Y. Tachibana, S. Horiuchi, K. Yamamoto and T. Murahashi, *Chem. Eur. J.*, 2019, **25**, 1212–1216.

76 Y. Ishikawa, K. Yamamoto and T. Murahashi, *Angew. Chem. - Int. Ed.*, 2017, **56**, 1346–1350.

77 T. Murahashi, R. Inoue, K. Usui and S. Ogoshi, *J. Am. Chem. Soc.*, 2009, **131**, 9888–9889.

78 M. Teramoto, K. Iwata, H. Yamaura, K. Kurashima, K. Miyazawa, Y. Kurashige, K. Yamamoto and T. Murahashi, *J. Am. Chem. Soc.*, 2018, **140**, 12682–12686.

79 G. Aromí, *Comments Inorg. Chem.*, 2011, **32**, 163–194.

80 C. Bin Yu, H. D. Wang, B. Song, H. Q. Shen, H. J. Fan and Y. G. Zhou, *Sci. China Chem.*, 2020, **63**, 215–221.

81 Q. Liu and L. Zhao, *Chin. J. Chem.*, 2020, **38**, 1897–1908.

82 T. Murahashi, K. Shirato, A. Fukushima, K. Takase, T. Suenobu, S. Fukuzumi, S. Ogoshi and H. Kurosawa, *Nat. Chem.*, 2012, **4**, 52–58.

83 W. J. Evans, *Organometallic Lanthanide Chemistry*, 1985, vol. 24.

84 K. E. Hyde, *J. Chem. Educ.*, 1975, **52**, 90–91.

85 J.-C. G. Bunzli and S. V. Eliseeva, *Basics of Lanthanide Photophysics*, 2010.

86 S. Wen, J. Zhou, K. Zheng, A. Bednarkiewicz, X. Liu and D. Jin, *Nat. Commun.*, , DOI:10.1038/s41467-018-04813-5.

87 D. A. Gálico, J. S. Ovens, F. A. Sigoli and M. Murugesu, *ACS Nano*, 2021, **15**, 5580–5585.

88 R. Marin, G. Brunet and M. Murugesu, *Angew. Chem. Int. Ed.*, 2019, 60, 4, 1728-1746.

89 L. Sorace and D. Gatteschi, *Lanthanides Actinides Mol. Magn.*, 2015, **2**, 1–26.

90 B. M. Day, F. S. Guo and R. A. Layfield, *Acc. Chem. Res.*, 2018, **51**, 1880–1889.

91 W. J. Evans, *Organometallics*, 2016, **35**, 3088–3100.

92 P. B. Hitchcock, M. F. Lappert, L. Maron and A. V. Protchenko, *Angew. Chem. - Int. Ed.*, 2008, **47**, 1488–1491.

93 M. R. Macdonald, J. E. Bates, J. W. Ziller, F. Furche and W. J. Evans, *J. Am. Chem. Soc.*, 2013, 9857–9868.

94 M. R. MacDonald, J. E. Bates, M. E. Fieser, J. W. Ziller, F. Furche and W. J. Evans, *J. Am. Chem. Soc.*, 2012, **134**, 8420–8423.

95 M. E. Fieser, M. G. Ferrier, J. Su, E. Batista, S. K. Cary, J. W. Engle, W. J. Evans, J. S. Lezama Pacheco, S. A. Kozimor, A. C. Olson, A. J. Ryan, B. W. Stein, G. L. Wagner, D. H. Woen, T. Vitova and P. Yang, *Chem. Sci.*, 2017, **8**, 6076–6091.

96 G. Meyer, *J. Solid State Chem.*, 2019, **270**, 324–334.

97 R. Sessoli, *Nature*, 2017, **548**, 400–401.

98 P. D. Boyd, Q. Li, J. B. Vincent, K. Folting, H.-R. Chang, W. E. Streib, J. C. Huffman, G. Christou and D. N. Hendrickson, *J. Am. Chem. Soc.*, 1988, **110**, 8537–8539.

99 A. Caneschi, D. Gatteschi and R. Sessoli, *J. Am. Chem. Soc.*, 1991, 5873–5874.

100 R. Sessoli, H. Tsai, A. R. Schake, S. Wang, J. B. Vincent, K. Foiling, D. Gatteschi, G. Christou and D. N. Hendrickson, *J. Am. Chem. Soc.*, 1993, 1804–1816.

101 L. Thomas, F. Lionti, R. Ballou, D. Gatteschi, R. Sessoli and B. Barbara, *Nature*, 1996, **383**, 145–147.

102 M. Atzori and R. Sessoli, *J. Am. Chem. Soc.*, 2019, **141**, 11339–11352.

103 L. Ungur and L. F. Chibotaru, *Phys. Chem. Chem. Phys.*, 2011, **13**, 20086–20090.

104 A. Abragam and B. Bleaney, *Electron Paramagnetic Resonance of Transition Ions*, Clarendon Press, Oxford, 1970.

105 D. Aravena and E. Ruiz, *Dalton Trans.*, 2020, **49**, 9916–9928.

106 J. H. Van Vleck, *Phys. Rev.*, 1940, **57**, 426–447.

107 R. Orbach and P. R. S. L. A, *Proc. R. Soc. London. Ser. A. Math. Phys. Sci.*, 1961, **264**, 458–484.

108 L. Escalera-Moreno, N. Suaud, A. Gaita-Ariño and E. Coronado, *J. Phys. Chem. Lett.*, 2017, **8**, 1695–1700.

109 A. Lunghi, F. Totti, R. Sessoli and S. Sanvito, *Nat. Commun.*, 2017, **8**, 1–7.

110 L. Escalera-Moreno, J. J. Baldoví, A. Gaita-Ariño and E. Coronado, *Chem. Sci.*, 2018, **9**, 3265–3275.

111 D. H. Moseley, S. E. Stavretis, K. Thirunavukkuarasu, M. Ozerov, Y. Cheng, L. L. Daemen, J. Ludwig, Z. Lu, D. Smirnov, C. M. Brown, A. Pandey, A. J. Ramirez-Cuesta, A. C. Lamb, M. Atanasov, E. Bill, F. Neese and Z. L. Xue, *Nat. Commun.*, 2018, **9**, 1–11.

112 A. Lunghi, F. Totti, S. Sanvito and R. Sessoli, *Chem. Sci.*, 2017, **8**, 6051–6059.

113 S. T. Liddle and J. Van Slageren, *Chem. Soc. Rev.*, 2015, **44**, 6655–6669.

114 X. Feng, J. L. Liu, K. S. Pedersen, J. Nehrkorn, A. Schnegg, K. Holldack, J. Bendix, M. Sigrist, H. Mutka, D. Samohvalov, D. Aguilà, M. L. Tong, J. R. Long and R. Clérac, *Chem. Commun.*, 2016, **52**, 12905–12908.

115 Y. S. Ding, T. Han, Y. Q. Zhai, D. Reta, N. F. Chilton, R. E. P. Winpenny and Y. Z. Zheng, *Chem. Eur. J.*, 2020, 26,26, 5893-5902.

116 A. Castro-Alvarez, Y. Gil, L. Llanos and D. Aravena, *Inorg. Chem. Front.*, , DOI:10.1039/d0qi00487a.

117 A. Chiesa, F. Cugini, R. Hussain, E. Macaluso, G. Allodi, E. Garlatti, M. Giansiracusa, C. A. P. Goodwin, F. Ortu, D. Reta, J. M. Skelton, T. Guidi, P. Santini, M. Solzi, R. De Renzi, D. P. Mills, N. F. Chilton and S. Carretta, *Phys. Rev. B*, 2020, **174402**, 1–9.

118 L. Ungur and L. F. Chibotaru, *Inorg. Chem.*, 2016, **55**, 10043–10056.

119 A. Castro-Alvarez, Y. Gil, L. Llanos and D. Aravena, *Inorg. Chem. Front.*, 2020, **7**, 2478–2486.

120 A. Lunghi and S. Sanvito, *J. Phys. Chem. Lett.*, 2020, **11**, 6273–6278.

121 F. Luis, M. J. Martínez-Pérez, O. Montero, E. Coronado, S. Cardona-Serra, C. Martí-Gastaldo, J. M. Clemente-Juan, J. Sesé, D. Drung and T. Schurig, *Phys. Rev. B - Condens. Matter Mater. Phys.*, 2010, **82**, 3–6.

122 A. Gaita-Ariño, F. Luis, S. Hill and E. Coronado, *Nat. Chem.*, 2019, **11**, 301–309.

123 J. L. Liu, Y. C. Chen and M. L. Tong, *Chem. Soc. Rev.*, 2018, **47**, 2431–2453.

124 S. K. Gupta and R. Murugavel, *Chem. Commun.*, 2018, **54**, 3685–3696.

125 H. A. Kramers, *Kon. Ned. Akad. Wetensch. Proc.*, 1930, **33**, 959–972.

126 F. Ortu, D. Reta, Y. S. Ding, C. A. P. Goodwin, M. P. Gregson, E. J. L. McInnes, R. E. P. Winpenny, Y. Z. Zheng, S. T. Liddle, D. P. Mills and N. F. Chilton, *Dalton Trans.*, 2019, **48**, 8541–8545.

127 S. Gómez-Coca, A. Urtizberea, E. Cremades, P. J. Alonso, A. Camón, E. Ruiz and F. Luis, *Nat. Commun.*, 2014, **5**, 1–8.

128 S. T. Liddle and J. Van Slageren, *Chem. Soc. Rev.*, 2015, **44**, 6655–6669.

129 G. Handzlik, M. Magott, M. Arczyński, A. M. Sheveleva, F. Tuna, S. Baran and D. Pinkowicz, *Dalton Trans.*, 2020, **49**, 11942–11949.

130 L. Gu and R. Wu, *Phys. Rev. B*, 2021, **103**, 1–9.

131 M. Buchner, K. Höfler, B. Henne, V. Ney and A. Ney, *J. Appl. Phys.*, 2018, **124**, 1–13.

132 J. Clarke, *Sci. Amer.*, 1994, **271**, 46–53.

133 G. A. Bain and J. F. Berry, *J. Chem. Educ.*, 2008, **85**, 532–536.

134 D. A. Gálico, R. Marin, G. Brunet, D. Errulat, E. Hemmer, F. A. Sigoli, J. O. Moilanen and M. Murugesu, *Chem. Eur. J.*, 2019, **25**, 14625–14637.

135 R. J. Blagg, L. Ungur, F. Tuna, J. Speak, P. Comar, D. Collison, W. Wernsdorfer, E. J. L. McInnes, L. F. Chibotaru and R. E. P. Winpenny, *Nat. Chem.*, 2013, **5**, 673–678.

136 C. Benelli and D. Gatteschi, *Introduction to Molecular Magnetism, Wiley-VHC*, 2015, Chapter 12, 195-215.

137 D. Reta and N. F. Chilton, *Phys. Chem. Chem. Phys.*, 2019, **21**, 23567–23575.

138 L. T. A. Ho and L. F. Chibotaru, *Phys. Rev. B*, 2016, **94**, 1–5.

139 J. Wu, S. Demeshko, S. Dechert and F. Meyer, *Chem. Commun.*, 2020, **56**, 3887–3890.

140 K. L. M. Harriman, D. Errulat and M. Murugesu, *Trends Chem.*, 2019, **1**, 425–439.

141 J. D. Rinehart and J. R. Long, *Chem. Sci.*, 2011, **2**, 2078–2085.

142 J. L. Liu, Y. C. Chen and M. L. Tong, *Chem. Soc. Rev.*, 2018, **47**, 2431–2453.

143 Y. C. Chen, J. L. Liu, L. Ungur, J. Liu, Q. W. Li, L. F. Wang, Z. P. Ni, L. F. Chibotaru,

X. M. Chen and M. L. Tong, *J. Am. Chem. Soc.*, 2016, **138**, 2829–2837.

144 S. D. Jiang, B. W. Wang, H. L. Sun, Z. M. Wang, and S. Gao, *J. Am. Chem. Soc.*, 2011, 133, 13, 4730-4733.

145 F. S. Guo, B. M. Day, Y. C. Chen, M. L. Tong, A. Mansikkamäki and R. A. Layfield, *Science*, 2018, **362**, 1400–1403.

146 S. Da Jiang, B. W. Wang, H. L. Sun, Z. M. Wang and S. Gao, *J. Am. Chem. Soc.*, 2011, **133**, 4730–4733.

147 S. Da Jiang, S. S. Liu, L. N. Zhou, B. W. Wang, Z. M. Wang and S. Gao, *Inorg. Chem.*, 2012, **51**, 3079–3087.

148 L. Ungur, J. J. Le Roy, I. Korobkov, M. Murugesu and L. F. Chibotaru, *Angew. Chemie*, 2014, **126**, 4502–4506.

149 J. J. Le Roy, I. Korobkov and M. Murugesu, *Chem. Commun.*, 2014, **50**, 1602–1604.

150 K. R. Meihaus and J. R. Long, *J. Am. Chem. Soc.*, 2013, **135**, 17952–17957.

151 C. A. P. Goodwin, F. Ortu, D. Reta, N. F. Chilton and D. P. Mills, *Nature*, 2017, **548**, 439–442.

152 C. A. P. Goodwin, D. Reta, F. Ortu, N. F. Chilton and D. P. Mills, *J. Am. Chem. Soc.*, 2017, **139**, 18714–18724.

153 F. S. Guo, B. M. Day, Y. C. Chen, M. L. Tong, A. Mansikkamäki and R. A. Layfield, *Angew. Chem. - Int. Ed.*, 2017, **56**, 11445–11449.

154 C. A. P. Goodwin, D. Reta, F. Ortu, J. Liu, N. F. Chilton and D. P. Mills, *Chem. Commun.*, 2018, **54**, 9182–9185.

155 J. D. Rinehart, M. Fang, W. J. Evans and J. R. Long, *J. Am. Chem. Soc.*, 2011, **133**, 14236–14239.

156 A. Ullah, J. Cerdá, J. J. Baldoví, S. A. Varganov, J. Aragó and A. Gaita-Ariño, *J. Phys. Chem. Lett.*, 2019, **10**, 7678–7683.

157 C. A. P. Goodwin, *Dalton Trans.*, 2020, **49**, 14320–14337.

158 K. Randall McClain, C. A. Gould, K. Chakarawet, S. J. Teat, T. J. Groshens, J. R. Long and B. G. Harvey, *Chem. Sci.*, 2018, **9**, 8492–8503.

159 D. Reta, J. G. C. Kragskow and N. F. Chilton, *J. Am. Chem. Soc.*, 2021, **143**, 5943–5950.

160 A. Lunghi and S. Sanvito, *Sci. Adv.*, 2019, **5**, 1–8.

161 M. Briganti, F. Santanni, L. Tesi, F. Totti, R. Sessoli and A. Lunghi, *J. Am. Chem. Soc.*, , DOI:10.1021/jacs.1c05068.

162 H. C. Longuet-Higgins and L. E. Orgel, *J. Chem. Soc.*, 1956, 1969–1972.

163 R. P. Dodge and V. Schomaker, *Nature*, 1960, **186**, 798–799.

164 G. Ganguly, S. Pathak and A. Paul, *Phys. Chem. Chem. Phys.*, 2021, **23**, 16005–16012.

165 R. Criegee and G. Schröder, *Justus Liebigs Ann. Chem.*, 1959, **623**, 1–8.

166 J. D. Dunitz, H. C. Mez, O. . Mills and H. M. . Shearer, *Helv. Chim. Acta*, 1962, **45**, 647–665.

167 R. Criegee and G. Schröder, *Angew. Chemie*, 1959, **70**, 70–71.

168 A. Nakamura and N. Hagihara, *Bull. Chem. Soc. Jpn.*, 1961, **34**, 452–453.

169 H. Yamazaki and N. Hagihara, *J. Organomet. Chem.*, 1970, **21**, 431–443.

170 A. T. Blomquist and P. M. Maitlis, *J. Am. Chem. Soc.*, 1962, **84**, 2329–2334.

171 L. F. Veiros, G. Dazinger, K. Kirchner, M. J. Calhorda and R. Schmid, *Chem. Eur. J.*, 2004, **10**, 5860–5870.

172 A. EFRATY, *Chem. Rev.*, 1977, **77**, 691–740.

173 P. M. Maitlis, *J. Organomet. Chem.*, 1980, **200**, 161–176.

174 D. Seyferth, *Organometallics*, 2003, **22**, 2–20.

175 N. V. Shvydkiy and D. S. Perekalin, *Coord. Chem. Rev.*, 2017, **349**, 156–168.

176 D. Kumar, M. Deb, J. Singh, N. Singh, K. Keshav and A. J. Elias, *Coord. Chem. Rev.*, 2016, **306**, 115–170.

177 C. Yu, W. X. Zhang and Z. Xi, *Organometallics*, 2018, **37**, 4100–4104.

178 J. Wei, Y. Zhang, W. X. Zhang and Z. Xi, *Angew. Chem. - Int. Ed.*, 2015, **54**, 9986–9990.

179 A. Sekiguchi, T. Matsuo and W. Hidetoshi, *J. Am. Chem. Soc.*, 2000, **2**, 5652–5653.

180 A. Sekiguchi, T. Matsuo and M. Tanaka, *Organometallics*, 2002, **21**, 1072–1076.

181 T. Matsuo and A. Sekiguchi, *Bull. Chem. Soc. Jpn.*, 2004, **77**, 211–226.

182 K. Ishii, N. Kobayashi, T. Matsuo, M. Tanaka and A. Sekiguchi, *J. Am. Chem. Soc.*, 2001, **123**, 5356–5357.

183 K. Takanashi, A. Inatomi, V. Y. Lee, M. Nakamoto, M. Ichinohe and A. Sekiguchi, *Eur. J. Inorg. Chem.*, 2008, 1752–1755.

184 B. A. Shainyan and A. Sekiguchi, *J. Mol. Struct. THEOCHEM*, 2005, **728**, 1–5.

185 J. T. boronski, A. J. Wooles and S. T. Liddle, *Chem. Sci.*, 2020, **11**, 6789–6794.

186 J. T. boronski and S. T. Liddle, *Eur. J. Inorg. Chem.*, 2020, **2020**, 2851–2861.

187 A. Sekiguchi, M. Tanaka, T. Matsuo and H. Watanabe, *Angew. Chem. - Int. Ed.*, 2001, **40**, 1675–1677.

188 B. M. Day, F. S. Guo, S. R. Giblin, A. Sekiguchi, A. Mansikkamäki and R. A. Layfield, *Chem. Eur. J.*, 2018, **24**, 16779–16782.

189 A. Chakraborty, B. M. Day, J. P. Durrant, M. He, J. Tang and R. A. Layfield, *Organometallics*, 2020, **39**, 1, 8-12.

190 A. J. Freeman and R. E. Watson, *Phys. Rev.*, 1962, **127**, 2058

Chapter 2: Dysprosium Pianostool

2.1 Introduction:

Spin-phonon coupling is the process whereby paramagnetic spins relax to thermal equilibrium via dynamic modulation of crystal field interactions.[1,2] The intramolecular mechanism of spin-phonon coupling in paramagnetic salts was described phenomenologically by Van-Vleck and his contemporaries, however recent perspectives have highlighted the need for a more complete understanding of this dynamic process.[3–9]

Indeed, the role of spin-phonon coupling has come to the fore in the development of high performing single-molecule magnets (SMMS) and molecular quantum bits (qubits), as efficient spin-lattice relaxation represents one of the last hurdles in the implementation of quantum systems for next generation technologies.[9–12] In SMMS in particular, it has been shown that spin-phonon couplings arising from intramolecular vibrations can lead to through-barrier magnetic relaxation, negating the benefits of large energy barriers to spin reversal.[13–17]

We are interested in borohydride salts as precursors to organometallic lanthanide complexes, as these ligands may impart solubility, volatility, and their weakly-coordinating nature lends itself to functionalisation of the metal centre.[18] While f-element boron-coordinated compounds have had a renaissance over the past decade due to their efficacy as polymerisation catalysts,[19] we were surprised to find a scarcity of magnetic characterisation of these compounds.[14,20–24]

2.2 Results and discussion:

2.2.1 Synthesis:

The $[Cp^*_2Dy]^+$ motif is ubiquitous in molecular magnetism, as the strong, near-linear ligand field and high symmetry can promote magnetic relaxation through thermally activated pathways.[25–27]To investigate potential borohydride complexes as precursors to high-nuclearity magnetic systems, we synthesised the borohydride-supported dysprosium piano stool complex [DyCp*(κ^3-BH_4)$_2$(THF)] **2.1**, based on an analogous procedure developed by Ephritikhine and co-workers. Addition of one stoichiometric equivalent of KCp* to dysprosium borohydride in THF under reduced temperatures, followed by extraction into toluene, yielded pale-yellow block crystals of **2.1** in 75 % yield (**Scheme 2.1)**.

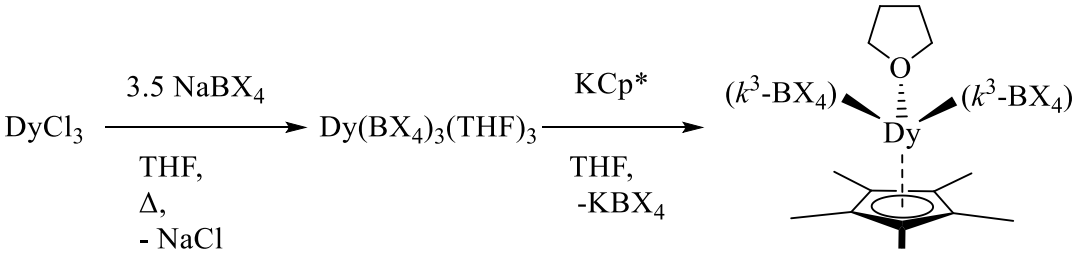

Scheme 2.1 - Synthetic scheme describing synthesis of compounds **2.1** [DyCp*(κ^3-BH_4)$_2$(THF)], and **2.2** [DyCp*(κ^3-BD_4)$_2$(THF)].

Working on the assumption that the B-H motif would lead to fast through-barrier relaxation *via* flexible intramolecular vibrational modes, we investigated whether the magnetisation dynamics could be manipulated through isotopic enrichment by preparing the hitherto unreported dysprosium borodeuteride salt, [Dy(BD_4)(THF)$_3$] (D = ^{2}H). While some of us have investigated the effects of outer-sphere isotopic enrichment on spin relaxation in

SMMs, this is, to the best of our knowledge, the first investigation of inner-sphere deuteration on the spin relaxation of an SMM. Substituting dysprosium borohydride with dysprosium borodeuteride yielded the isotopically enriched analogue [DyCp*(κ^3-BD_4)$_2$(THF)], **2.2**, in 78% yield.

2.2.2 Structural Analysis:

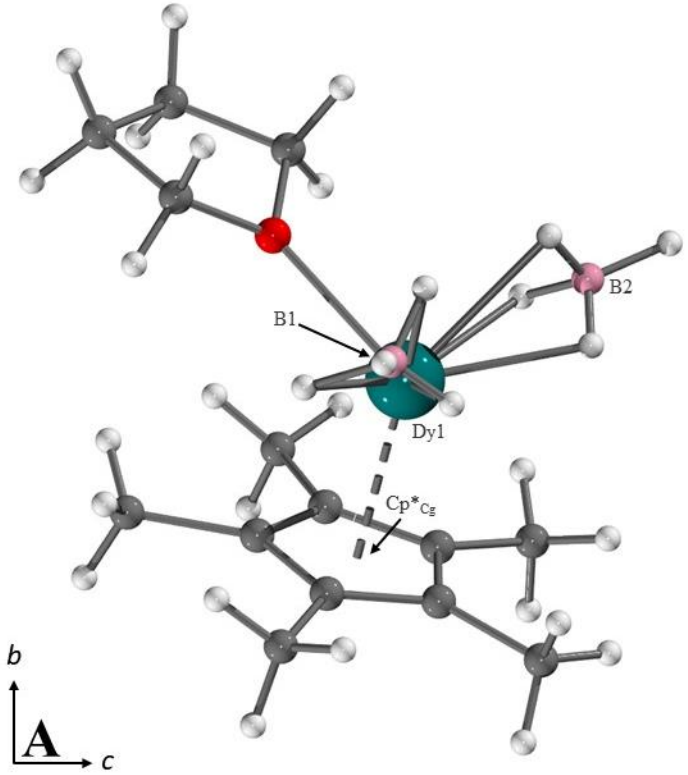

Figure 2.1 - Solid-state molecular structure of compound [DyCp*(κ^3-BH_4)$_2$(THF)] **2.1**. Colour code: grey = carbon, red = oxygen, white = hydrogen, teal = dysprosium, pink = boron.

Compound 2.1 crystallises in the orthorhombic space group Pmn21, with unit cell parameters a = 13.980(2) Å, b = 8.259(1) Å, c = 7.828(1) Å, $\alpha = \beta = \gamma = 90^o$, V = 902.7(2) Å^3, and two [DyCp*(κ^3-BH_4)$_2$(THF)] molecules in the unit cell. Each dysprosium centre is κ^3 bound to two borohydride ligands with Dy-B = 2.501(12) Å. The solid-state κ^3-BH_4 binding mode was investigated with FTIR spectroscopy (Figure A.1). A strong broad peak at 2470 cm^{-1}, in addition to a doublet band at 2150 and 2100 cm^{-1} have been previously assigned to the B-H stretches of the κ^3 coordination mode of BH_4. [28]A strong doublet between 2400-2600 cm^{-1} and a strong peak at 1650 – 2150 cm^{-1} would be expected if either of the BH_4 ligands exhibited κ^2 coordination in the solid state, neither of which is observed. These assignments have been corroborated in analogous systems.[29] The arenide is η^5 bound, and its centre of gravity, denoted Cp*$_{cg}$, is located Dy-Cp*$_{cg}$ = 2.334(5) Å from the metal centre. The coordination sphere is complete by a solvated THF molecule, which is commonly seen in lanthanide complexes without sterically demanding ligands due to their extreme Lewis acidity. The THF molecule is located Dy-O = 2.310(9) Å from the metal centre and makes an angle of $\angle$ Cp*$_{cg}$-Dy-O_{THF} = 161.8(2)^o with the arenide. The molecule lies on a crystallographic mirror plane which bisects the Dy centre, one methyl group of the Cp*

ligand, and the donor oxygen of the coordinated THF molecule. The shortest Dy-Dy distance within the lattice found to be equal to 8.216(1) Å.

Compound 2.2 was isostructural to **2.1**, with minimal differences in bond lengths and angles (**Table 2.1**). This can be visualised by overlaying the thermal ellipsoids of the two solid state molecular structures (**Figure 2.2**), showing the near identical models, which show RMS deviation of 6.56 $x10^{-3}$.

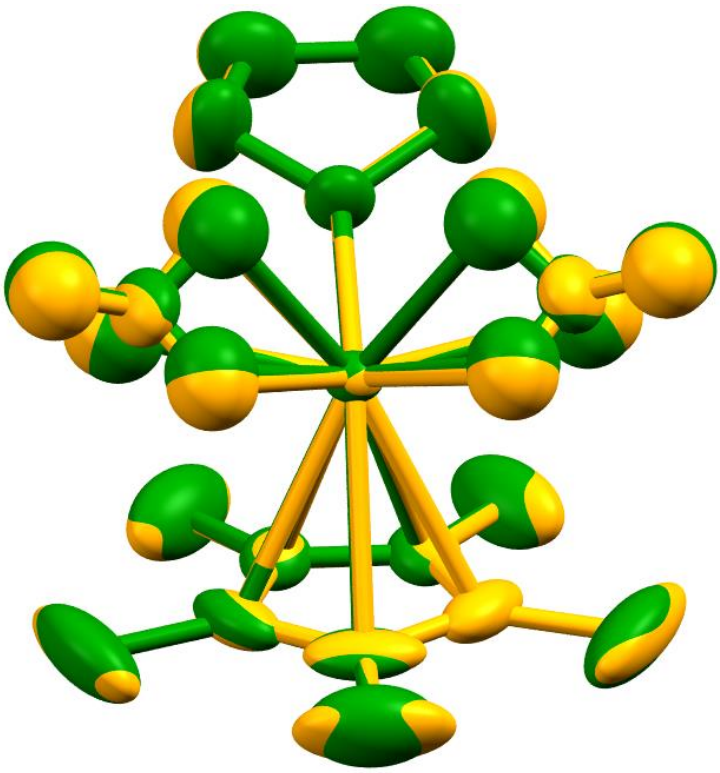

Figure 2.2 - Overlaid solid state molecular structures of **2.1** (Orange) and **2.2** (Green) at 273 K. Thermal ellipsoids rendered at 50 % probability level. Structures show a RMS deviation of 6.56 $x10^{-3}$. Non-coordinating hydrogen atoms were removed for clarity.

Table 2.1 - Selected interatomic distances in compounds **2.1** and **2.2.**

Complex	Distance/angle		Distance/angle
2.1			
Dy-O1	2.310(9)	B1-Dy-B1’	106.7(4)
Dy-B1	2.490(13)	O1-Dy-Cp*	161.8(2)
Dy-Cp*	2.342(7)	B1-Dy-Cp*	92.3(3)
O1-Dy-B1	98.5(3)		
2.2			
Dy-O1	2.334(5)	B1-Dy-B1’	107.3(18)
Dy-B1	2.510(6)	O1-Dy-Cp*	111.0(10)

Dy-Cp*	2.337(10)	B1-Dy-Cp*	118.7(15)
Dy-D1	2.196(7)	O1-Dy-B1	98.8(15)
Dy-D2	2.370(6)	B1-Dy-B1’	107.3(19)
Dy-D3	2.364(4)		

2.2.3 DC and AC Magnetism:

Direct current (DC) magnetic susceptibility measurements were carried out on polycrystalline samples of **2.1** and **2.2**. The temperature dependence of the $\chi_m T$ product of **2.1** and **2.2**, where χ_m represents the molar magnetic susceptibility, are shown in **Figure 2.3.** At 300 K, $\chi_m T$ products of 13.98 and 14.26 cm^3 K mol^{-1} are observed for **2.1** and **2.2**, respectively, which are in agreement with the expected values of 14.17 cm^3 K mol^{-1} for a single Dy^{III} ion ($4f^9$, $^6H_{15/2}$, S = 5/2, L = 5, g = 4/3). These values decrease with temperature due to depopulation of crystal-field excited states, until reaching minima of 10.86 and 11.56 cm^3 K mol^{-1} respectively below 5 K. The magnetisation and reduced magnetisation were probed between 1.9 and 7 K at fields from 0 to 70 000 Oersted (Oe), both reaching saturation above 5.0 μ_B, as expected for mononuclear Dy^{III} systems (Figures S5, S19). The shape and behaviour of the $\chi_m T$ measurements are in good agreement with the *ab initio* calculated susceptibilities (**Figure 2.4**).

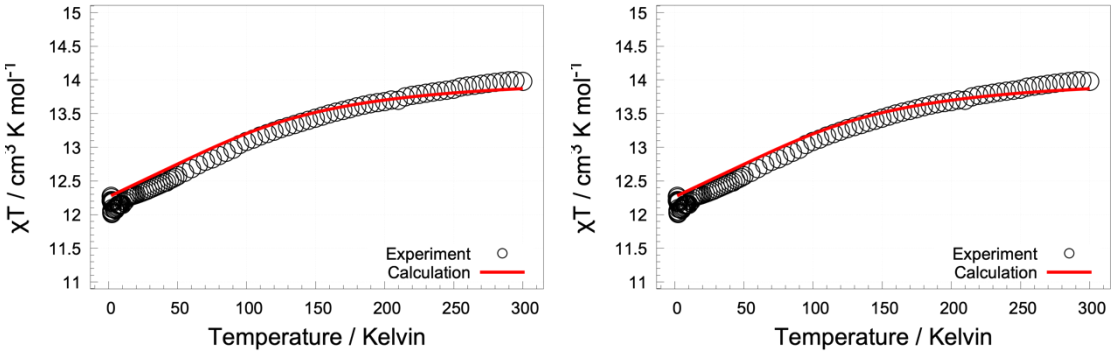

Figure 2.3 - Experimental (hollow circles) and calculated (red lines) temperature dependence of the Molar magnetic susceptibility in **2.1** (left) and **2.2** (right). Calculated using VQSP basis set and DFT optimised structures.

The dynamic magnetic properties of **2.1** and **2.2** were probed through alternating current (AC) magnetic susceptibility measurements. For compound **2.1**, the temperature dependence of the out-of-phase magnetic susceptibility, χ’’, in the absence of an applied magnetic field is shown in **Figure 2.4**. Frequency dependant peaks are seen from 1.8 to 25 K. No qualitative differences are seen in the out-of-phase or in-phase susceptibilities between **2.1** and **2.2**, suggesting the isotopic differences have little effect on the dominant spin relaxation pathways. By fitting each isothermal dataset to the generalised Debye model, the relaxation time, τ, at each temperature can be extracted (**Table A.6**). The best-fit τ values for **2.1** and **2.2** across the temperature range measured are between 2.2 ms and 0.1 ms, indicative of fast relaxation via quantum tunnelling of the magnetisation. The best-fit alpha values are in

the range of 0.13 – 0.09 for **2.1**, and 0.14 – 0.133 for **2.2**, each signifying a relatively narrow distribution of relaxation times across the temperature range.

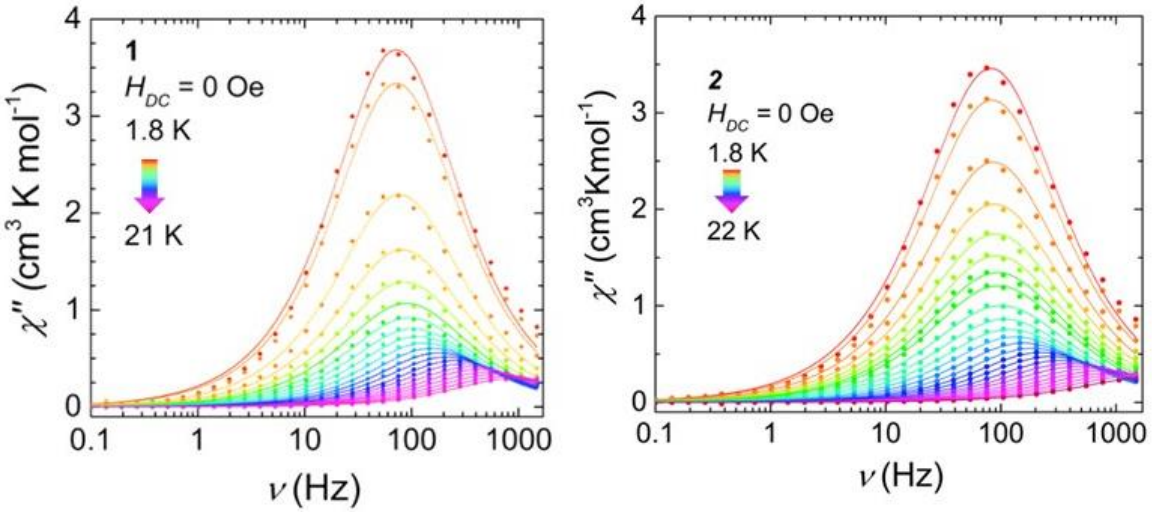

Figure 2.4 - Out-of-phase magnetic susceptibility (χ'') versus frequency of **2.1** (left) and **2.2** (right) under zero-field conditions between 1.8 and 22 K. Solid points are experimental data and lines are best-fits to the generalised Debye model (described in-text).

To offer further insight into the relaxation mechanisms occurring under zero-field, the relaxation rates were plotted as a function of T on a log-log scale (**Figure 2.5, a, d**) and fit with the parameter-sparse equation **2.1**, Where the first component represents a Raman process with terms C and n; and the second component represents a quantum tunnelling process, with the rate term, τ_{QTM}^{-1}. Uncertainty values and error bars for the relaxation times were calculated based on the method described by Chilton and Reta, utilising a log-normal distribution of the best-fit alpha values at each temperature.[30]

$$\tau^{-1}(T) = CT^{n} + \tau_{QTM}^{-1} \qquad \textbf{2.1}$$

Fitting these data, the magnetic relaxation can be modelled with best-fit parameters of C = 5.81×10^{-2} $s^{-1}K^{-n}$, n = 3.74, and τ_{QTM} = 2.04×10^{-3} s for compound **2.1** and C = 4.58×10^{-2} $s^{-1}K^{-n}$, n = 3.95 and τ_{QTM} = 1.80×10^{-3} s for **2.2**. Attempts to include terms describing Orbach or Direct processes did not meaningfully improve the fit, indicating that the spin relaxation in **2.1** and **2.2** is dominated by QTM and Raman processes. For Kramers' systems (those with an odd number of unpaired electrons, such as Dy^{III}), the Raman exponent is expected to be n = 9. However lower values have been rationalised by the inclusion of optical phonons[6,12,31,32] or phonon bottleneck effects.[33–35]

To better probe the Raman relaxation process occurring, characteristic frequency measurements were carried out on **2.1** and **2.2** to find an optimal field which would minimise QTM and allow Raman relaxation to be isolated. The out-of-phase magnetic susceptibilities for both compounds at 10 K show frequency dependant peaks between 0 and 0.16 T. The field dependence of the relaxation rates (**Figure 2.5**) can be fit to equation 2, which contains terms describing direct and QTM processes:

$$\tau^{-1}(H) = AH^{4}T^{-1} + B_1/(1+B_2H^{2}) \qquad \textbf{2.2}$$

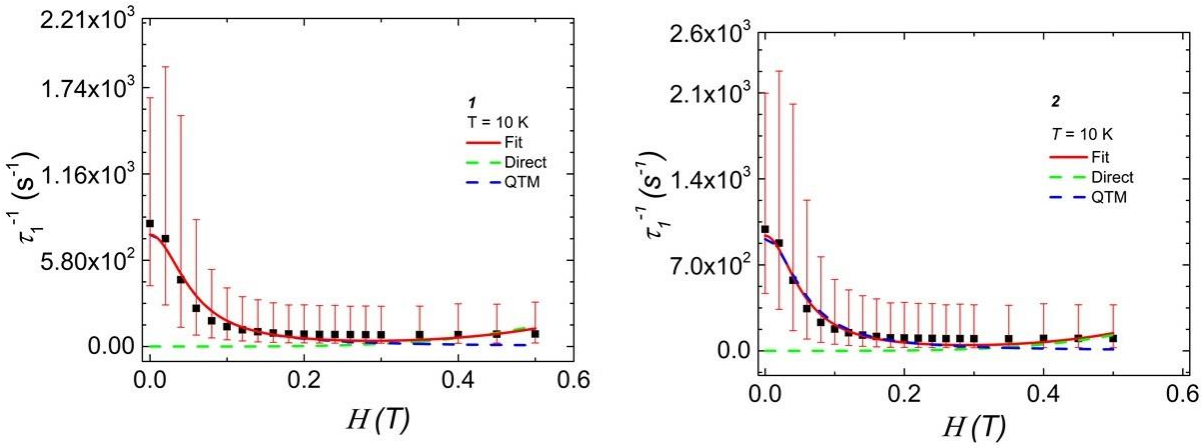

Figure 2.5 - Field dependence of spin relaxation rate of **2.1** (left) and **2.2** (right) at 10 K from 0 to 0.5 T.

Fitting these data, we see that the direct process, a single phonon through-barrier mechanism, is not operative at low fields, but, with a moderate A parameter of 180 T^{-4} K^{-1} s^{-1} in **2.1** and 213 T^{-4} K^{-1} s^{-1} in **2.2**, begins to contribute to the relaxation of the magnetisation above 0.4 T. The QTM terms B_1 and B_2, which describe the off-diagonal crystal field terms, and thus the QTM rate, are relatively large with best-fit paramaters of B_1 = 751 s^{-1} B_2 = 331 T^{-2} in **2.1**, and B_1 = 939 s^{-1}, B_2 = 339 T^{-2} in **2.2**. These may be explained by the low symmetry environment, which can lead to admixture of electronic m_j states and facilitate QTM.[36,37] Additionally, molecular flexibility has recently been suggested as an important contributor to through barrier relaxation pathways in SMMs and qubits.[38–41] An optimal field of 0.12 T was chosen for further temperature-dependant analysis as this would minimise contributions from direct and QTM pathways.

Further temperature-dependant ac measurements were carried out on **2.1** and **2.**2 between 1.8 and 25 K under an applied optimal field of 0.12 T. Each isothermal dataset was fit using the generalised Debye model and the extracted relaxation rates were plotted against T (**Figure A.7**). Fitting these data to a Raman-only model gives best-fit values of C = 3.68x10-4 s^{-1} K^{-n}, n = 5.35 for **2.1**, and C = 2.86x10^{-4} s^{-1} K^{-n}, n = 5.62 for **2.2**. Attempts to restrain the Raman parameters to those obtained from the zero-field fits, or to include Orbach or direct terms, did not meaningfully improve the fits.

To improve these models, the zero-field and optimal-field τ^{-1} vs. T data were globally fit using equation 1 (**Figure 2.6**). To keep the models physically reasonable, n values were restrained to integer values and QTM was assumed to be negligible under optimal field conditions. Best fits were obtained with the parameters τ_{QTM} = 1.56x10^{-3} s, n = 5, C = 1.13x10^{-3} s^{-1} K^{-n} for **2.1** and τ_{QTM} = 1.47 x10^{-3} s, n = 5, C = 1.90x10^{-3} s^{-1} K^{-n} for **2.2**. These values are best-fits and therefore cannot be correlated strongly with structural parameters or relaxation mechanisms, however the near identical properties suggest that the deuterium enrichment has minimal effects on the magnetic relaxation processes. Even under an optimal field, where the Raman pathway is shown to be dominant, we see only a marginal decrease in the relaxation time from 12.5 ms in **2.1** to 10.2 ms in **2.2**, and an increase in the Raman parameter C from 1.13x$10^{-3}$$s^{-1}$$K^{-n}$ in 1 to 1.90x10^{-3}s-1K^{-n} in 2. This may be due to the relatively small change in mass upon deuteration of BH_4 compared to the mass of the central

dysprosium (III) ion, or that any effects on the dominant spin-relaxation pathways are not noticeable within the experimentally accessible conditions.

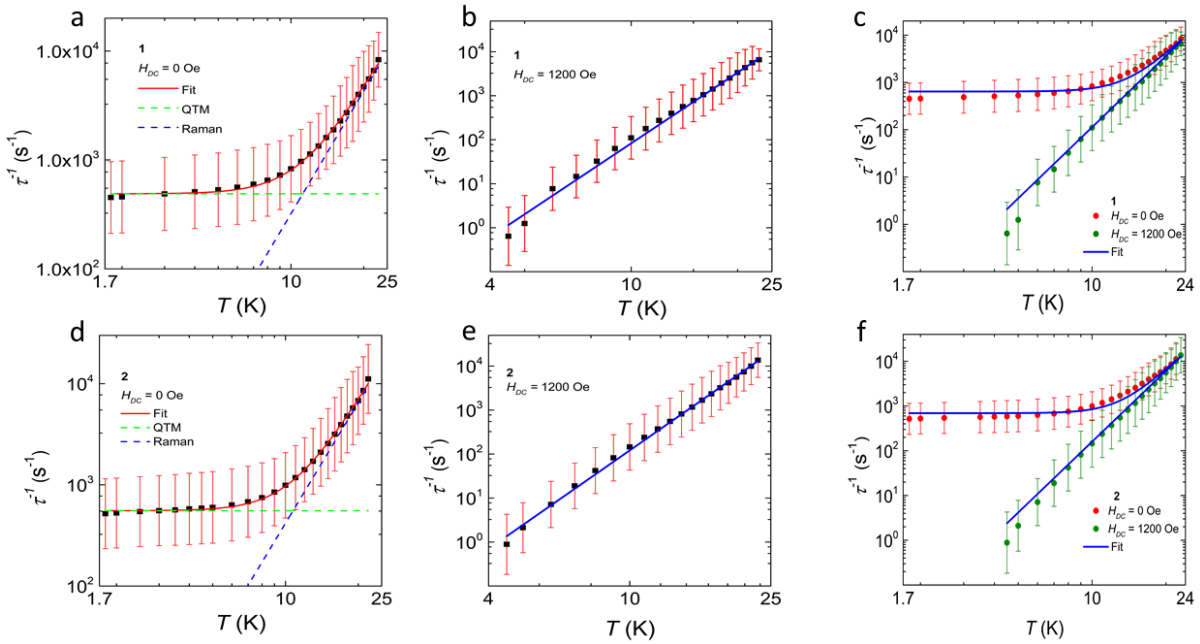

Figure 2.6 - Log-Log plots of the temperature dependence of the relaxation rates for **2.1** and **2.2** extracted from best-fits of the out-of-phase susceptibilities under zero field (**a, d**), optimal field (**b, e**) and global fit of both datasets (**c, f**). Dotted lines represent Raman (blue) and QTM (green) components of overall fit (solid red). Solid blue lines in c and f represent the global fit. Data were fit with equation 1 using parameters discussed in-text. Error bars were calculated using the method escribed by Chilton and Reta in-text.

Table 2.2 - Global fitting parameters as described in text for compounds **2.1** and **2.2**.

Label		**2.1**	**2.2**
QTM	τ (s)	1.56×10^{-3}	1.47×10^{-3}
Raman	C ($s^{-1}K^{-n}$)	1.13×10^{-3}	1.90×10^{-3}
	n	5.0	5.0

2.2.4 Electronic Structure and Bonding:

To gain insight into the mechanism of spin relaxation occurring, *CASSCF* (complete active-space self-consistent field) electronic structure calculations were carried out using DFT (Density Functional Theory) optimised structures of **2.1** and **2.2** (**Table A10**). These calculations shown that the electronic ground state in **2.1** and **2.2** is well separated from the low-lying excited states at 174 cm^{-1}, and predict a strongly anisotropic ground state, as revealed by the CF *g* tensors (g_x,g_y < 0.01). The first excited state shows a deviation from axiality in *g*-tensor calculations: g_y = 0.6, g_x = **2.6**, g_z = 16.7 in **2.1**, g_y = 0.6, g_x = 2.6, g_z = 16.7 in **2.2**, however as the relaxation appears to occur *via* a through-barrier mechanism, it isn't clear what role the excited states play in facilitating spin-relaxation. However recent

computational work has highlighted the importance of the energy gap between the electronic ground and first excited states for the slow magnetic relaxation of SMMs.

Lanthanide-ligand bonding is classically considered to be electrostatic-only (*vide supra)*, however, while calculating the energies and CF parameters of the dysprosium (III) complex **2.1,** it was discovered that inclusion of covalent interactions has a large effect on the resulting electronic manifold. We can illustrate this by looking at the orientation of the g_z tensor of the ground state KDs (**Figure 2.7**). We observe an angle of 70^o between the two calculated magnetic axes – showing that orbital overlap has a non-negligible effect on the electronic properties of **2.1**. Additionally, we see a significant difference in the CF *g* tensors of the excited KDs, with loss of magnetic axiality expected when only considering electrostatic interactions (gx = 10.04, gy = 9.70, gz = 1.36) but strong anisotropy expected when orbital overlap was considered (gx = 0.09, gy = 0.10, gz = 17.10) at the same level of theory. We can observe a similar difference when looking at the calculated energies of the first excited state KDs (**Table S10**), which differ by 90 cm^{-1} when comparing the electrostatic-only to the electrostatic and covalent models using the same basis set, with 74^{-1} cm for the former and 164 cm^{-1} for the latter respectively. It is clear therefore that the bonding in **2.1** cannot be described accurately using the classical description of Lanthanide metal bonding, *i.e.*, orbital overlap is playing a non-negligible role in the metal-ligand bonding interactions.

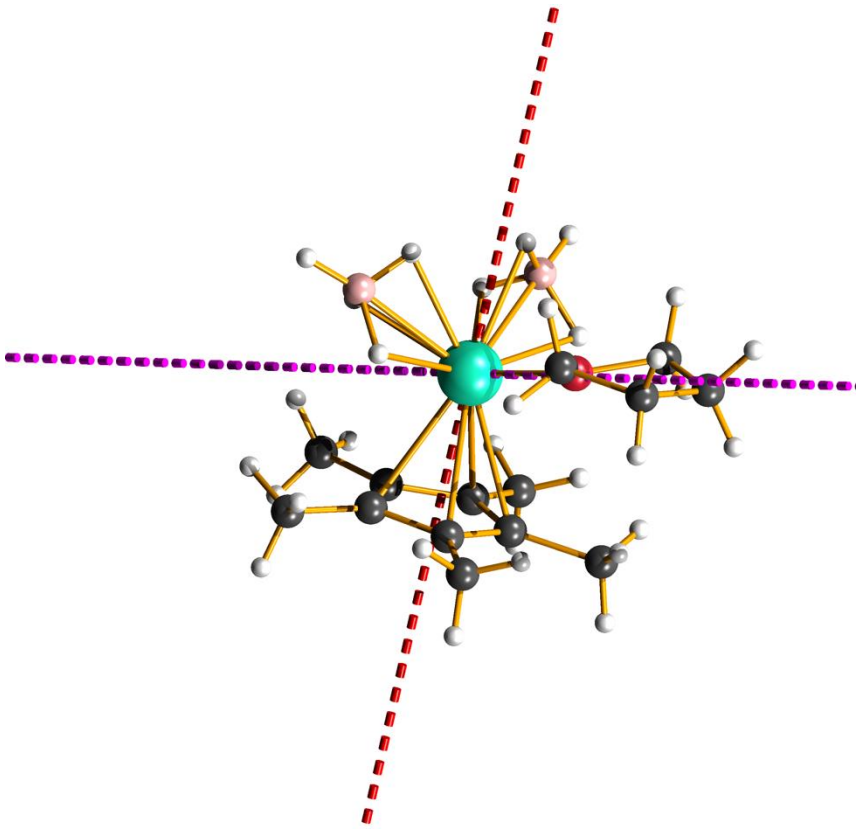

Figure 2.7 - Magnetic Axes of the ground state KDs as described by the g_z tensors calculated accounting for just electrostatic interactions (violet line) or electrostatic interactions and covalent interactions (red line). Calculated using CASSCF methods.

To support these models experimentally, low-temperature fluorescence emission spectroscopy was carried out on a crystalline sample of **2.1** to evaluate its electronic structure. Upon lowering the temperature to 14 K, we expect the CF excited states to be depopulated following a Boltzmann distribution, allowing the CF microstates to be identified (**Figure 2.8 B**). The experimentally derived first KD lies 181 cm^{-1} above the ground state, which is in agreement with the covalent and electrostatic computational model described. By measuring the emission at progressively higher temperatures, we can identity transitions occurring from electronic excited states, known as "hot bands" (**Figure 2.8 A**).

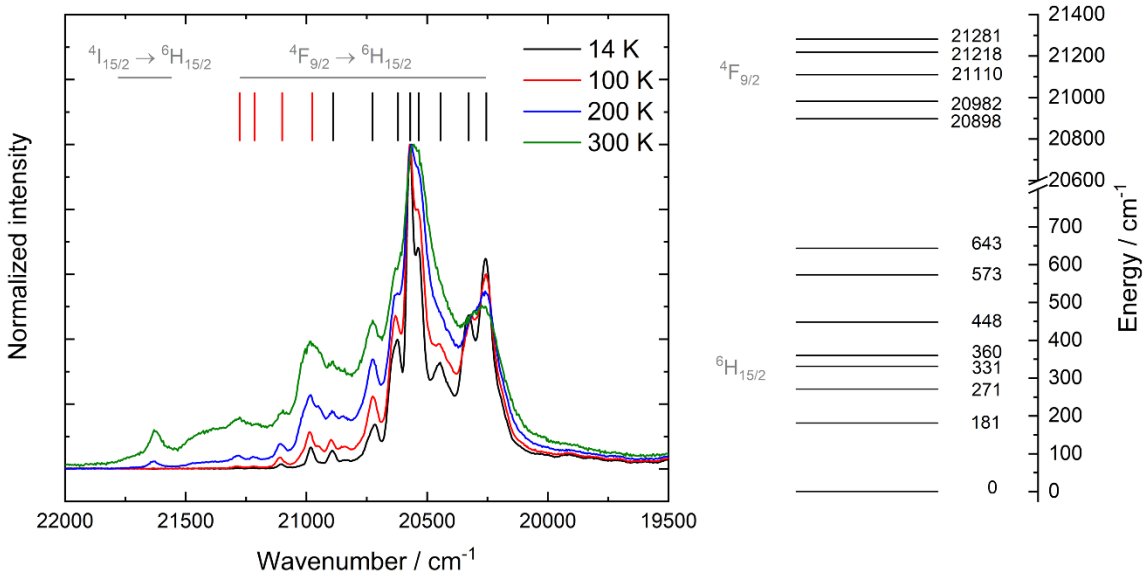

Figure 2.8 - Low-temperature emission fluorimetry carried out on a crystalline sample of **2.1**, prepared in an air-tight cuvette under a nitrogen atmosphere. Plot colour corresponds to measurement temperature indicated in legend. Black bars above spectra correspond to "cold band" peaks, red bars correspond to "hot band" peaks (**A**). Experimentally derived energies of the CF microstates of **2.1** and their corresponding Russell Saunders levels (**B**).

We can generate *ab initio* blocking barriers by examining the magnetic moments for each possible spin transition pathway (**Figure 2.9**) in the CF matrix. The dark red transitions occur with higher probability than pink transitions, giving an insight into the possible spin-relaxation pathways within the system. For a purely axial system, we would expect to see no through-barrier processes as $g_x = g_y = 0$. However, we can see that the excited KDs deviate from axiality, and give rise to through-barrier relaxation, in the form of QTM (horizontal lines), or spin-phonon coupling transitions (diagonal lines). Noticeably, we see significant QTM taking place in the first KDs, due to the transverse CF terms. This is in agreement with the significant QTM observed experimentally. We do not observe a qualitative difference between spin transition pathways **2.1** and **2.2**, which is in agreement with the identical magnetic relaxation behaviour determined experimentally.

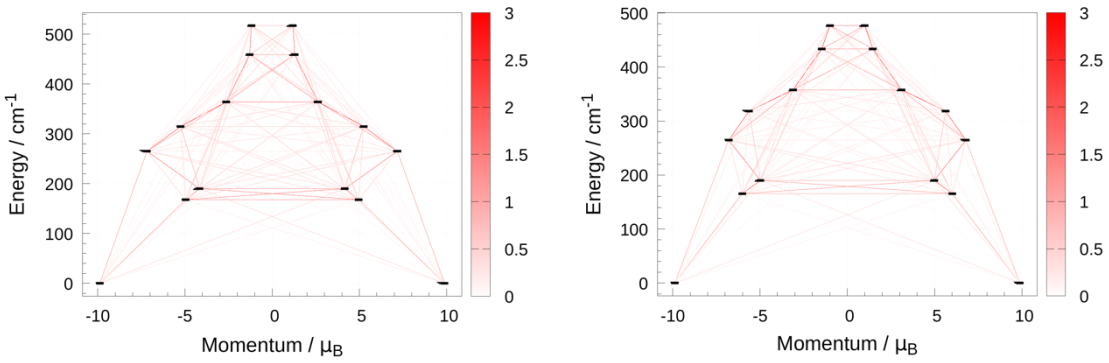

Figure 2.9 - *ab initio* blocking barriers for **2.1** (left) and **2.2** (right) computed with VQZP basis set using DFT optimised structures.

2.2.5 Phonon dispersion:

To investigate the effect of deuteration on the lattice vibrations and possible spin-phonon interactions, VASP (Vienna *ab initio* Simulation Package) phonon spectra were calculated using the DFT optimised crystal structures of **2.1** and **2.2** (**Table A9**, **Figure 2.10**). Complex **2.1** shows a slightly higher density of phonon modes below 200 cm^{-1}; this region has recently been highlighted for its effect on spin-lattice relaxation rates.[40,42] However, the most noticeable difference is the band structure between 1500-2000 cm^{-1} seen only in **2.2**, which is due to B-D stretches with lower frequency than their B-H counterparts in **2.1**. Similar assignments for actinide borodeuteride complexes corroborate this.[43]

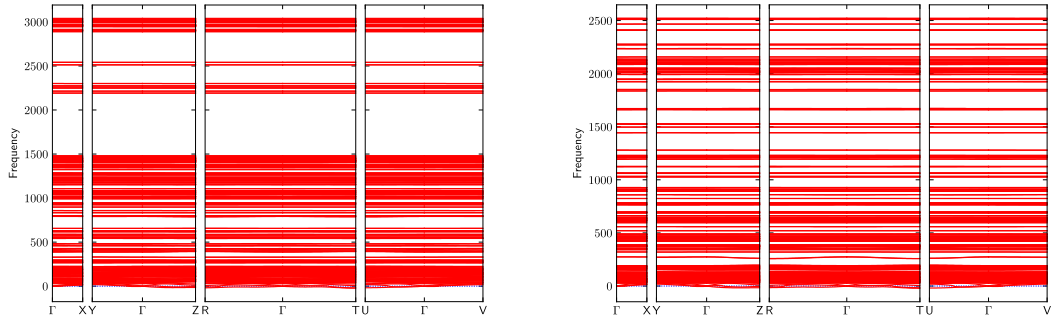

Figure 2.10 - Phonon dispersion in **2.1** (left) and **2.2** (right) computed with VQZP basis set

2.3 Summary:

Herein we report the preparation of the dysprosium pianostool complex [DyCp*(κ^3-BH_4)$_2$(THF)] **2.1**, and its borodeuteride congener [[DyCp*(κ^3-BD_4)$_2$(THF)] **2.2**. The structure of these compounds was described using SC-XRD analysis, and their magnetism dynamics probed *via* SQUID magnetometry. The compounds demonstrate slow magnetic relaxation in the absence of an applied field; however they do not show thermal barriers to magnetic relaxation as in conventional SMMs. Instead, they relax *via* through-barrier processes, namely Raman and QTM processes. The Raman process is mediated by spin-phonon coupling, an interaction that describes dynamic modulation of an ion's crystal field by lattice vibrations, allowing energy to be exchanged between the spin state and the thermal bath. We compared the magnetism dynamics of **2.**1 and **2.2** and demonstrated minor differences in the

spin relaxation. Instead, we observe that the large energy gap is responsible for the presence of slow magnetic relaxation in **2.1** and **2.2**. These results were corroborated by *ab initio* methods, which show that covalent interactions play a significant role in the bonding **2.1.** This result is fascinating in the context of Lanthanide bonding, and may open the door to more complex investigations, such as electronic modification *via* substitution of the Cp* moiety.

2.4 Experimental:

Materials and methods: All reactions and subsequent manipulations were performed under air-free and anhydrous conditions using standard Schlenk-line or nitrogen atmosphere glovebox techniques. Tetrahydrofuran, Toluene, and Hexanes were dried on columns of activated alumina using a J.C. Mayer solvent purification system, degassed with successive freeze-pump-thaw cycles, and stored over 4 Å molecular sieves in a nitrogen atmosphere glovebox prior to use. Celite® used for filtration was dried under vacuum while heating at 200 °C for 120 h, subsequently cooled under vacuum, and stored under nitrogen before use. HCp* was purchased from Sigma Aldrich, thoroughly degassed by successive freeze pump thaw cycles, and stored under nitrogen over 4 Å sieves before use. Hexamethyldisilylamide (HMDS) was purchased from x and used without further purification. Anhydrous $DyCl_3$ and YCl_3 were purchased from Strem Chemicals Inc at 99% purity and stored under nitrogen prior to use. Sodium borohydride was purchased from Sigma Aldrich, dried *in vacuo*, and stored under nitrogen prior to use. Potassium hydride in a mineral oil suspension was purchased from Sigma Aldrich and was washed thoroughly with Hexanes and dried before use.

Infrared spectra were recorded on a Nicolet Nexus 550 FTIR spectrometer using transmission mode in the 4000-600 cm^{-1} range; solid samples were prepared under an inert atmosphere and sandwiched between transparent NaCl plates. NMR spectra were acquired on a Bruker Avance-II 300 MHz spectrometer at 298 K. Elemental analysis were conducted by Midwest Microlab, Indianapolis.

Single-Crystal Xray measurements: Single crystals of **2.1** and **2.2**, suitable for single-crystal X-ray diffraction (SCXRD) analysis were covered in paraffin oil and mounted on a thin glass fiber. Full data was collected on a Bruker AXS SMART APEX-II CCD single-crystal diffractometer (graphite monochromated Mo-Kα radiation, λ = 0.71073 Å), at 200 K temperature. Absorption corrections were applied by using multi-scan of the SADABS[1] program. Structures were solved using direct methods with SHELXT[2] and refined by the full-matrix least-squares methods on F^2 with SHELXL-2018/3[3] in anisotropic approximation for all non-hydrogen atoms. Carbon-bound hydrogen atoms were included in calculated positions. Complex **1** refined as a two component inversion twin in a 46:54 domain ratio. The hydrogen atoms of the borohydride groups in complex **2.1** and complex **2.2** were located and refined isotropically. All geometric/crystallographic calculations were carried out using WINGX[4] and PLATON[5] packages while the molecular graphics were prepared with DIAMOND[6] and MERCURY.[7]

Magnetic Measurements: The magnetic susceptibility measurements were obtained using a Quantum Design SQUID magnetometer MPMS-XL7 operating between 1.8 and 300 K. DC measurements were performed on a polycrystalline sample of 15.0 mg of complex **2.1** and 13.5 mg of complex 2.**2**. The samples were restrained with silicon grease and wrapped in a polyethylene membrane under an inert atmosphere. The samples were subjected to DC fields of -7 to 7 T, and a 3.78 Oe driving field was used for AC measurements. The magnetization data were collected at 100 K to check for ferromagnetic impurities. Diamagnetic corrections were applied for the sample holder and the inherent diamagnetism of the sample with the use of Pascals constants.

$[Dy(BH_4)_3(THF)_3]$

$[Dy(BH_4)_3(THF)_3]$ was prepared by a modified literature procedure. [44]

A high-pressure Schlenk flask was charged with 3.48 g (13.0 mM) of $DyCl_3$, 1.69 g (43.0 mM, 3.5 eq.) of $NaBH_4$, and a stir-bar inside a nitrogen-atmosphere glovebox. The flask was transferred to a Schlenk line, cooled to -78ºC, and 30 mL of THF were added via cannula. The slurry was allowed to heat to RT with stirring under argon, then the flask was placed under static vacuum and heated to 60 ºc for 48 hours. After cooling to room temperature, the off-white suspension was dried *in-vacuo* and taken into a nitrogen-atmosphere glovebox. The grey solids were suspended in 30 mL of THF, filtered through a plug of Celite®, and the solids washed with a further 3 x 10 mL of THF. The translucent yellow solution was reduced in volume by half and cooled to -27ºC overnight. The solution was decanted, and the crystals washed with 3 x 2 mL of cold THF, and dried *in vacuo* to yield 3 g (6.79 mM, 52 %) of $[Dy(BH_4)(THF)_3]$ as pale off-white solids. The mother liquor was further concentrated and placed in the freezer to yield a second crop of crystals. A small portion of these crystals were dissolved in hot THF, allowed to cool to room temperature, and cooled to -27 ºC overnight to yield colourless X-ray quality crystals.

$[DyCp^*(BH_4)_2(THF)]$ – 2.1

A 20 mL scintillation vial was charged with 200 mg (0.45 mM) $[Dy(BH_4)_3(THF)_3]$, a magnetic stirrer bar, and 3 mL THF. A second vial was charged with 66 mg (0.4 mM, 0.9 eq.) KCp*, a magnetic stirrer bar, and 2 mL THF, and the two vials were cooled to -30 ºC. Once cool, the solution of KCp* was added dropwise to the stirred solution of $[Dy(BH_4)_3(THF)_3]$. The opaque solution immediately took on a pale-yellow colour with a white suspension. Once addition was complete, the suspension was allowed to heat to room temperature and was stirred at room temperature overnight. After 18 hours the suspension was filtered through a pad of Celite®, which was washed with an addition 3 x 2 mL THF, and the opaque yellow filtrate was dried *in vacuo* to yield a pale-yellow oil. The oil was washed 3 x 2 mL with hexanes, dried *in vacuo*, extracted into toluene, and filtered through a Celite® pad to yield a pale-yellow solution. The solution was concentrated to half volume and cooled to -27 ºC overnight to yield a crop of pale-yellow block crystals (0.137 g, 0.343 mM, 75%). Found: IR: 2450 w, 2230 s, 2150 s cm^{-1}. A small portion of these crystals were dissolved in hot Toluene, allowed to cool to room temperature, and cooled to -27 ºc overnight to yield X-ray quality crystals.

$[Dy(BD_4)_3(THF)_3]$

$[Dy(BD_4)_3(THF)_3]$ was prepared analogously to the proteo salt, replacing $NaBH_4$ with an equimolar quantity of $NaBD_4$. Briefly: A slurry of 0.8 g (3.0 mM) $DyCl_3$ and 0.5 g (12 mM) of $NaBD_4$ in 20 mL THF was stirred rapidly at 60 ºC under a nitrogen atmosphere for 48 hours. Once cooled, the suspension was filtered through Celite®, and the solids washed with a further 3 x 10 mL THF. The pale-yellow filtrate was reduced to half volume and cooled to -27 ºC overnight to yield 0.6 g (44 %) of off-white crystals. Further concentration of the mother liquor yielded 0.4 g (68 % total) of crystalline material.

$[DyCp^*(BD_4)_2(THF)]$– 2.2

$[DyCp^*(BD_4)_2(THF)]$ was prepared analogously to **1**, replacing $[Dy(BH_4)_3(THF)_3]$ with an equimolar quantity of $[Dy(BD_4)_3(THF)_3]$ to yield **2** in 78 % yield. Briefly: a 20 mL scintillation vial was charged with 0.2 g (0.44 mM) $[Dy(BD_4)_3(THF)_3]$, a magnetic stir bar,

and 2 mL THF, and cooled to -27 ^{o}C. A cold solution of 72 mg (0.4 mM) KCp* in 2 mL THF was added dropwise with stirring, immediately forming a pale white precipitate. The pale-yellow suspension was allowed to heat to room temperature and was stirred at room temperature for 18 hours. Once complete, the suspension was filtered through a pad of Celite®, and the solids washed with a further 3 x 2 mL THF. The combined filtrates were dried *in vacuo* to yield a pale-yellow oil. The oil was washed 3 x 2 mL hexanes before being taken up in 3 mL toluene and filtered through Celite® to yield a pale-yellow solution. Slow diffusion of hexanes into this solution over two days at -27 ^{o}C yielded 140 mg of [DyCp*$(BD_4)_2$(THF)] as pale yellow block crystals.

2.5 References:

1 K. W. H. Stevens, *Rep. Prog. Phys.*, 1967, **30**, 189–225.

2 R. Orbach and P. R. S. L. A, *Proc. R. Soc. London. Ser. A. Math. Phys. Sci.*, 1961, **264**, 458–484.

3 D. H. Moseley, S. E. Stavretis, K. Thirunavukkuarasu, M. Ozerov, Y. Cheng, L. L. Daemen, J. Ludwig, Z. Lu, D. Smirnov, C. M. Brown, A. Pandey, A. J. Ramirez-Cuesta, A. C. Lamb, M. Atanasov, E. Bill, F. Neese and Z. L. Xue, *Nat. Commun.*, 2018, **9**, 1–11.

4 A. Lunghi and S. Sanvito, *Sci. Adv.*, 2019, **5**, 1–8.

5 A. Albino, S. Benci, L. Tesi, M. Atzori, R. Torre, S. Sanvito, R. Sessoli and A. Lunghi, *Inorg. Chem.*, 2019, **58**, 10260–10268.

6 S. E. Stavretis, D. H. Moseley, F. Fei, H. H. Cui, Y. Cheng, A. A. Podlesnyak, X. Wang, L. L. Daemen, C. M. Hoffmann, M. Ozerov, Z. Lu, K. Thirunavukkuarasu, D. Smirnov, T. Chang, Y. S. Chen, A. J. Ramirez-Cuesta, X. T. Chen and Z. L. Xue, *Chem. Eur. J.*, 2019, **25**, 15846–15857.

7 K. Irländer and J. Schnack, *Phys. Rev. B*, 2020, **102**, 1–6.

8 E. Garlatti, L. Tesi, A. Lunghi, M. Atzori, D. J. Voneshen, P. Santini, S. Sanvito, T. Guidi, R. Sessoli and S. Carretta, *Nat. Commun.*, 2020, **11**, 1–10.

9 F. Santanni, A. Albino, M. Atzori, D. Ranieri, E. Salvadori, M. Chiesa, A. Lunghi, A. Bencini, L. Sorace, F. Totti and R. Sessoli, *Inorg. Chem.*, 2021, 60, 1, 140-151.

10 M. Atzori, S. Benci, E. Morra, L. Tesi, M. Chiesa, R. Torre, L. Sorace and R. Sessoli, *Inorg. Chem.*, 2018, **57**, 731–740.

11 A. Lunghi and S. Sanvito, *J. Phys. Chem. Lett.*, 2020, **11**, 6273–6278.

12 M. Briganti, F. Santanni, L. Tesi, F. Totti, R. Sessoli and A. Lunghi, *J. Am. Chem. Soc.*, , DOI:10.1021/jacs.1c05068.

13 M. J. Giansiracusa, A. K. Kostopoulos, D. Collison, R. E. P. Winpenny and N. F. Chilton, *Chem. Commun.*, 2019, **55**, 7025–7028.

14 F. Guégan, J. Jung, B. Le Guennic, F. Riobé, O. Maury, B. Gillon, J. F. Jacquot, Y. Guyot, C. Morell and D. Luneau, *Inorg. Chem. Front.*, 2019, **6**, 3152–3157.

15 L. Escalera-Moreno, N. Suaud, A. Gaita-Ariño and E. Coronado, *J. Phys. Chem. Lett.*, 2017, **8**, 1695–1700.

16 G. Handzlik, M. Magott, M. Arczyński, A. M. Sheveleva, F. Tuna, S. Baran and D. Pinkowicz, *Dalton Trans.*, 2020, **49**, 11942–11949.

17 A. Castro-Alvarez, Y. Gil, L. Llanos and D. Aravena, *Inorg. Chem. Front.*, , DOI:10.1039/d0qi00487a.

18 M. Ephritikhine, *Chem. Rev.*, 1997, **97**, 2193–2242.

19 M. Visseaux and F. Bonnet, *Coord. Chem. Rev.*, 2011, **255**, 374–420.

20 C. A. P. Goodwin, D. Reta, F. Ortu, J. Liu, N. F. Chilton and D. P. Mills, *Chem. Commun.*, 2018, **54**, 9182–9185.

21 F. Guégan, F. Riobé, O. Maury, J. Jung, B. Le Guennic, C. Morell and D. Luneau, *Inorg. Chem. Front.*, 2018, **5**, 1346–1353.

22 D. I. Alexandropoulos, K. R. Vignesh, H. Xie and K. R. Dunbar, *Dalton Trans.*, 2019, **48**, 10610–10618.

23 F. S. Guo, B. M. Day, Y. C. Chen, M. L. Tong, A. Mansikkamäki and R. A. Layfield, *Science*, 2018, **362**, 1400–1403.

24 J. P. Durrant, J. Tang, A. Mansikkamäki and R. A. Layfield, *Chem. Commun.*, 2020, **56**, 4708–4711.

25 J. D. Rinehart and J. R. Long, *Chem. Sci.*, 2011, **2**, 2078–2085.

26 S. Demir, M. D. Boshart, J. F. Corbey, D. H. Woen, M. I. Gonzalez, J. W. Ziller, K. R. Meihaus, J. R. Long and W. J. Evans, *Inorg. Chem.*, 2017, **56**, 15049–15056.

27 B. M. Day, F. S. Guo and R. A. Layfield, *Acc. Chem. Res.*, 2018, **51**, 1880–1889.

28 T. J. Marks and J. R. Kolb, *Chem. Rev.*, 1977, **77**, 263–293.

29 F. Ortu, D. Packer, J. Liu, M. Burton, A. Formanuik and D. P. Mills, *J. Organomet. Chem.*, 2018, **857**, 45–51.

30 D. Reta and N. F. Chilton, *Phys. Chem. Chem. Phys.*, 2019, **21**, 23567–23575.

31 A. Singh and K. N. Shrivasta, *Phys. Stat. Sol.*, 1979, **95**, 273–277.

32 K. Randall McClain, C. A. Gould, K. Chakarawet, S. J. Teat, T. J. Groshens, J. R. Long and B. G. Harvey, *Chem. Sci.*, 2018, **9**, 8492–8503.

33 S. Q. Wu, Y. Miyazaki, M. Nakano, S. Q. Su, Z. S. Yao, H. Z. Kou and O. Sato, *Chem. Eur. J.*, 2017, **23**, 10028–10033.

34 E. Rousset, M. Piccardo, M. E. Boulon, R. W. Gable, A. Soncini, L. Sorace and C. Boskovic, *Chem. Eur. J.*, 2018, **24**, 14768–14785.

35 L. Tesi, A. Lunghi, M. Atzori, E. Lucaccini, L. Sorace, F. Totti and R. Sessoli, *Dalton Trans.*, 2016, **45**, 16635–16643.

36 L. Ungur and L. F. Chibotaru, *Chem. Eur. J.*, 2017, **23**, 3708–3718.

37 J. L. Liu, Y. C. Chen and M. L. Tong, *Chem. Soc. Rev.*, 2018, **47**, 2431–2453.

38 F. Ortu, D. Reta, Y. S. Ding, C. A. P. Goodwin, M. P. Gregson, E. J. L. McInnes, R. E. P. Winpenny, Y. Z. Zheng, S. T. Liddle, D. P. Mills and N. F. Chilton, *Dalton Trans.*, 2019, **48**, 8541–8545.

39 L. T. A. Ho and L. F. Chibotaru, *Phys. Rev. B*, 2018, **97**, 1–18.

40 A. Lunghi, F. Totti, R. Sessoli and S. Sanvito, *Nat. Commun.*, 2017, **8**, 1–7.

41 R. Mirzoyan and R. G. Hadt, *Phys. Chem. Chem. Phys.*, 2020, **22**, 11249–11265.

42 A. Lunghi, F. Totti, S. Sanvito and R. Sessoli, *Chem. Sci.*, 2017, **8**, 6051–6059.

43 R. H. Banks and N. Edelstein, *J. Chem. Phys.*, 1980, **73**, 3589–3599.

44 S. M. Cendrowski-Guillaume, G. Le Gland, M. Nierlich and M. Ephritikhine, *Organometallics*, 2000, **19**, 5654–5660.

Chapter 3: Palladocene

3.1 Introduction:

Cyclobutadiene is a cyclic-1,3-diene which has long been a curiosity of theoretical and synthetic chemists. Unsubstituted cyclobutadiene (C_4H_4) is extremely unstable and has been shown to undergo rapid Diels-Alder polymerisation under matrix isolation conditions at as low as 35 K. The instability of cyclobutadiene has been the subject of theoretical debate, with disagreement over whether it is mainly due to the ring strain or the 4 πe^- antiaromatic electronic configuration.

One of our aims has been to develop a route to tetraaryl substituted cyclobutadienediide salts, as this would facilitate the development of novel cyclobutadienediide organometallic complexes. Sekiguchi and co-workers at the university of Tsukuba disclosed detailed synthetic procedures and characterisation of a series of silyl-substituted dilithio cyclobutadienediide salts in the early 2000s, with a focus on the aromaticity of the novel 6 πe cyclobutadienediide ring.[1–3] These reports were ground-breaking, but limited in two aspects: firstly, the synthesis is carried out using an extremely air, moisture, and thermally sensitive precursor, [$CoCp(CO)_2$]; secondly, the synthesis utilises lithium sand (amorphous Li^0 nanoparticles), which is extremely pyrophoric and should only be handled inside of an argon glovebox. To address this, we took sight on the palladium tetraaryl cyclobutadiene system, which is bench stable and whose reductive chemistry was unexplored.

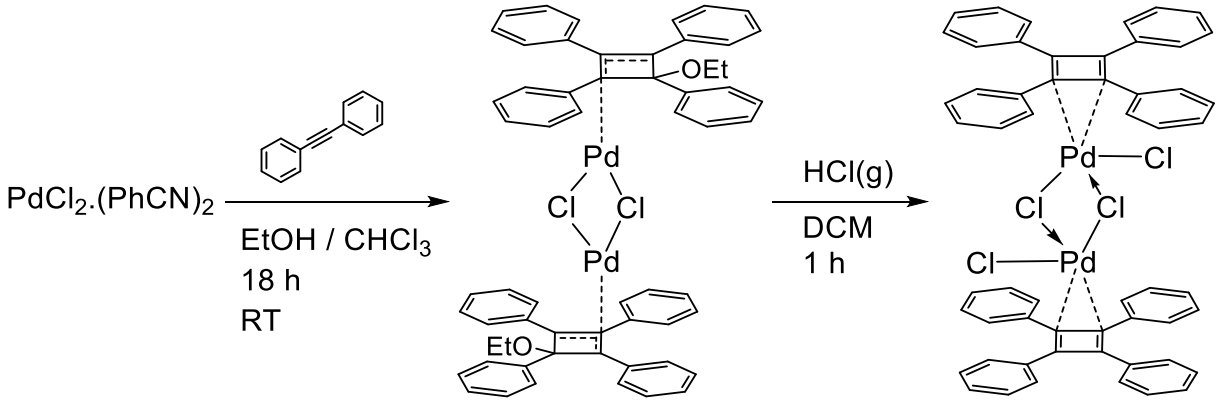

Pd-1 **Pd-2**

Scheme 3.1 - Synthetic scheme describing preparation of **Pd-2**.

The synthesis of palladium cyclobutadiene was first explored by Blomquist and Maitlis. They reported a general procedure to the highly stable $PdCl_2$ Cyclobutadiene dimer, Pd-2 (**Scheme 3.1**) in the early 60s. Briefly: A solution of palladium (II) chloride benzonitrile adduct was heated with an equivalent of diphenylacetylene in a 3:1 ethanol:chloroform mixture. Orange crystals of the palladium cyclobutenyl dimer, **Pd-1**, precipitate from solution overnight in 70-80 % yield. This reaction is notably solvent dependant, with cyclotrimerization to form hexaphenylbenzene occurring in non-coordinating solvents such as benzene. Protonolysis of this complex *via* bubbling dry HCl gas through a DCM solution of **Pd-1** instantly precipitates the chloride bridged cyclobutadiene complex, **Pd-2**. **Pd-2** is

thermally stable up to 330 °C and is stable to strong acids such as H_2SO_4. **Pd-2** is only sparingly soluble in THF and Chloroform saturated with HCl gas.[4,5]

While investigating the palladium (II) cyclobutadiene system we serendipitously discovered the formation of a zerovalent palladium cyclobutadiene sandwich compound (*vide infra*). Contemporary reviews of transition metal cyclobutadiene do not mention any previous syntheses of homoleptic cyclobutadiene sandwich compounds.[5,6,7] However, we uncovered a report of the same compound dating to 1980 which received little attention, likely due to the lack of a solid-state molecular structure.[8]

3.2 Results and Discussion:

3.2.1 Synthesis:

Adding four equivalents of freshly cut potassium metal to an orange solution of **Pd-2** in anhydrous THF under a nitrogen atmosphere causes an immediate precipitation of deep brown solids (**Scheme 3.2**). The dark suspension was stirred vigorously at room temperature overnight and subsequently dried *in vacuo* to yield a tacky brown solid. The solid was then extracted into benzene, filtered through a pad of Celite®, and layered with pentanes to yield black needle crystals of [Pd(η^4-Cb^{Ph4})$_2$], compound **3.1** after standing for one week at room temperature.

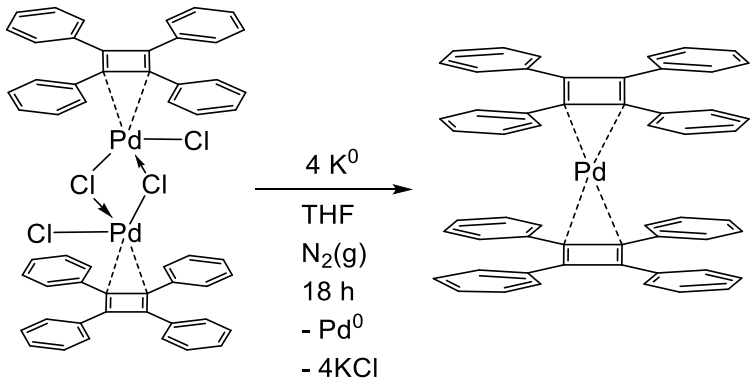

Scheme 3.2 - Synthetic scheme describing preparation of compound **3.1** [Pd(η^4-Cb^{Ph4})$_2$].

The formation of compound **3.1** was unexpected, as no previous cyclobutadiene sandwich complexes were reported in contemporary literature. However, on deeper inspection a report in 1980 was discovered which reports an analogous synthesis of **3.1**, utilising Li_2COT (COT = 1,3,5,7-cyclooctatetraene) as a soluble reducing agent.[8] Their investigation included NMR spectroscopy and mass spectrometry; however no crystal structure was obtained.

3.2.2 Structural Analysis:

X-ray quality black needle crystals were obtained *via* slow diffusion of pentane into a solution of **3.1** over one week and were interrogated using SC-XRD analysis. Compound **3.1 (Figure 3.1)** crystallises in the monoclinic space group, $P2_1$, with lattice parameters a = 10.6694(4) Å, b =16.9322(7) Å, c = 11.1731(4) Å, $\alpha = \gamma = 90^o$, β = 102.345(1)°, V = 1971.8(1) Å^3, and one metallocene complex inside the asymmetric unit. This space group can be understood as each metallocene sits on a crystallographic inversion centre. Each complex comprises a zerovalent palladium centre bound to two {η^4-C_4Ph_4} rings with centroid distances Pd-Cb_{cg} = 1.9140(5) Å and Pd-Cb'$_{cg}$ = 1.9148(5) Å, making an angle of ∠Cb_{cg}-Pd-

Cb'_{cg} = 177.94(3)^{o} with the metal centre. These distances are consistent with the formula [Pd(η^4-Cb^{Ph4})$_2$], describing a neutral zerovalent palladium metallocene with 18 valence electrons. This is worth noting as the analogous neutral [Pd(η^5-Cp*)$_2$] complex hosts 20 valence electrons and is only stable on the CV timescale.

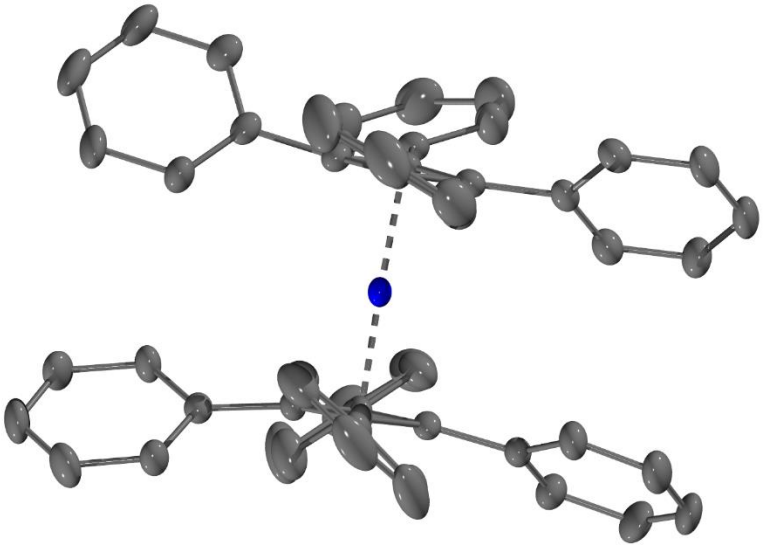

Figure 3.1 - Solid state molecular structure of [Pd(η^4-Cb^{Ph4})$_2$, thermal ellipsoids rendered at the 50 % probability level. Colour code: carbon, grey; palladium, blue. Hydrogen atoms were removed for clarity.

The cyclobutadiene ring in the {C_4Ph_4} fragment shows C-C bond lengths greater than standard C=C double bonds (1.350 Å) and minor bond length alteration, suggesting aromatic delocalisation of their π electrons (**Table 3.1**). We can rationalise this bond length equalisation in the seemingly antiaromatic ring with the Dewar-Chatt-Duncanson model of TM-alkene complexes, which shows that synergistic metal-to-ligand π backbonding, which strengthens the coordination complex, occurs via donation of electrons from a filled metal orbital into an empty ligand π* antibonding orbital (*vide supra*). The bond lengths and angles are in agreement with previously reported transition metal cyclobutadiene complexes, and recent *ab initio* investigations of Cb.[9,10]

Table 3.1 - Selected interatomic distances in [Pd(η^4-Cb^{Ph4})$_2$], **3.1**

Label	Distance (Å)	Label	Distance (Å)	Label	Angle (^{O})
$Pd\text{-}Cb_{cg}$	1.9146(5)	$Pd\text{-}Cb'_{cg}$	1.9142(5)	Cb-Pd-Cb’	177.95(3)
C1-C2	1.470(9)	C1’-C2’	1.492(9)	C1-C2-C4	89.9(5)
C3-C4	1.469(8)	C3’-C4’	1.484(9)	C1-C4-C3	90.3(5)
C1-C4	1.472(8)	C1’-C4’	1.473(9)	C1’-C2’-C4’	89.6(5)
C2-C3	1.480(8)	C2’-C3’	1.478(8)	C1’-C4’-C3’	90.2(5)

The metallocene units pack in a herringbone arrangement (**Figure 3.2),** with the closest intermolecular distance of $Pd\text{-}Pd_{inter}$ = 10.1288(7) Å.

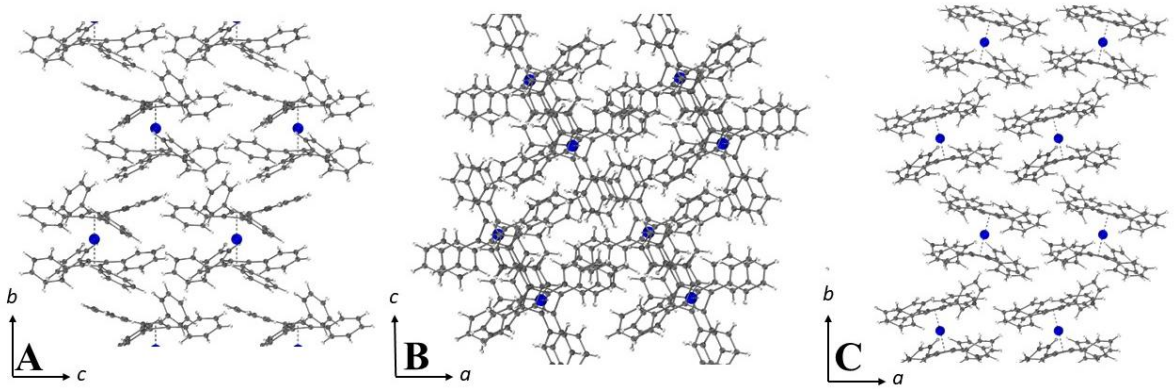

Figure 3.2 - Solid-state molecular packing of [Pd(η^4-Cb^{Ph4})$_2$] **3.1,** viewed down the *a* (**A**), *b* (**B**), and *c* (**C**) crystallographic axes. Atoms were rendered as ball-and-sticks for clarity. Colour code: carbon, grey; palladium, blue; hydrogen, white.

Hirshfeld surface plots are a computational tool developed to visually relate the molecular structure of a crystal to its intermolecular packing. The Hirshfeld surface is a 3D isosurface where each point is defined as where the molecular and supramolecular wavefunctions have equal contributions. This surface further maps a specific property, such as the normalised contact distance, d_{norm} or the shape index, *S* on each point, illuminating the interactions between the molecule and the crystal.[11] Hirshfeld surface plots mapping d_{norm} and the *S* for **3.1** were generated using CrystalExplorer21 and are displayed in **Figures 3.3** and **3.4** respectively**.**[12] Red areas on the d_{norm} surface indicate close-contacts, defined as when the weighted interatomic distance is shorter than the sum of the respective atoms' van der Waal radii. White regions indicate that the interatomic distance is at or around the sum of the van der Waal radii, and blue regions are where the interatomic distance is longer than the sum of the van der Waal radii. Looking at the d_{orrm} surface, we can see several close interactions appear as red circles above the phenyl groups. The top face of the surface is notably deformed as a result of the phenyl groups' free rotation.

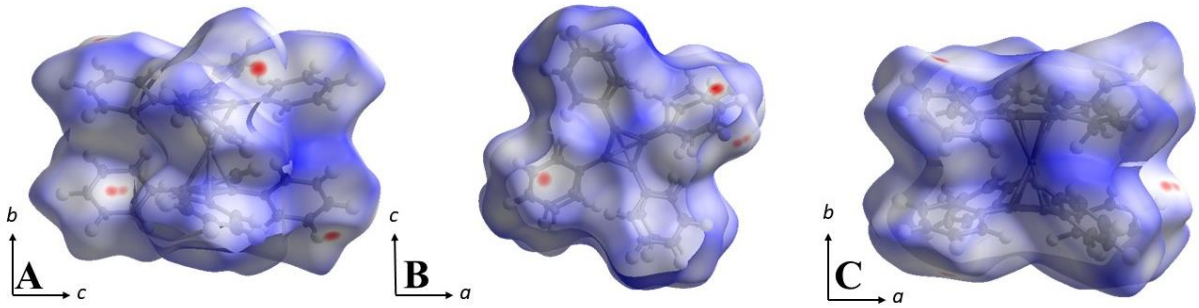

Figure 3.3 - Hirshfeld surface plot of [Pd(η^4-Cb^{Ph4})$_2$] **3.1,** mapping d_{norm} viewed down the *a* (**A**), *b* (**B**), and *c* (**C**) crystallographic axes. Surface code: blue, interatomic distance > sum of vdW radii; white, interatomic distance = sum of vdW radii; red, interatomic distance < vdW radii. Atom colour code: carbon, grey; palladium, blue; hydrogen, white. Generated using CrystalExplorer21.[12]

The shape index is a measure of the magnitude and direction of a surface's curvature, where red areas are concave and blue areas convex deformations of the surface. Red hollows

observed above the phenyl rings and the complementary blue peaks at the tips of the phenyl groups are a result of the significant close contacts within the crystal structure (**Figure 3.4**).

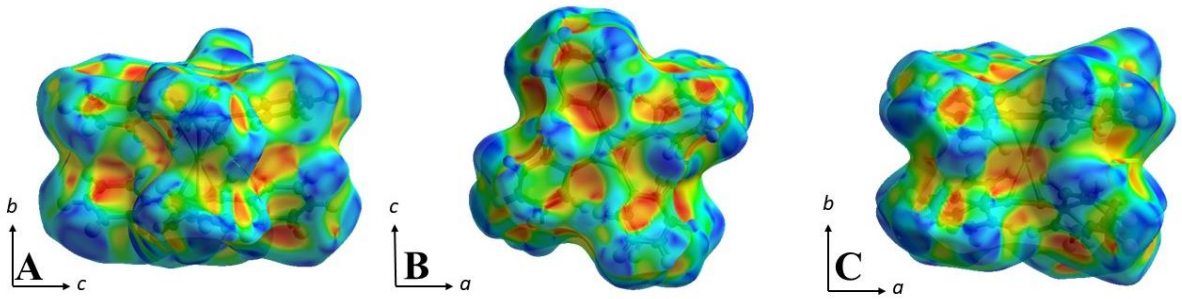

Figure 3.4 - Hirshfeld surface plot of [Pd(η^4-Cb^{Ph4})$_2$] **3.1,** mapping S viewed down the *a* (**A**), *b* (**B**), and *c* (**C**) crystallographic axes. Surface colour code: concave, red; planar. Atom colour code: carbon, grey; palladium, blue; hydrogen, white. Generated using CrystalExplorer21.[12]

We can make a "fingerprint plot" (**Figure 3.5**, **A**) by generatng a 2D histogram of the Hirshfeld surface according to the interatomic distances (d_e and d_i) and interaction frequency from blue (rare) to red (common).[13] The high symmetry and width of the plot indicates frequent short contacts with equal donor and acceptor contributions, likely because of the close packing arrangement in the crystal structure. By breaking down the contributions by donor and acceptor atom identity we can observe that most of the close interatomic contacts are between protons, with H···H interactions dominating between 1.2 – 1.8 Å and C···H interactions taking place between 1.8 – 2.2 Å. C···C interactions make up a smaller portion of the plot between 2.2 – 2.8 Å. Comparing the frequency of interactions as a percentage of total interactions (**Figure 3.5, B**), we can see that H···H interactions dominate, making up over 71% of all total contacts. C···H and H···C interactions are the second most frequent, making up 27.5 % of all interactions on the surface. Finally, C···C type interactions are the least frequent, contributing to only 1.3 % of all interactions. We would expect to see a red centroid around the vdW radius of carbon (1.8 Å) if significant π - π stacking was present, which we do not observe. These data show that the majority of lattice interactions taking place are between hydrogen atoms of the eight phenyl groups. Targeting these interactions, such as by substituting the hydrogen atoms for fluorinated groups (-F, -CF_3), could therefore prove an interesting route to develop new Palladocene derivatives.

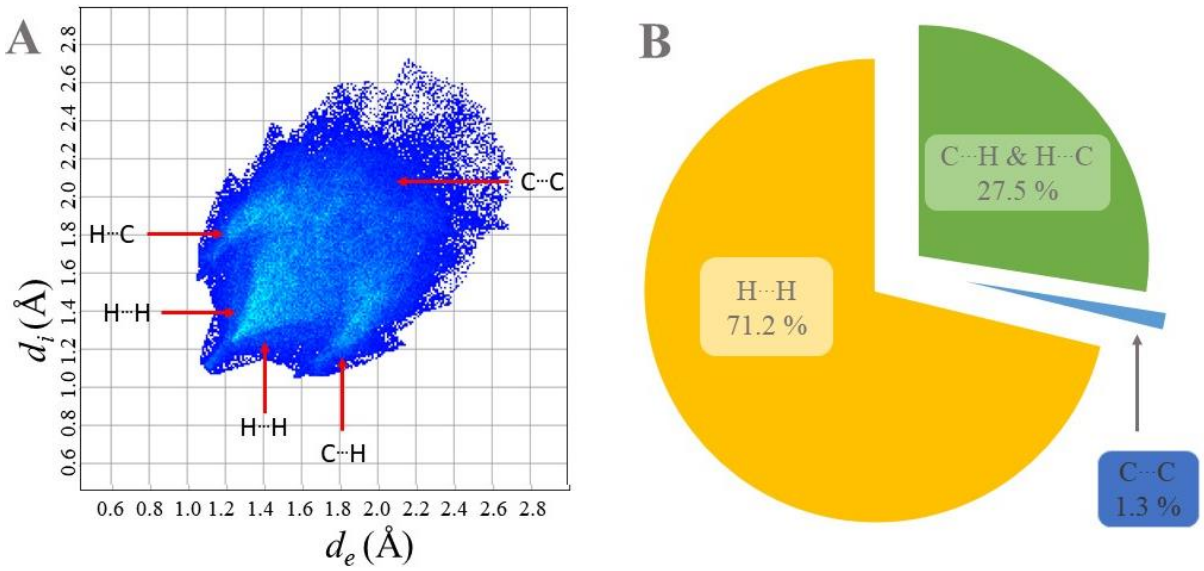

Figure 3.5 - Fingerprint plot of [Pd(η^4-Cb^{Ph4})$_2$] **3.1,** showing the contacts as a function of distance (d_i and d_e) and frequency (**A**). Colour code: blue, least common; green, moderately common. Pie chart showing interaction groups' frequency as a percentage of total interactions (**B**). Generated using CrystalExplorer21.[12]

3.2.3 Molecular Symmetry and Bonding:

As discussed previously, the stability of **3.1** is likely a result of significant metal-to-ligand π-back donation, which is in agreement with the Dewar-Chatt-Duncanson model of bonding in TM-olefin complexes.[14] We can rationalise this by looking at the Symmetry Adapted linear Combinations (SALCs) of ligand group orbitals and metal atomic orbitals which form the possible Molecular Orbitals (**Figure 3.6**). Considering **3.1** to be described by C_{4h} symmetry (not D_{4h} as there are no dihedral rotational axes), the 4d orbitals are separated in three groups (**Figure 3.6, C**): the A_g set, containing the 4dz^2 orbital; the doubly degenerate E_g set, containing the 4dyx and 4dyz orbitals; and the doubly degenerate B_g set, containing the 4d(x^2-y^2) and 4dxy orbitals.[15] In addition to these, we also have the filled 5s orbital, with symmetry A_g, and the empty 4pz orbital with symmetry A_u. The 4px and 4py orbitals do not have the correct symmetry to interact with the ligand group orbitals. The ligand group orbitals (**Figure 3.6, B**) describe the 8 possible combinations of the π-MOs from each Cb ring. The two bonding MOs can combine symmetrically or asymmetrically, described by the A_g and A_u symmetry species respectively. The non-bonding MOs, each with two nodes, combine to form two sets of doubly degenerate group orbitals, described by the E_u and E_g symmetry species. Finally, the highest energy antibonding MOs with three nodes each combine to form two group orbitals with symmetry B_g and B_u. This gives rise to 9 SALCS, exhibiting three different types of bonding combinations. The 5s and 4dz^2 atomic orbitals have the correct symmetry for σ-interactions with the A_g group orbital (**Figure 3.6, D**), which represents the π-bonding orbitals of each Cb. The 4dyz and 4dxz orbitals have the correct symmetry for π-back donation into the E_g group orbital (**Figure 3.6, E**), which represents the non-bonding MOs of each Cb. This π-back donation interaction likely contributes to the stabilisation of the Cb moiety, as it can be thought of donating 2 electrons into each 4π antiaromatic system, making them aromatic. Finally, the 4d(x^2-y^2) and 4dxy orbitals have the correct symmetry to engage in a δ-bonding interaction with B_g group orbitals of the Cb rings in a face-to-face-to-face manner (**Figure 3.6, F**). As the B_g group orbitals are composed of the highest energy

antibonding orbitals in free Cb, this interaction may give rise to further metal-to-ligand back bonding. A similar assessment was predicted for a nickel cyclobutadiene complex[16], which has been described as "metalloaromatic" due to the enhanced electronic stability of the Cb rings upon coordination.[17] A comparable δ-bonding interaction was reported in Uranocene, $[U(COT)_2]$, a Uranium (IV) metallocene, *via* 5f atomic orbitals interacting with the antibonding group orbitals of the aromatic COT^{2-} dianions.[18] Unlike the Lanthanides, the Actinide 5f valence orbitals are strongly interacting, acting more like TMs.[19,20] Similar bonding has been predicted for an Actinide Cb metallocene, however no such examples have been structurally authenticated.[21]

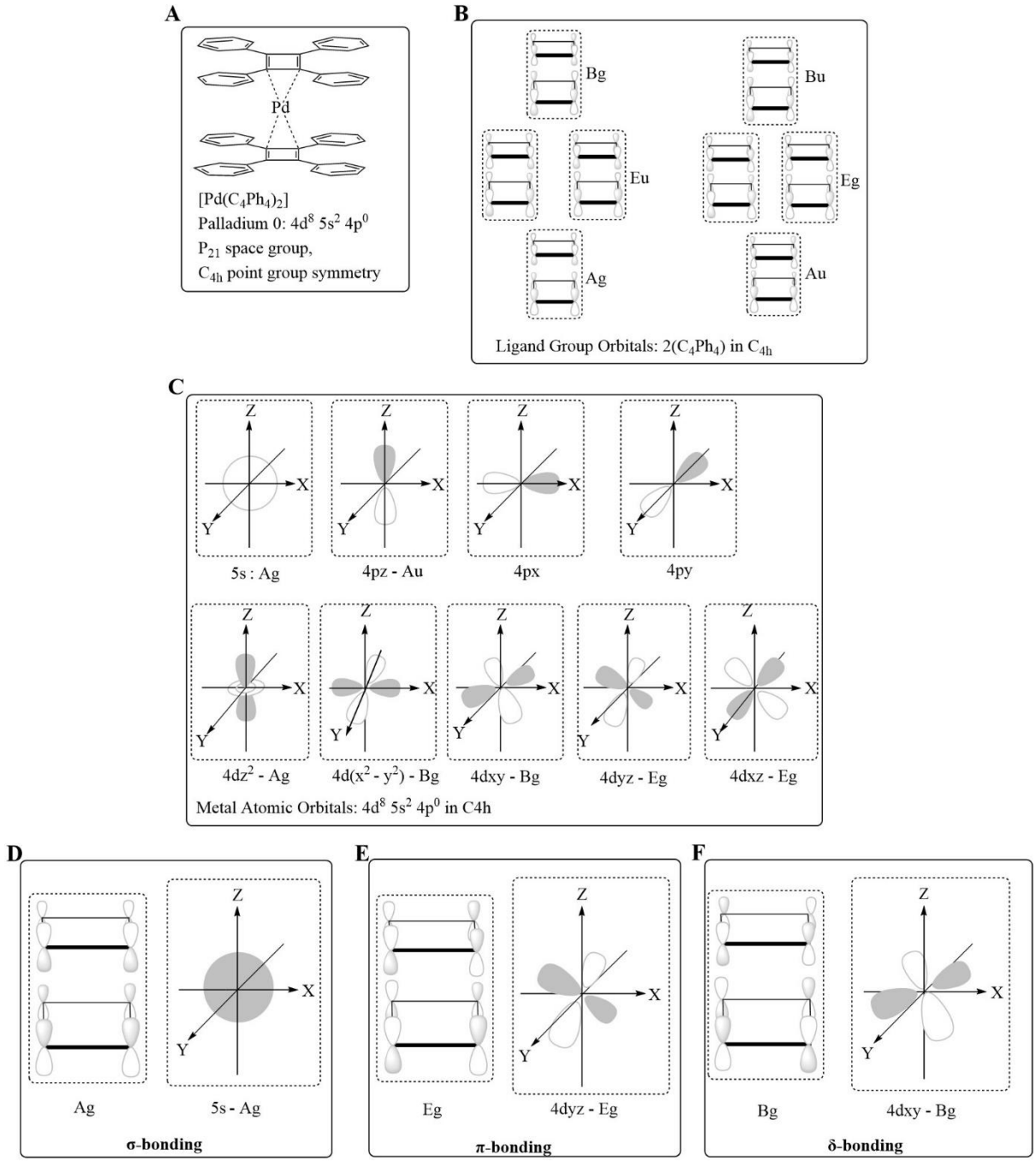

Figure 3.6 - Schematic representation of the solid-state molecular structure of of $[Pd(\eta^4\text{-}Cb^{Ph4})_2]$ **3.1,** its electronic configuration and molecular symmetry (**A**). The eight group

orbitals resulting from the symmetry adapted combination of two Cb^{Ph4} ligands when considered in C_{4h} point group symmetry (**B**). Grey and white lobes represent positive and negative phases of the wavefunction respectively. Each state is derived from the π-molecular orbital diagram for cyclobutadiene (see: Chapter 1). The valence atomic orbitals for palladium (0) in C_{4h} symmetry (**C**). The 4px and 4py orbitals do not have the correct symmetry to engage in bonding interactions but are shown for continuity. An example of a symmetry-allowed σ-bonding interaction in **3.1**, between the filled 5s orbital and the A_g group orbital (**D**). An example of a symmetry-allowed π-bonding interaction in **3.1**, between the empty 4dyz orbital and the E_g group orbital (**E**). An example of symmetry-allowed δ-bonding interaction in **3.1**, between the filled 4dxy orbital and the B_g group orbitals (**F**).

3.3 Summary:

We report the synthesis and characterisation of [Pd(η^4-Cb^{Ph4})$_2$] **3.1**, which is the first monomeric zerovalent palladium metallocene reported and the second structurally authenticated example of a cyclobutadiene metallocene in the literature. Utilising Maitlis and Blomquist's [2+2] cyclisation of phenylacetylene with palladium (II), the chloride bridged dimer **Pd-2** was formed. Chemical reduction of this species yields the formally zerovalent palladium complex, **3.1**, which hosts 18 valence electrons. SC-XRD analysis and group theory were used to give insight into the symmetry and bonding of **3.1**, showing that there are symmetry allowed *σ*-, *π*-, and *δ*- bonding combinations. Hirshfeld surface analyses were used to investigate the packing and intermolecular contacts stabilising the crystal structure. Based on its high thermal stability and predicted electrical conductivity, future work may investigate the of applications of **3.1** *via* experimental conductivity measurements and *ab initio* electron-transport calculations.

3.4 Experimental:
Materials and methods

Caution: elemental alkali metals are extremely pyrophoric and should be handled with care.

All reactions and subsequent manipulations were performed under air-free and anhydrous conditions using standard Schlenk-line or nitrogen atmosphere glovebox techniques. Tetrahydrofuran, toluene, benzene, hexanes, and pentane solvents were dried on columns of activated alumina using a J.C. Mayer solvent purification system, degassed with successive freeze-pump-thaw cycles, and stored over 4 Å molecular sieves in a nitrogen atmosphere glovebox prior to use. Celite® used for filtration was dried under vacuum while heating at 200 °C for 120 h, subsequently cooled under vacuum, and stored under nitrogen before use. 4 Å molecular sieves were activated by heating to 200 °C under high vacuum for a week, slowly cooling to room temperature, and stored in a nitrogen atmosphere glovebox before use. 9

Infrared spectra were recorded on a Nicolet Nexus 550 FTIR spectrometer using transmission mode in the 4000-600 cm^{-1} range; solid samples were prepared under an inert atmosphere and sandwiched between transparent NaCl plates. NMR spectra were acquired on a Bruker Avance-II 300 MHz spectrometer at 298 K. Elemental analysis were conducted by Midwest Microlab, Indianapolis.

Single-Crystal Xray measurements: Single crystals suitable for single-crystal X-ray diffraction (SCXRD) analysis were covered in parabar oil and mounted on a thin glass fiber. Full data was collected on a Bruker AXS SMART APEX-II CCD single-crystal diffractometer (graphite monochromated Mo-Kα radiation, λ = 0.71073 Å), at 200 K temperature. Absorption corrections were applied by using multi-scan of the SADABS[1] program. Structures were solved using direct methods with SHELXT[2] and refined by the full-matrix least-squares methods on F^2 with SHELXL-2018/3[3] in anisotropic approximation for all non-hydrogen atoms. Carbon-bound hydrogen atoms were included in calculated positions.

Synthesis of $[Pd(C_4Ph_4OEt)_2Cl_2]$ – Pd 1

$[Pd(C_4Ph_4OEt)_2Cl_4]$ was prepared using a modified literature route.[4]

A 50 mL round-bottomed flask was charged with 0.8 g of palladium (II) chloride benzonitrile solvate, $[PdCl_2(PhCN)_2]$ (2.1 mM), a magnetic stir bar, and 10 mL chloroform. In a separate flask, 0.75 mg diphenylacetylene (4.2 mM) was dissolved in 10 mL of 99 % ethanol. The turbid solution was added dropwise to the rapidly stirred pale red palladium solution, and once complete, the red solution was stirred at room temperature for 18 hours. Once settled, an orange microcrystalline material was collected on a frit, washed with 3 x 5 mL hexanes, and dried *in vacuo* to 1.6 g (1.47 mM, 74 %) $[Pd(C_4Ph_4OEt)_2Cl_2]$ as an orange microcrystalline powder.

Synthesis of $[Pd(Cb^{Ph4})_2Cl_4]$ – Pd 2

$[Pd(Cb^{Ph4})_2Cl_4]$ was prepared using a modified literature route.[4]

1.0 g (0.92 mM) of Pd-1 was dissolved in 50 mL of chloroform with vigorous stirring. Dry HCl gas, generated through the action of concentrated sulfuric acid on NaCl in a side-arm flask, was bubbled through the solution of Pd-1 while stirring for 15 minutes. The pale orange solution instantly darkened and deep red blocks precipitated immediately. The suspension was stirred overnight, collected on a frit, washed with 3 x 5 mL DCM, and dried *in vacuo* to yield 0.64 g (0.59 mM, 65 %) of [$Pd(Cb^{Ph4})_2Cl_4$] as deep red microcrystalline solids.

Synthesis of [$Pd(\eta^4\text{-}Cb^{Ph4})_2$] – 3.1:

Approximately 37 mg (0.946 mM) of freshly cut potassium metal was added piecewise to a vigorously stirred orange solution containing 200 mg of [$Pd(Cb^{Ph4})_2Cl_4$] (0.187 mM) in 10 mL of THF in a nitrogen atmosphere glovebox at room-temperature. The solution quickly darkened, and a brown precipitate formed. After stirring rapidly at room temperature for 16 hours, the suspension was filtered over Celite® and the brown solution dried *in vacuo*. The resultant brown oil was taken up in 5 mL of benzene, filtered through a plug of Celite®, layered with 10 mL pentane, and left to diffuse for 1 week, yielding 46 mg (0.056 mM, 30 %) of [$Pd(\eta^4\text{-}Cb^{Ph4})_2$] as small black needle crystals.

3.5 References:

1 T. Matsuo and A. Sekiguchi, *Bull. Chem. Soc. Jpn.*, 2004, **77**, 211–226.

2 A. Sekiguchi, T. Matsuo and H. Watanabe, *J. Am. Chem. Soc.*, 2000, 122, 5652–5653.

3 A. Sekiguchi, T. Matsuo and M. Tanaka, *Organometallics*, 2002, **21**, 1072–1076.

4 A. T. Blomquist and P. M. Maitlis, *J. Am. Chem. Soc.*, 1962, **84**, 2329–2334.

5 P. M. Maitlis, *J. Organomet. Chem.*, 1980, **200**, 161–176.

6 C. J. Elsevier and M. R. Eberhard, *Compr. Organomet. Chem. III*, 2007, **8**, 269–314.

7 N. V. Shvydkiy and D. S. Perekalin, *Coord. Chem. Rev.*, 2017, **349**, 156–168.

8 H. Hoberg and C. Frolich, *J. Organomet. Chem.*, 1980, **197**, 105–109.

9 C. Yu, W. X. Zhang and Z. Xi, *Organometallics*, 2018, **37**, 4100–4104.

10 G. Ganguly, S. Pathak and A. Paul, *Phys. Chem. Chem. Phys.*, 2021, **23**, 16005–16012.

11 M. A. Spackman and D. Jayatilaka, *CrystEngComm*, 2009, **11**, 19–32.a

12 P. R. Spackman, M. J. Turner, J. J. McKinnon, S. K. Wolff, D. J. Grimwood, D. Jayatilaka and M. A. Spackman, *J. Appl. Crystallogr.*, 2021, **54**, 1006–1011.

13 M. A. Spackman and J. J. McKinnon, *CrystEngComm*, 2002, **4**, 378–392.

14 C. P. Gordon, R. A. Andersen and C. Copéret, *Helv. Chim. Acta*, 2019, **102**, 1–11.

15 F. A. Cotton, *Chemical Applications of Group Theory*, John Wiley & Sons, Ltd, Third Edit., 1990.

16 S. Y. Chu and R. Hoffmann, *J. Phys. Chem.*, 1982, **86**, 1289–1297.

17 B. E. Bursten, F. Richard, B. E. Bursten and R. F. Fenske, *Inorg. Chem.*, 1979, **18**, 1760–1765.

18 D. Seyferth, *Organometallics*, 2004, **23**, 3562–3583.

19 C. J. Burns and B. E. Bursten, *Covalency in f-Element Organometallic Complexes: Theory and Experiment*, 1989, vol. 9.

20 T. Arliguie, L. Belkhiri, S. E. Bouaoud, P. Thuéry, C. Villiers, A. Boucekkine and M. Ephritikhine, *Inorg. Chem.*, 2009, **48**, 221–230.

21 J. T. boronski and S. T. Liddle, *Eur. J. Inorg. Chem.*, 2020, **2020**, 2851–2861.

Chapter 4: Cyclobutadienediide Coordination Polymers

4.1 Introduction:

The chemistry of the dianionic ligand Cb'''' (Cb'''' = 1,2,3,4,-*tetrakis*(trimethylsilyl)cyclobutadienediide, **Fig. 4.1 A**) has received a surge of attention recently as many predict that the Cb^{2-} moiety may lead to exceptional SMM properties in organometallic complexes with oblate Lanthanide ions (*vide supra)*, such as dysprosium (III), due to its incredibly strong near-linear coordination mode engendering magnetic axiality.[1–4]

While the chemistry of Cb'''' has been revived recently, the organometallic chemistry of no other cyclobutadienediide ligands have been explored outside of a small number of alkali metal salts. This paucity is likely due to their complex and extremely sensitive syntheses: most published routes leverage a cobalt (I) mediated (2+2) cycloaddition of acetylenes to synthesise and stabilise the unstable cyclobutadiene ring in one step.[5] From here, the alkali metal *trans*fer reagent, Li_2Cb'''', can be prepared *via* a reductive transmetallation with lithium metal in a coordinating solvent.[6–8]

However, no metallocenes of the type $[LnCb''''_2]^-$ (Ln = REE) have been isolated due to the high intrinsic reactivity of this ligand, which is prone to C-H activation, destroying the axial CF.[1,2] [Li_2Cb''''] has even been suggested for use as a powerful organometallic reducing agent, and was shown to be capable of reducing Thorium (IV) to Thorium metal.[9]

Two alternative cyclobutadienediide salts were reported by Sekiguchi, namely Li_2Cb^{cis} and Li_2Cb^{trans} (Cb^{cis} = 1,2-bisphenyl-3,4-bistrimethylsilylcyclobutadienediide, Cb^{trans} =1,3-bisphenyl-2,4-bistrimethylsilylcyclobutadienediide, **Figure 4.1, B**), however their organometallic chemistry has not been explored, likely due to the difficult separation of the geometric isomers, which was reported on a 50 mg scale utilising preparative TLC.

We were interested to know if the aforementioned lithium salts could be isolated on a scale that would facilitate exploratory organometallic chemistry. As only the organometallic chemistry of the Cb'''' (**Figure 4.1, A**) has been reported, this could offer new insights into 4f organometallic chemistry. The two phenyl substituents may act to stabilise the Cb^{trans} dianion through electronic delocalisation, and as such, may be less prone to C-H activation than Cb'''' (*vide supra)*.

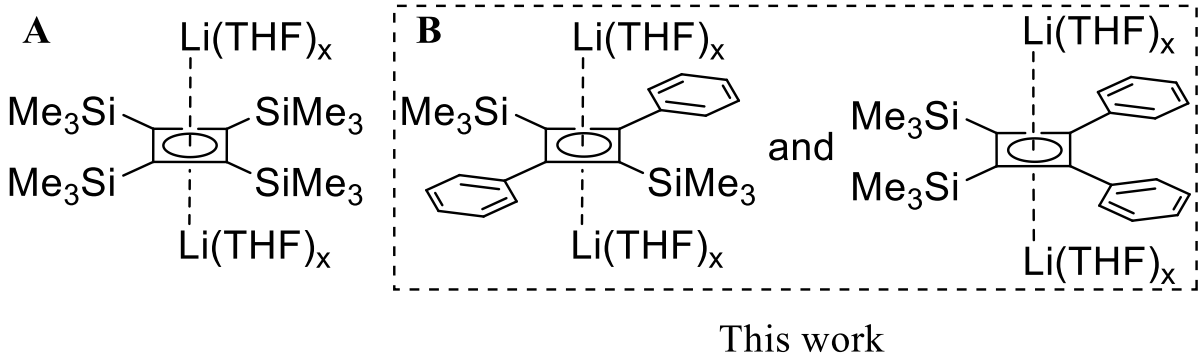

Figure 4.1 - Schematic representation of [Li_2Cb''''] (**A**), and [Li_2Cb^{trans}] and [Li_2Cb^{cis}](**B**).

4.2 Results and Discussion:

4.2.1 Synthesis:

Reported preparations for [$CoCpCb^{cis}$] and [$CoCpCb^{trans}$] were carried out on a small scale and were purified using preparative TLC, as they were discovered out of synthetic

curiosity.[5,7,10] We developed the route described in **Scheme 4.2** to prepare and isolate the two complexes on a 10 g scale to facilitate exploratory research. Firstly, the cobalt (I) precursor, [$CoCp(CO)_2$] is refluxed in Toluene with two equivalents of 1-phenyl-2-trimethylsilylacetylene under a nitrogen atmosphere for 72 hours. After cooling to room temperature, the mixed cyclobutadiene products can be separated from CO-insertion biproducts *via* column chromatography. The undesired side-products, appearing as red bands with R_f values < 0.1 are easily filtered off by dry loading the crude reaction mixture mixed with Celite® onto a silica-gel column and eluting with benzene. The mixed cyclobutadiene products, which elute as a single orange band with R_f = 0.6, can be collected and concentrated for the second stage of separation. To isolate [$CoCpCb^{cis}$] and [$CoCpCb^{trans}$], the mixture is dry loaded with Celite® onto a silica-gel column and eluting with PET ether (BP < 80°C). [$CoCpCb^{trans}$] elutes before [$CoCpCb^{cis}$], as orange bands with R_f values of 0.4 and 0.2 respectively. Best results were obtained by using a ratio of 1:100 g of mixed analyte to dry silica loaded in a 3 cm diameter glass column. Purity of the isomers can be verified using ^1H and ^{13}C spectroscopies, due to the different magnetic environments present in the *cis* and *trans* isomers (**Figures A9-12)**

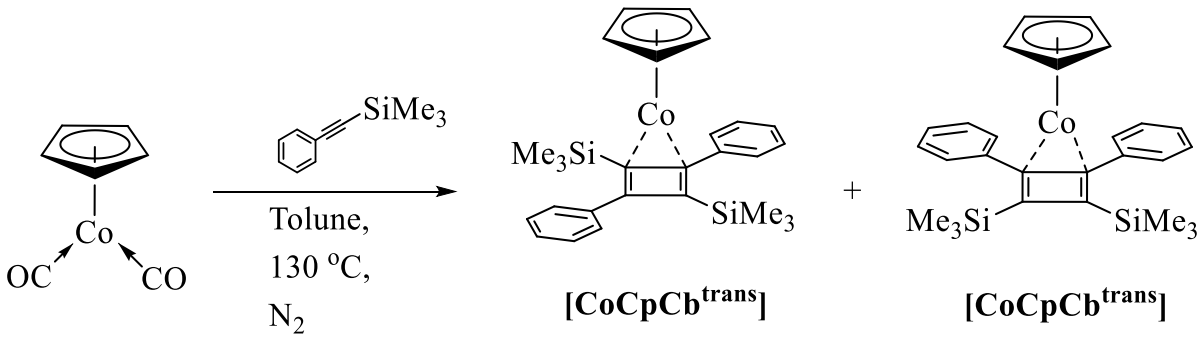

Scheme 4.1 - Synthetic scheme describing the preparation of [$CoCpCb^{trans}$] and [$CoCpCb^{cis}$].

The only reported route to transform MCpCb complexes into alkali metal transfer reagents is the elegant reductive transmetallation developed by Sekiguchi and co-workers.[7,8,11] Utilising this, we prepared the salts [Li_2Cb^{trans}] and [Li_2Cb^{cis}] by adding excess Li^0 metal (< 20 eq.) to a rapidly stirred solution of the respective CoCpCb precursor in thoroughly dry and degassed THF under an argon atmosphere for 72 hours (**Scheme 4.2**). On addition, the transparent orange solutions quickly darken to a violet suspension as the lithium pieces are consumed. After three days the deep violet-brown suspensions are filtered through Celite®, dried *in vacuo*, and the brown oil repeatedly extracted in hexanes. After filtering through Celite®, the deep-red solutions were cooled to -27 °C overnight to yield red-orange crystals of [Li_2Cb^{trans}] in 30 - 40 % yield on a 5 g scale. Alternative alkali metal reducing agents, such as Na^0 and K^0, were investigated, however only intractable mixtures were formed.

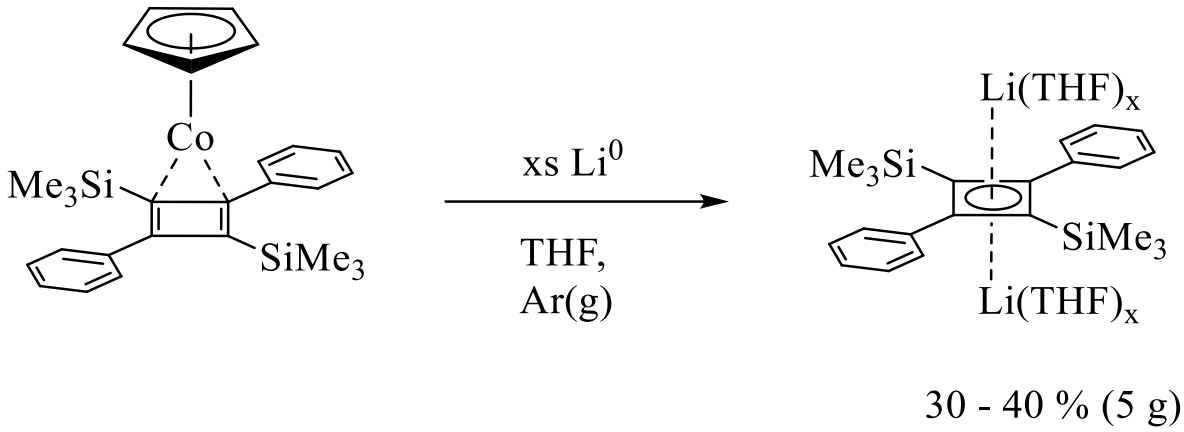

Scheme 4.2 - Synthetic scheme describing the preparation of [Li_2Cb^{trans}].

Once a route to usable quantities of [Li_2Cb^{trans}] salts was developed, we set out to investigate their organometallic chemistry with lanthanide ions because of their promising electronic properties. We first investigated reactions between [Li_2Cb] and dysprosium (III) borohydride salts, due to their solubility and assumed lability. A deep red solution of [Li_2Cb^{trans}] in THF was added dropwise to a pale-yellow solution of [$Dy(BH_4)_3(THF)_3$] in THF, which gradually became pale orange over the course of addition (**Scheme 4.3**). The solution was allowed to stir overnight at room temperature, after which it was filtered over Celite® and dried *in vacuo* to yield a tacky orange oil. Redissolving the oil in benzene and filtering through Celite® yielded a deep red solution. Slow diffusion of pentane into this solution at room temperature yielded red needle crystals of compound **4.1**, **[$DyCb^{trans}(\kappa^3$-$BH_4)((\mu$-$H)_2BH_4(Li(THF))_3)((\mu$-$H)_2BH_4(Li(THF)_2))]_\infty$** (*vide infra*) after three days.

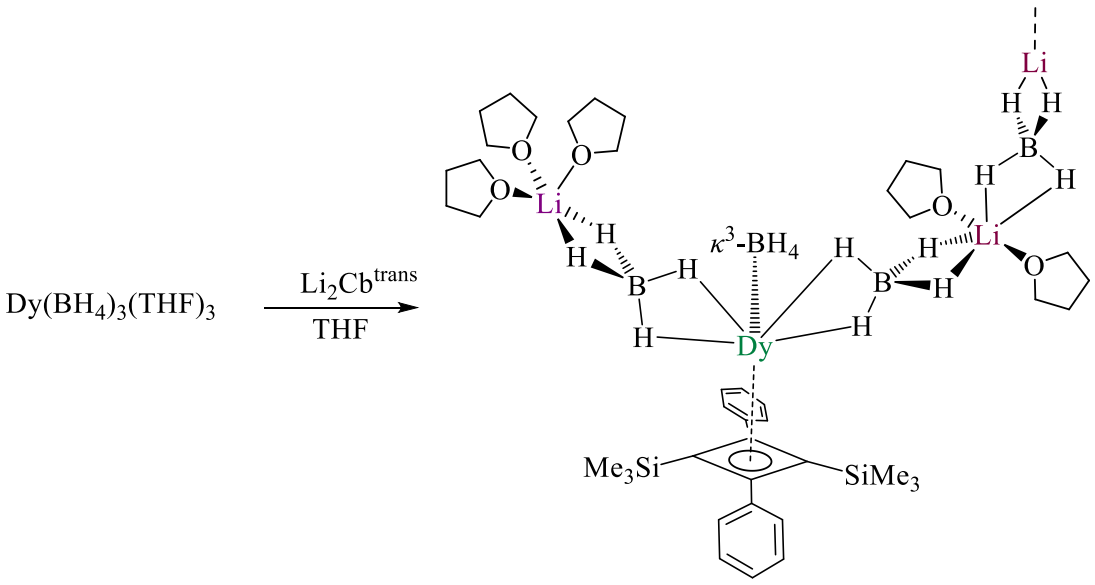

Scheme 4.3 - Synthetic scheme describing the preparation of compound **4.1**, [$DyCb^{trans}(\kappa^3$-$BH_4)((\mu$-$H)_2BH_4(Li(THF))_3)((\mu$-$H)_2BH_4(Li(THF)_2))]\infty$.

By analysing the charge balance in compound **4.1,** we can confirm that it is the first reported organometallic complex of Cb^{trans} in its dianionic form with a TM or REE.

Interestingly, compound **4.1** has some differences compared to an analogous Cb'''' dysprosium borohydride complex reported by Layfield and co-workers (designated Dy-

Cb’’’’).[3] Notably, Dy-Cb’’’’ has only two borohydride co-ligands bound to the dysprosium (III) centre, whereas **4.1** has three borohydride co-ligands, charge balanced by two lithium counter cations. This is likely due to the difference in ionic radii of Li^+ and Na^+. The ability of Lanthanide (III) ions to form salt-inclusion “ate complexes” due to their extreme Lewis acidity is known, and the {(μ-H)$_2$BH$_4$(Li(THF)$_x$))} motif has been identified previously.[12–15] However, to the best of our knowledge, no other Ln(III) complexes supported by an arenide ligand and three borohydride co-ligands has been reported. Compound **4.1** is reminiscent of a side-product that was identified during exploratory reactions with dysprosium pianostool, namely [DyCp*(κ^3-BH$_4$)$_2$((μ-H)$_2$BH$_4$)Li(THF)$_3$] **4.2**. Despite its serendipitous discovery, compound **4.2** could be obtained by adding lithium borohyride to a THF solution of [DyCp*(BH$_4$)$_3$(THF)] and crystallising from THF (**Scheme 4.4)**.

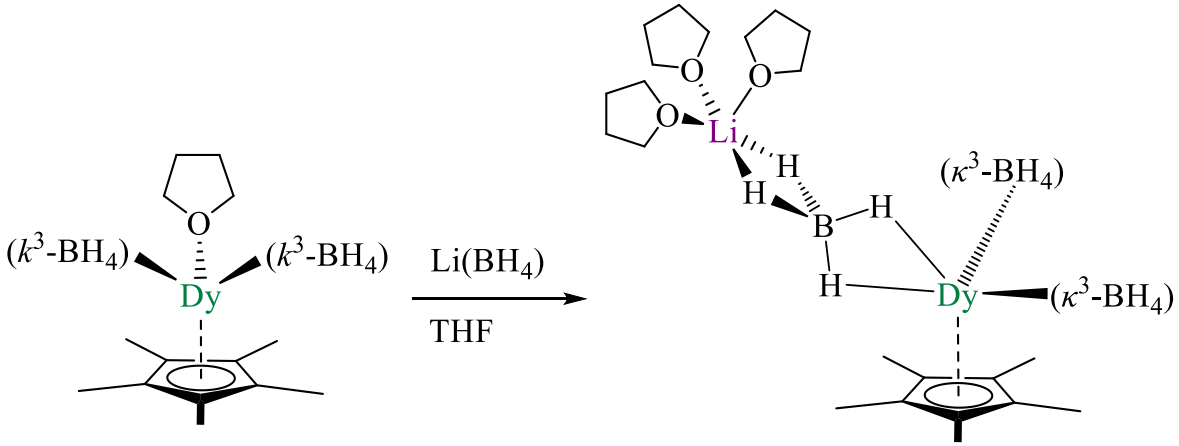

Scheme 4.4 - Synthetic scheme describing the preparation of [DyCp*(κ^3-BH$_4$)$_2$((μ-H)$_2$BH$_4$)Li(THF)$_3$] compound **4.2.**

We surmise that the kinetic and thermodynamic factors that stabilise the {Cp*Dy(κ^3-BH$_4$)$_2$((μ-H)$_2$BH$_4$(Li(THF))$_3$)} motif present in **4.2** may explain the formation of the {Cb^{trans}Dy(κ^3-BH$_4$)((μ-H)$_2$BH$_4$(Li(THF)$_x$)$_3$)$_2$} motif present in **4.1**. We observe that the borohdride ligands are able to sequester lithium cations and form the {((μ-H)$_2$BH$_4$(Li(THF))$_x$)} group, which is able to act as a neutral bridging or terminal ligand (dependant on the coordinative saturation of the lithium ion). The monoanionic nature of the Cp* ligand in **4.2**, compared to the dianionic Cb^{trans} in **4.1**, may be the reason that the former is a discrete complex while the latter is a coordination polymer in the solid state.

The reaction between [Li$_2$Cb^{trans}] and [DyCp*(BH$_4$)$_2$(THF)] was investigated to see if a discrete heteroleptic sandwich complex could be isolated (**Scheme 4.5**). Briefly: a deep-red solution of the [Li$_2$Cb^{trans}] in THF was added dropwise to a pale-yellow solution of [DyCp*(BH$_4$)$_2$(THF)] in THF. After stirring overnight under a nitrogen atmosphere, the resulting orange solution was filtered over Celite® and dried *in vacuo* to yield an orange oil. The oil was taken up in pentane, filtered through Celite®, and cooled to -27 ^{o}C to yield small red needle crystals of compound **4.3** after three days. SC-XRD analysis (*vide infra*) revealed that **4.3** forms a new coordination polymer structure.

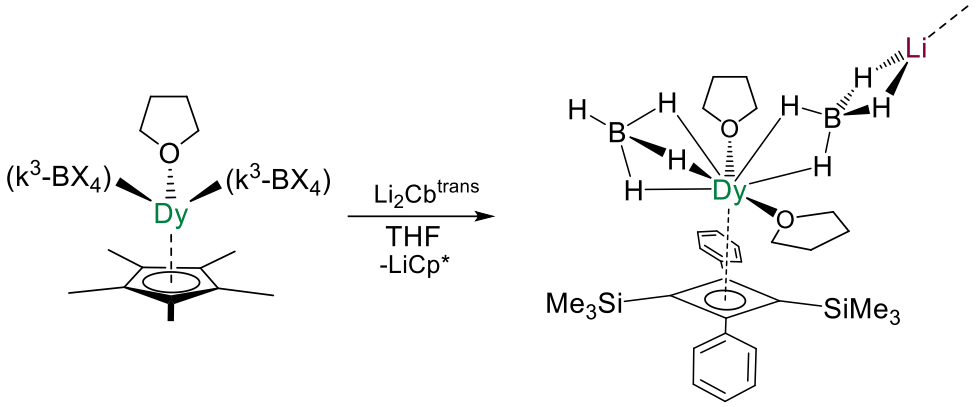

Scheme 4.5 - Synthetic scheme describing the reaction between [DyCp*$(BH_4)_2$(THF)] and [Li_2Cb^{trans}] to yield compound **4.3,** [$DyCb^{trans}(THF)_2(\kappa^3\text{-}BH_4)((\mu\text{-}H)_2BH_4)Li]\infty$.

The exclusion of Cp* was unexpected, as arenide rings are usually considered good ligands for Lanthanide (III) ions[16,17], however, **4.3** was obtained reproducibly. We can rationalise this as chelating ability of the BH_4 group, the dianionic charge of the Cb^{trans}, and the ability to form larger salt inclusion complexes by incorporating both of these moieties likely caused these ligands to out-compete the Cp* for metal coordination in the solid state. The Cp* was likely lost as LiCp* in solution, which can be rationalised by the stoichiometry in **Scheme 4.4**.

The reactions displayed in Schemes **4.2** and **4.3** were repeated with a stoichiometric addition of 12-crown-4 or 15-crown-5 ether (12-crown-4 = 1,4,7,10-Tetraoxacyclododecane, 15-crown-5 = 1,4,7,10,13-Pentaoxacyclopentadecane) to selectively sequester alkali metal cations, however no crystalline material was obtained.

Further test reactions were carried out using the [Li_2Cb^{cis}] isomer described in Scheme **4.1,** however no crystalline material was obtained.

4.2.2 Structural Analysis:

The structures discussed here were interrogated using SC-XRD analysis. Compound **4.1** crystallises in the monoclinic spacegroup $P2_1/c$, with unit cell parameters a = 11.3567(4) Å, b = 19.6768(8) Å, c = 24.399(1) Å, $\alpha = \gamma = 90^o$, β = 102.664(1)^o, V = 5319.6(4) Å^3, and two polymer chains within the unit cell. Each chain comprises a [$DyCb^{trans}(\kappa^3\text{-}BH_4)((\mu\text{-}H)_2BH_4(Li(THF))_3)((\mu\text{-}H)_2BH_4(Li(THF)_2))$] repeating unit. Each Dy centre (**Fig. 4.2**, **A**) is coordinated to an η^4-Cb^{trans} ligand with Dy-Cb_{Cg} = 2.3138(5) Å, a terminal κ^3-BH_4 with Dy-B_{BH4} = 2.525(7) Å, a terminal {$(\mu$-H)$_2BH_4(Li(THF)_3)$} group with Dy-B_{BH4} = 2.581(8) Å, and the polymer-extending {$(\mu$-H)$_2BH_4(Li(THF)_2)$} bridge with Dy-B_{BH4} = 2.632(6) Å. The three boron atoms sit on the corners of an equilateral triangle with average length B-B_{BH4} = 3.967(1) Å and average internal angle ∠B-B-B = 59.98(19)^o. The charge balance is completed with three lithium counter-cations per dysprosium (III) ion (**Fig. 4.2**, **B).** The first is coordinated to a {$(\mu$-H)$_2BH_4$Dy} moiety with Li_1-B_{BH4} = 2.512(11) Å, and three solvated THF molecules with average Li_1-O_{THF} = 1.929(11) Å. The second and third lithium cations are incorporated into the polymeric backbone; the first is coordinated to a{$(\mu$-H)$_2BH_4$Dy} moiety with Li_2-B_{BH4} = 2.636(13) Å, a {$(\mu$-H)$_2BH_4$Li} moiety with Li_2-B_{BH4} = 2.411(11) Å, and two solvated THF molecules with average Li_2-O_{THF} = 1.985(11) Å. The final lithium cation is coordinated to a {$(\mu$-H)$_2BH_4$Li} moiety with Li_3-B_{BH4} = 2.238(10) Å, and the opposite face of each Cb ring with Li-Cb_{cg} = 1.915(7) Å, extending the polymeric structure. The metal cations make an angle of ∠Li-Cb_{cg}-Dy = 178.30(20)^o with the arenide centroid.

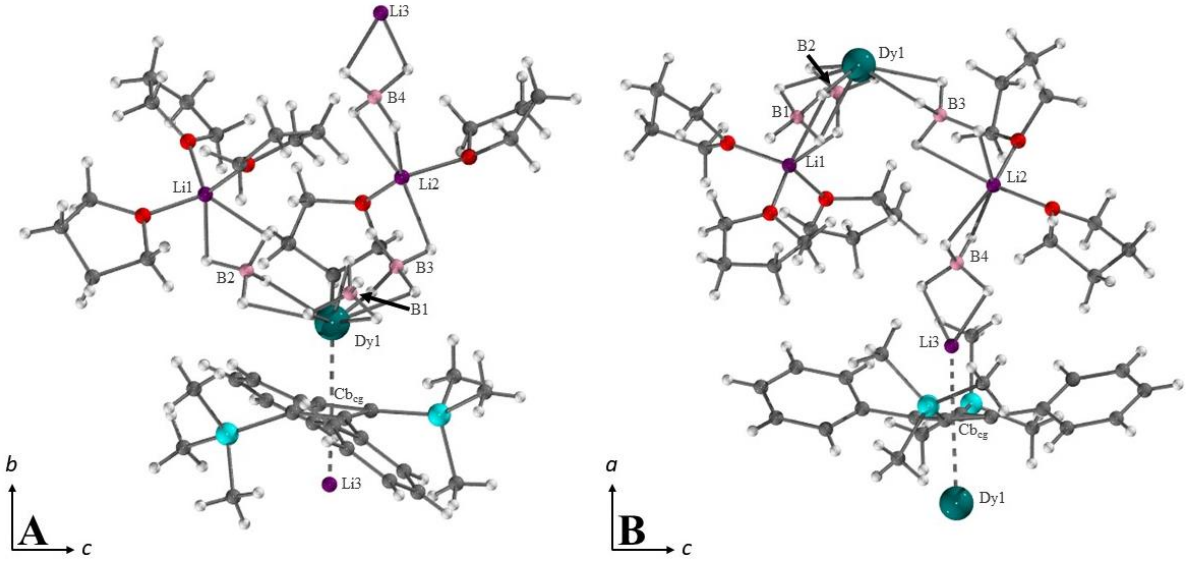

Figure 4.2 - Partial solid state molecular structures of compound **4.1** [DyCb^{trans}(κ^3-BH$_4$)((μ-H)$_2$BH$_4$(Li(THF)$_3$))((μ-H)$_2$BH$_4$(Li(THF)$_2$))]∞, highlighting the Dy (**A**) and Li (**B**) coordination spheres. Atoms were rendered as ball-and-sticks for clarity. Colour code: dysprosium, teal; lithium, violet; oxygen, red; carbon, grey; boron, pink; silicon, aqua

Table 4.1 - Selected interatomic distances in compound **4.1**

Label	**Distance (Å)**	**Label**	**Distance (Å) / Angle(º)**
Dy-Cb$_{cg}$	2.33233(6)	Li1-Cb$_{cg}$	1.896(20)
Dy-B1	2.533(20)	Li1-B2	2.282(26)
Dy-B2	2.830(17)	Li1-O3	176.68(60)
Dy-O1	2.438(8)	B2-Li2	2.636(13)
Dy-O2	2.452(9)	Li2-O4	1.933(10)

Looking at the extended chain, each dysprosium centre is separated by Dy-Dy$_{intra}$ = 12.2040(9) Å, while interatomic distance between chains is noticeably shorter with Dy-Dy$_{inter}$ = 11.3567(5) Å. The polymer chains alternate in a zig-zag pattern, which can be observed in the solid-state packing (**Fig. 4.3**).

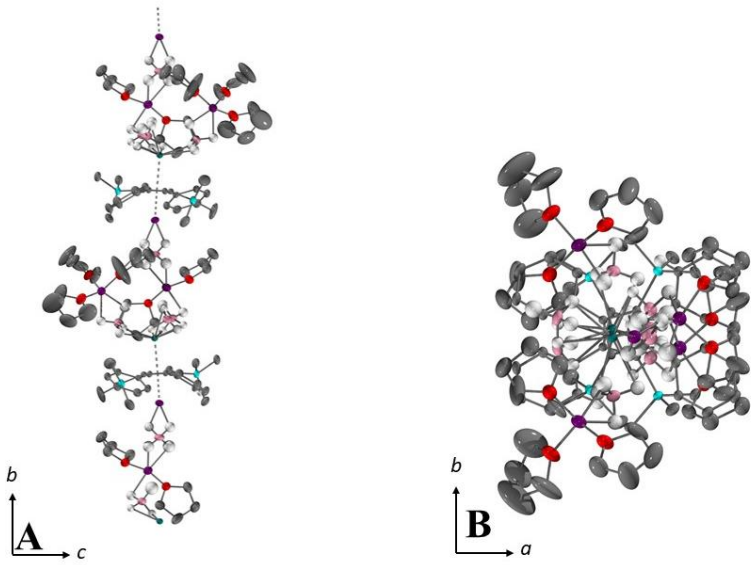

Figure 4.3 - Solid state molecular packing structure of compound **4.1** [DyCb^{trans}(κ^3-BH_4)((μ-H)$_2$$BH_4$(Li(THF)$_3$))(($\mu$-H)$_2$$BH_4$(Li(THF)$_2$))]$\infty$ viewed down the *a* (**A**) and *c* (**B**) crystallographic axes. Thermal ellipsoids were rendered at the 30 % probability level. Colour code: dysprosium, teal; lithium, violet; oxygen, red; carbon, grey; boron, pink; silicon, aqua. Non-coordinating hydrogen atoms were removed for clarity.

Crystals of compound **4.2** were extremely air and moisture sensitive, precluding full X-ray characterisation, so only connectivity will be described in detail. Compound **4.2** crystallises in the monoclinic spacegroup with lattice parameters a = 9.62(2) Å, b = 28.64(6) Å, c = 11.55(3) Å, $\alpha = \gamma = 90^o$, β =108.15(5)^o, V = 3024(12) Å^3, and two symmetry related [DyCp*(BH_4)$_2$((μ-H)$_2$$BH_4$(Li(THF)$_2$))] complexes in the unit cell (**Fig. 4.4**). Each complex comprises an η^5-Cp* bound dysprosium (III) centre and three borohydride co-ligands, two of which are terminal, and one coordinated to a solvated lithium cation. The three boron atoms sit on the corners of a distorted triangle.

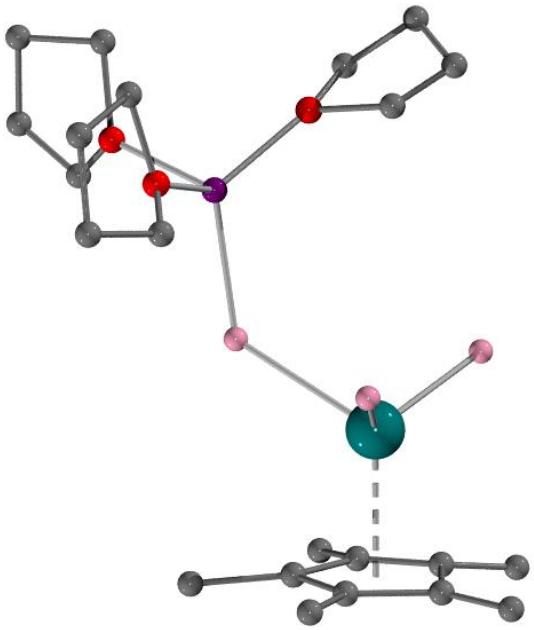

Figure 4.4 - Solid-state molecular structure of compound **4.2**. Colour code: dysprosium, teal; lithium, violet; oxygen, red; carbon, grey; boron, pink. Atoms were rendered as ball-and-sticks for clarity. Hydrogen atoms were removed for clarity.

Compound **4.3** crystallises in the orthorhombic space group $P2_12_12_1$ with lattice parameters a = 10.697(1) Å, b = 16.541(2) Å, c = 19.621(3) Å, $\alpha = \beta = \gamma = 90^o$, V = 3471.8(8) Å^3 and two polymer chains within the unit cell. Each coordination polymer is made of a [DyCb^{trans}(THF)$_2$(κ^3-BH$_4$)((μ-H)$_2$BH$_4$)Li] repeating unit. Each dysprosium centre (**Fig. 4.5**, **A**) is coordinated to an η^4-Cb^{trans} ligand with Dy-Cb$_{Cg}$ = 2.3233(6) Å, two borohydride ancillary ligands, a terminal κ^3-BH$_4$ with Dy-B$_1$ = 2.533(20) Å, and a bridging {(μ-H)$_2$BH$_4$} moiety with Dy-B$_2$ = 2.830(17) Å. The coordination sphere is completed by two solvated THF molecules, with Dy-O$_{THF}$ = 2.438(8) and 2.452(9) Å. The charge balance is completed by a lithium counter-cation (**Fig. 4.5**, **B**) which is coordinated to the opposite side of the Cb^{trans} ring with Li-Cb$_{Cg}$ = 1.896(20) Å, and the bridging {(μ-H)$_2$BH$_4$} group, with Li-B$_{BH4}$ = 2.282(26) Å. The two metal ions make an angle of ∠Li-Cb$_{Cg}$-Dy = 178.68(60)^o with the bridging arenide centroid.

Table 4.2 - Selected interatomic distances in compound **4.3.**

Label	**Distance (Å)**	**Label**	**Distance (Å) / Angle(^{o})**
Dy-Cb$_{cg}$	2.33233(6)	Li1-Cb$_{cg}$	1.896(20)
Dy-B1	2.533(20)	Li1-B2	2.282(26)
Dy-B2	2.830(17)	Li1-O3	176.68(60)
Dy-O1	2.438(8)	B2-Li2	2.636(13)
Dy-O2	2.452(9)	Li2-O4	1.933(10)

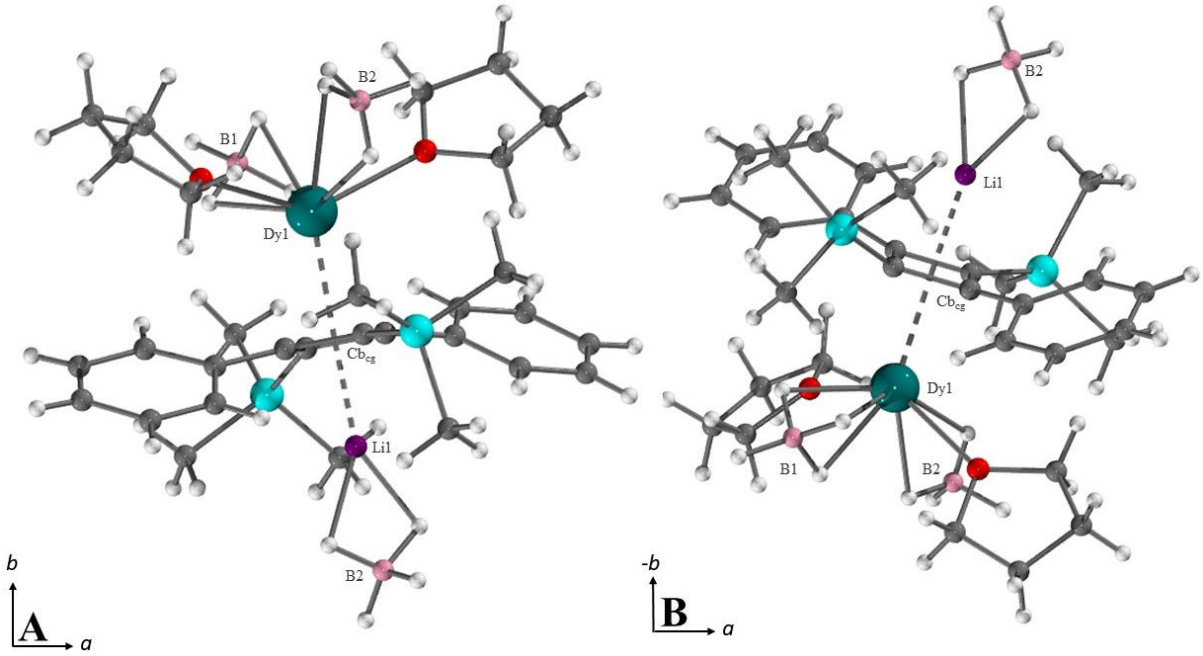

Figure 4.5 - Partial solid state molecular structure of compound **4.3**, [DyCb^{trans}(THF)$_2$(κ^3-BH$_4$)((μ-H)$_2$BH$_4$)Li]∞, highlighting the Dy (**A**) and Li (**B**) coordination spheres. Atoms were rendered as ball-and-sicks for clarity. Atoms were rendered as ball-and-sticks for clarity. Colour code: dysprosium, teal; lithium, violet; oxygen, red; carbon, grey; boron, pink; silicon, aqua.

Looking along the polymeric chains in compound **4.3**, each dysprosium centre is separated by a distance Dy-Dy$_{intra}$ = 9.279(1) Å, which is surprisingly slightly longer than in the reported Dy-Cb'''' (9.119 Å) which incorporates sodium cations, and almost 3 Å shorter than in **4.1** (12.2040 Å). Between chains, the shortest Dy-Dy distance in **4.3** is Dy-Dy$_{inter}$ = 10.332(1) Å, which is comparable to Dy-Cb'''' 10.968, and notably shorter than in **4.1** (11.8304 Å). The Dy polymers pack into alternating chains in the solid state (**Fig. 4.6**).

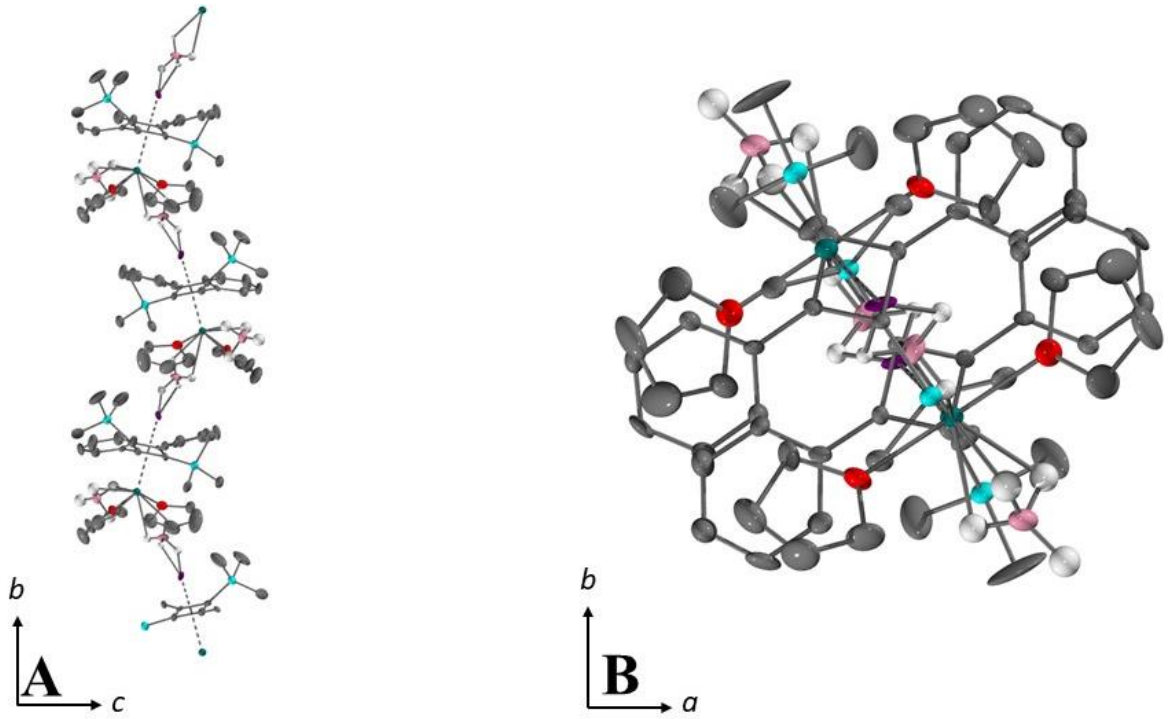

Figure 4.6 - Solid-state molecular packing in compound **4.3** shown down the *a* (**A**) and *b* (**B**), crystallographic axes. Thermal ellipsoids were rendered at the 30 % probability level. Non-coordinating hydrogen atoms were removed for clarity. Colour code: dysprosium, teal; carbon, grey; silicon, aqua; lithium, violet; boron, pink; hydrogen, white; oxygen, red.

4.3 Summary:

In this chapter a route to the gram scale isolation of [Li_2Cb^{cis}] and Li_2Cb^{trans}] is presented, and with it, the first organometallic chemistry of the Cb^{trans} cyclobutadienediide moiety with a rare earth ion is explored. Two different coordination polymers are reported and their solid-state molecular structures are described. These structures are related to reported structures incorporating the related Cb'''' ligand, and a discrete Cp* complex. With these results we demonstrate for the first time the utility of the Li_2Cb^{trans} and Li_2Cb^{cis} salts as alkali metal *trans*fer reagents and open the door to a new area of rare earth cyclobutadienediide chemistry.

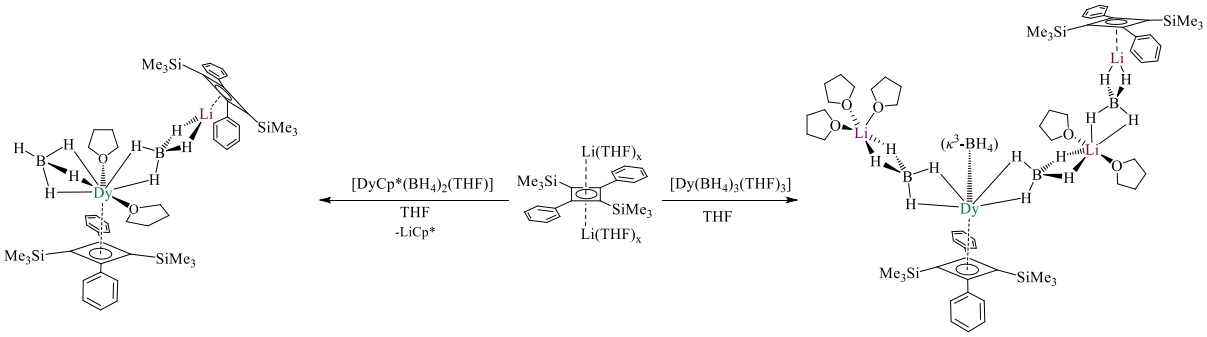

Scheme 4.6 - Synthetic scheme summarising the reactions described in chapter 4.

4.4 Experimental:

Materials and methods

All reactions and subsequent manipulations were performed under air-free and anhydrous conditions using standard Schlenk-line or nitrogen atmosphere glovebox techniques. Tetrahydrofuran, Toluene, and Hexanes were dried on columns of activated alumina using a J.C. Mayer solvent purification system, degassed with successive freeze-pump-thaw cycles, and stored over 4 Å molecular sieves in a nitrogen atmosphere glovebox prior to use. Celite® used for filtration was dried under vacuum while heating at 200 °C for 120 h, subsequently cooled under vacuum, and stored under nitrogen before use. HCp* was purchased from Sigma Aldrich, thoroughly degassed by successive freeze pump thaw cycles, and stored under nitrogen over 4 Å sieves before use. [$CoCp(CO)_2$] was purchased from Sigma Aldrich, was stored at -27 ^oC under nitrogen, and was used without further purification. Lithium borohydride was purchased from Sigma Aldrich, dried *in vacuo*, and stored under nitrogen prior to use. Lithium granules were purchased from Sigma Aldrich and stored under argon prior to use. Potassium hydride in a mineral oil suspension was purchased from Sigma Aldrich and was washed thoroughly with hexanes and dried before use. [$Dy(BH_4)_3(THF)_3$] and [$DyCp^*(BH_4)_2(THF)$] were prepared as described in **Chapter 2**. Phenylacetylene and TMS chloride were purchased from Sigma Aldrich and were used without further purification.

Infrared spectra were recorded on a Nicolet Nexus 550 FTIR spectrometer using *trans*mission mode in the 4000-600 cm^{-1} range; solid samples were prepared under an inert atmosphere and sandwiched between *trans*parent NaCl plates. NMR spectra were acquired on a Bruker Avance-II 300 MHz spectrometer at 298 K. Elemental analysis were conducted by Midwest Microlab, Indianapolis.

Single-Crystal Xray measurements: Single crystals suitable for single-crystal X-ray diffraction (SCXRD) analysis were covered in paraffin oil and mounted on a thin glass fiber. Full data was collected on a Bruker AXS SMART APEX-II CCD single-crystal diffractometer (graphite monochromated Mo-Kα radiation, λ = 0.71073 Å), at 200 K temperature. Absorption corrections were applied by using multi-scan of the SADABS[1] program. Structures were solved using direct methods with SHELXT[2] and refined by the full-matrix least-squares methods on F^2 with SHELXL-2018/3[3] in anisotropic approximation for all non-hydrogen atoms.

Synthesis of 1,2-TMSphenylacetylene:

1,2-trimethylsilylphenylacetylene was prepared using a modified literature procedure:

5.0 g (49 mM) of phenylacetylene was dissolved in 30 mL of THF and cooled to -78 ^oC under a nitrogen atmosphere. With stirring, 23 mL of ^{n}BuLi solution (2.5 M in hexanes, 53 mM) was added dropwise *via* cannula. Once addition was complete, the orange suspension was allowed to warm to room temperature and was stirred at room temperature for 2 hours. The red suspension was then cooled to -78 ^oC, and 5.7 g (6.8 mL, 53 mM) TMS chloride was added dropwise *via* syringe. On addition, the orange suspension immediately became clear with a thick white precipitate. The suspension was allowed to warm to room temperature and was stirred at room temperature overnight. Once complete, the reaction was quenched by pouring over a saturated solution of ammonium nitrate and was extracted 3 x 30 mL with

PET ether. The combined extracts were washed 3 x 30 mL water, dried over magnesium sulfate, filtered, and concentrated *in vacuo* to yield a translucent yellow oil. Vacuum distillation yielded 6.5 g (37 mM, 75 %) of 1,2-trimethylsilylphenylacetylene as a colourless oil.

Synthesis of [CoCpCb^{trans}] and [CoCpCb^{cis}]:

The compounds were prepared using a modified literature procedure:

3.0 g (16.65 mM) of [CoCp(CO)$_2$] (17 mM) was added to a solution of 5.8 g (33 mM) 1,2-trimethylsilylphenylacetylene in 20 mL toluene under a nitrogen atmosphere. Once addition was complete, the red solution was heated to reflux (bath temperature 130 ^{o}C) and refluxed under dynamic nitrogen for 72 hours while covered in foil to exclude light. Once complete, the solution was allowed to cool to room temperature, filtered over filter paper into a round bottomed flask, and dried *in vacuo* to a deep red solid. The red solid was mixed with a small amount of Celite® (about 0.5 g) and DCM (10 mL) and was dried slowly while mixing to achieve a homogenous dispersion. The dry loaded product was placed onto a column of silica gel saturated with benzene and was eluted with approximately 1 L benzene. The desired products elute first as an orange band with Rf = 0.7. The undesired biproducts elute as a black-red band with Rf < 0.1. The products were collected, combined, and dried *in vacuo* to give 5.5 g (10.5 mM, 63 % total) of mixed *cis*/*trans*-[CoCpCb] as a deep red microcrystalline powder.

To separate the *cis* and *trans* isomers, 1 g of mixed *cis/trans*-[CoCpCb] was dry loaded as before onto a column of 100 g silica gel saturated with PET ether (BP < 80 ^{o}C) and was eluted with approximately 1 L PET ether. The *trans* isomer, [CoCpCb^{trans}], elutes first as an orange band with Rf = 0.4, and the *cis* isomer elutes last as an orange band with Rf = 0.2. The *cis* and *trans* isomers were collected, dried *in vacuo*, and crystallised from evaporating acetone to yield 0.5 g [CoCpCb^{trans}], and 0.4 g [CoCpCb^{cis}] respectively.

Synthesis of [Li$_2$Cb^{trans}]:

A round-bottomed flask was charged with 1.0 g of [CoCpCb^{trans}] (2.1 mM) and 30 mL of dry, degassed THF. 0.8 g (120 mM) of fresh lithium granules were added at once under a dynamic flow of argon while stirring rapidly. The clear orange solution quickly darkened to violet as the lithium metal was consumed. The suspension was allowed to stir at room temperature for 72 hours, after which it was dried thoroughly *in vacuo* and brought inside a nitrogen atmosphere glovebox. The tacky red oil was redissolved in 3x 30 mL hexanes and filtered through Celite®, yielding a deep red solution. Cooling this solution to -27 ^{o}C yielded 0.42 g (0.83 mM, 40 %) of [Li$_2$(THF)$_x$Cb^{trans}] as a deep red microcrystalline solid.

Synthesis of [DyCb^{trans}(κ^3-BH$_4$)((μ-H)$_2$BH$_4$(Li(THF)$_3$))((μ-H)$_2$BH$_4$(Li(THF)$_2$))]$_\infty$ - 4.1

A deep red solution of 50 mg (0.098 mM) Li$_2$Cb^{trans} in 5 mL THF was added dropwise to a rapidly stirred pale yellow solution of 43 mg (0.1 mM) [Dy(BH$_4$)$_3$(THF)$_3$] in 3 mL THF. The solution gradually darkened to pale red as the reagent was consumed. After complete addition, the solution was left to stir at room temperature for 16 hours. The resultant pale-orange solution was dried *in vacuo*, redissolved in 3x mL benzene, and filtered through Celite® to give a pale red solution. Slow diffusion of pentane into this solution at room temperature yielded **4.1** as 20 mg of small red crystals after three days.

Synthesis of [DyCp*$(BH_4)_2$(μ-BH_4)Li] - 4.2

0.011 g (0.5 mM) of $LiBH_4$ was added to a solution of 0.1 g (0.25 mM) [DyCp*$(BH4)_2$(THF)] in THF with stirring. The pale-yellow suspension was allowed to stir overnight at room temperature. The resultant pale-yellow suspension was filtered through Celite® and concentrated *in vacuo* until incipient precipitation, after which the solids were redissolved with light heating before cooling to -27 °C. After 3 days a mixture of pale-yellow block crystals were obtained, including [DyCp*$(BH_4)_2$(μ-BH_4)Li$(THF)_3$] and [DyCp*$(BH_4)_2$(THF)].

Synthesis of [DyCb^{trans}(THF)$_2$(κ^3-BH_4)(κ^2-μ-BH_4)Li]$_\infty$ - 4.3

A deep red solution of 0.08 g [Li_2Cb^{trans}] (0.0197 mM) in 5 mL THF was added dropwise to a rapidly stirred pale yellow solution of 0.01 g [DyCp*$(BH4)_2$(THF)] (0.0197 mM) in 3 mL THF. The solution gradually darkened to pale red as the reagent was consumed. After complete addition, the solution was left to stir at room temperature for 16 hours. The resultant pale-orange solution was dried *in vacuo*, redissolved in 3x mL Pentane, and filtered through Celite® to give a pale red solution. Cooling this solution to -27 °C yielded **4.3** as 5 mg red needle crystals of after three days.

4.5 References:

1 B. M. Day, F. S. Guo, S. R. Giblin, A. Sekiguchi, A. Mansikkamäki and R. A. Layfield, *Chem. Eur. J.*, 2018, **24**, 16779–16782.

2 A. Chakraborty, B. M. Day, J. P. Durrant, M. He, J. Tang and R. A. Layfield, *Organometallics*, 2020, 39, 1, 8-12.

3 J. Durrant, J. Tang, A. Mansikkamäki and R. Layfield, *Chem. Commun.*, 2020, **4**, 4–7.

4 J. T. boronski and S. T. Liddle, *Eur. J. Inorg. Chem.*, 2020, **2020**, 2851–2861.

5 H. Sakurai and J. Hayashi, *J. Organomet. Chem.*, 1972, **39**, 365–370.

6 A. Sekiguchi, T. Matsuo and H. Watanabe, *J. Am. Chem. Soc.*, 2000, 122, 5652–5653.

7 A. Sekiguchi, T. Matsuo and M. Tanaka, *Organometallics*, 2002, **21**, 1072–1076.

8 T. Matsuo and A. Sekiguchi, *Bull. Chem. Soc. Jpn.*, 2004, **77**, 211–226.

9 J. T. boronski, A. J. Wooles and S. T. Liddle, *Chem. Sci.*, 2020, **11**, 6789–6794.

10 C. Kabuto, J. Hayashi, H. Sakurai and Y. Kitahara, *J. Organomet. Chem.*, 1972, **43**, 23–25.

11 A. Sekiguchi, T. Matsuo and W. Hidetoshi, *J. Am. Chem. Soc.*, 2000, **2**, 5652–5653.

12 A. V. Khvostov, V. K. Belsky, A. I. Sizov, B. M. Bulychev and N. B. Ivchenko, *J. Organomet. Chem.*, 1998, **564**, 5–12.

13 T. J. Marks, H. Schumann, P. N. Swepston, L. E. Schock and G. Jeske, *J. Am. Chem. Soc.*, 1985, **107**, 8103–8110.

14 W. J. Evans, J. W. Ziller and T. J. Boyle, *Inorg. Chem.*, 1992, **31**, 1120–1122.

15 F. Bonnet, M. Visseaux, D. Barbier-Baudry, A. Hafid, E. Vigier and M. M. Kubicki, *Inorg. Chem.*, 2004, **43**, 3682–3690.

16 W. J. Evans, *Organometallics*, 2016, **35**, 3088–3100.

17 B. M. Day, F. S. Guo and R. A. Layfield, *Acc. Chem. Res.*, 2018, **51**, 1880–1889.

Chapter 5: Breaking the Cyclobutadienediide Chain

5.1 Introduction:

Weak, non-covalent interactions have recently been highlighted by us and others as a route to prepare discrete polynuclear organometallic complexes[1–4] and improve the spin-relaxation properties of multinuclear SMMs.[5,6] Close contacts such as these can be engendered through the incorporation of polarisable organic moieties, such as the $C^{\delta-}$–$Si^{\delta+}$ bond in SiR_3 groups[7–9], or the delocalised π clouds of conjugated groups[10–12]. Additionally, agostic interactions have been investigated for enhanced small molecule activation and catalysis in organometallic systems.[13,14] Weak interactions are non-trivial to predict due to their complex environmental sensitivity, and as such, developing new design strategies to direct them is an unmet challenge in organometallic chemistry.

Our aim was to investigate if discrete Lanthanide cyclobutadienediide complexes could be accessed by utilising bulky cyclic organoboranes co-ligands, a design strategy which has not been explored previous in organometallic chemistry. To this end, we utilised the bulky cyclic organoborane 9-BBN (9-BBN = 9-bisboracyclononane, $HBBN^-$ = 9-bisboracyclononane hydroborate anion, $H_2BC_8H_{14}$) as an organometallic co-ligand, expecting that its bulky cyclohexyl-like substituents and limited κ^2-coordination mode would hinder polymerisation. No HBBN salts of the Ln(III) ions have been reported, however stable Ln(II) HBBN salts (for Ln = Eu, Yb) have been identified.[15].

5.2 Results and Discussion:

5.2.1 Synthesis:

The ligand precursor, 9-BBN dimer is commercially available as a neutral diborane species. Treatment of 9-BBN dimer with excess KH in THF yields KHBBN after work-up, which can be used to prepare 9-BBN hydroborate complexes *via* salt metathesis, analogous to KBH_4 (**Scheme 5.1**).

In pursuit of the first Lanthanide (III) HBBN salts, $DyCl_3$ was treated with excess KHBBN in refluxing THF for 72 hours. The resulting pale-yellow suspension was filtered through Celite®, reduced in volume, and cooled to -27 °C to yield pale-yellow block crystals of compound **5.1**, **$[K(THF)_6][Dy(HBBN)_4(THF)_2]$** (v*ide infra*). The crystals were extremely air and moisture sensitive, likely owing to the easily desolvated $\{K(THF)_6\}^+$ moiety. Varying stoichiometries, from 1:2 to 1:5 Dy:HBBN were investigated, however only the 1:4 species compound **5.1** was observed.

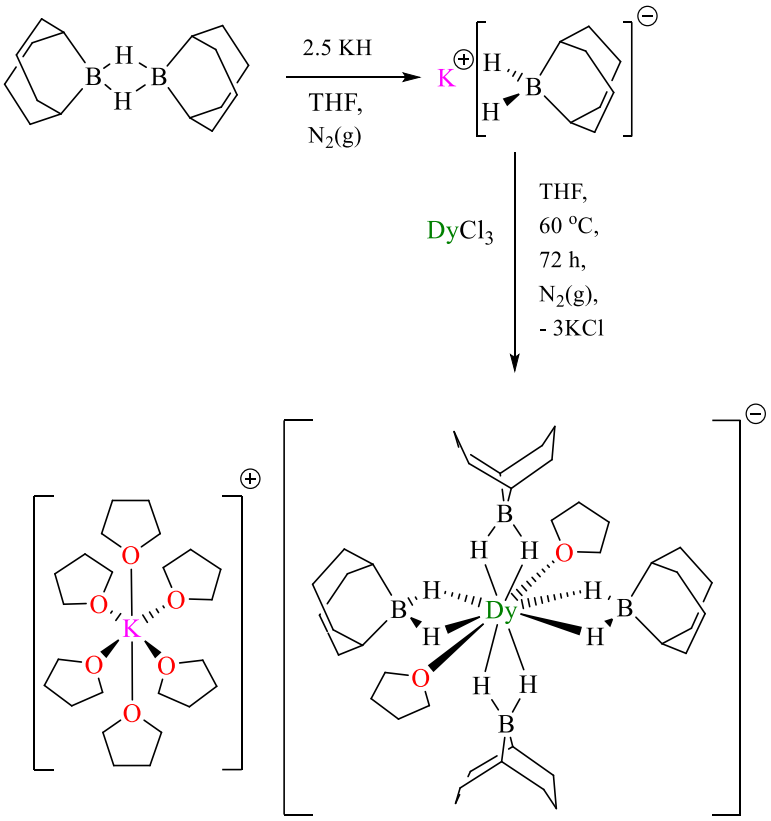

Scheme 5.1 - Synthetic scheme describing preparation of KHBBN and compound **5.1** $[K(THF)_6][Dy(HBBN)_4(THF)_2]$.

In order to investigate the reactivity of the dysprosium HBBN salt with cyclobutadienediide, a solution of **5.1** was treated with $[Li_2Cb^{trans}]$ in THF (**Scheme 5.2**). Briefly: A deep red solution of $[Li_2Cb^{trans}]$ was added dropwise to a pale yellow solution of compound **5.1, [K(THF)$_6$][Dy(HBBN)$_4$(THF)$_2$]** at room temperature. The solution darkened from turbid yellow to translucent orange over the course of addition, after which it was allowed to stir overnight. The resulting orange solution was dried *in vacuo* to yield a tacky orange oil. The oil was extracted with pentane and the deep-red solution was filtered through Celite® and cooled to -27 °C overnight to yield small red needle crystals of compound **5.2 [Dy(κ^3-HBBN)(κ^2-HBBN)(THF)(μ-Cb^{trans})Li(THF)]**.

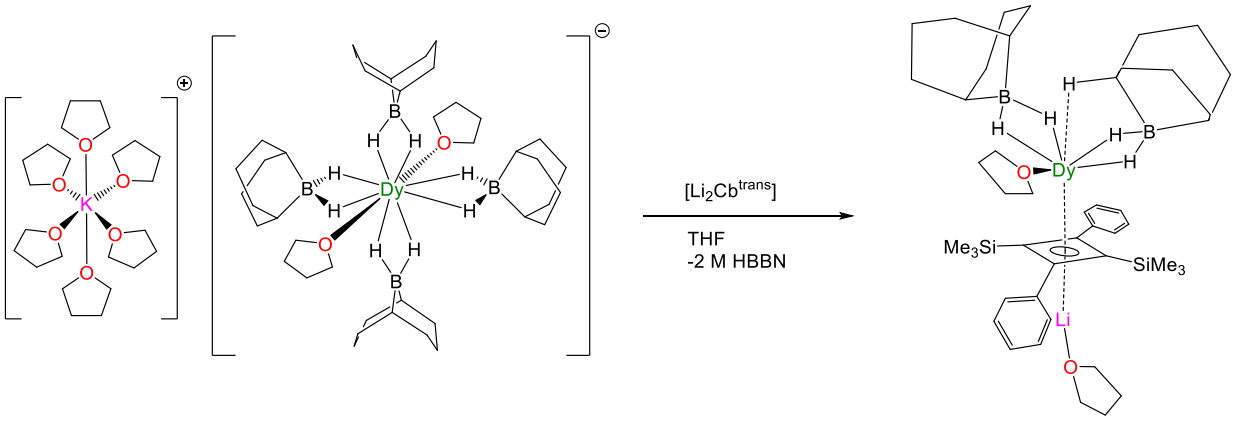

Scheme 5.2 - Synthetic scheme describing the preparation of compound **5.2**, [Dy(κ^3-HBBN)(κ^2-HBBN)(THF)(μ-Cb^{trans})Li(THF)].

After extraction of the crude reaction mixture with hexanes it was noted that a tacky red residue was left. Extraction of this residue with benzene, and filtration through Celite® yielded a pale red solution. Slow diffusion of pentanes onto this solution for one week yielded red needle crystals of compound **5.3**, **[Dy(κ^3-HBBN)(κ^2-HBBN)(THF)(μ-Cb^{trans})K(THF)]$_4$.**.

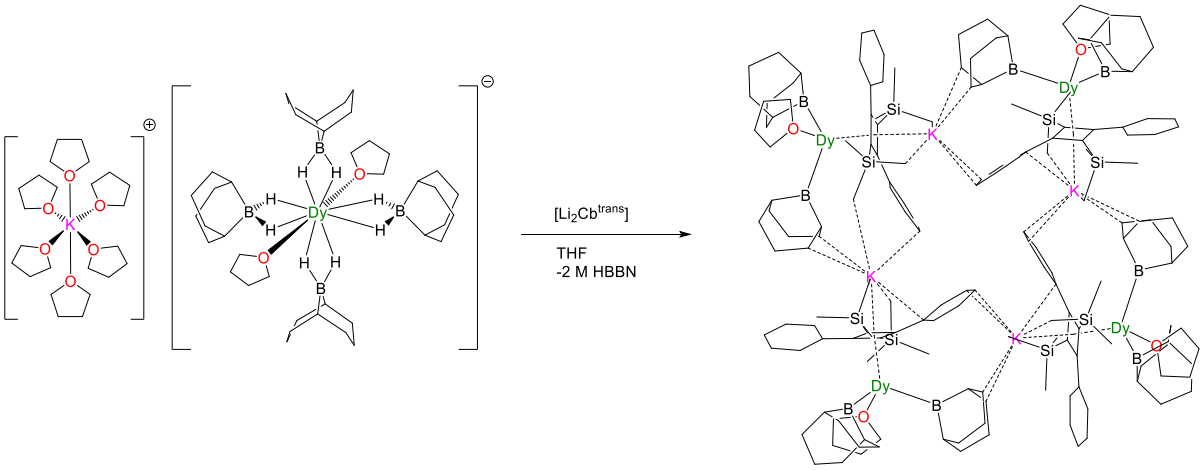

Scheme 5.3 - Synthetic scheme describing preparation of compound **5.3**, [Dy(HBBN)$_2$(THF)(μ-Cb^{trans})K(THF)].

5.2.2 Structural Analysis:

The solid-state molecular structures of the compounds described were interrogated via SC-XRD analysis. Compound **5.1** crystallises in the Triclinic spacegroup P-1, with unit cell parameters a = 11.38(2) Å, b = 11.58(3) Å, c = 14.17(3) Å, α = 77.95(4)°, β = 79.92(4)°, γ = 77.94(4)°, V = 1769(6) Å^3, and one solvent separated ion pair (SSIP) within the unit cell. Several crystals were measured, however their extreme air and moisture sensitivity precluded full data collection, so only connectivity will be described in detail. Similar issues were reported with [Ln(HBBN)$_4$K(THF)$_2$] (Ln = Eu(II), Yb(II)). Each SSIP **(Figure 5.1)** comprises a pseudo-octahedral {K(THF)$_6$}$^+$ cation and a 10-coordinate {Dy(HBBN)$_4$(THF)$_2$}$^-$ anion, in which the dysprosium centre is bound to four κ^2-HBBN

ligands whose B atoms occupy the corners of a square. The coordination sphere is completed with two axially coordinated solvated THF molecules.

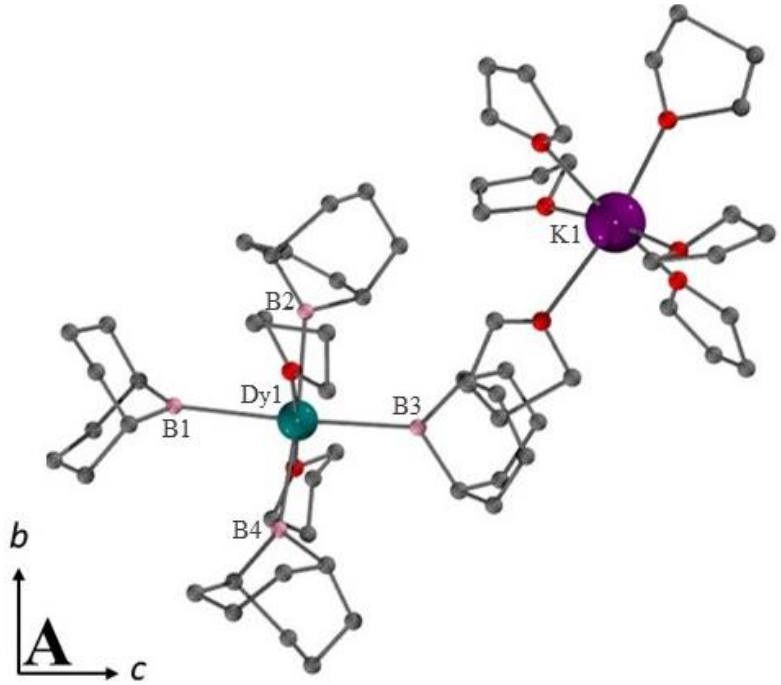

Figure 5.1 - Solid-state molecular structure of compound **5.1**, $[K(THF)_6][Dy(HBBN)_4(THF)_2]$. Hydrogen atoms were removed for clarity. Atoms were rendered as ball-and-sticks for clarity. Colour code: dysprosium, teal; potassium, violet; oxygen, red; carbon, grey; boron, pink.

Table 5. 1 - Selected interatomic distances in compound **5.1**, $[K(THF)_6][Dy(HBBN)_4(THF)_2]$.

Label	**Distance (Å)**	**Label**	**Distance (Å) / Angle(º)**
Dy-B1	2.807(23)	Dy-O2	2.443(19)
Dy-B2	2.748(21)	K-O3	2.688(22)
Dy-B3	2.718(28)	O1-Dy-O2	174.98(53)
Dy-B4	2.756(21)	B1-Dy-B2	86.04(68)
Dy-O1	2.430(16)	B3-Dy-B4	93.44(86)

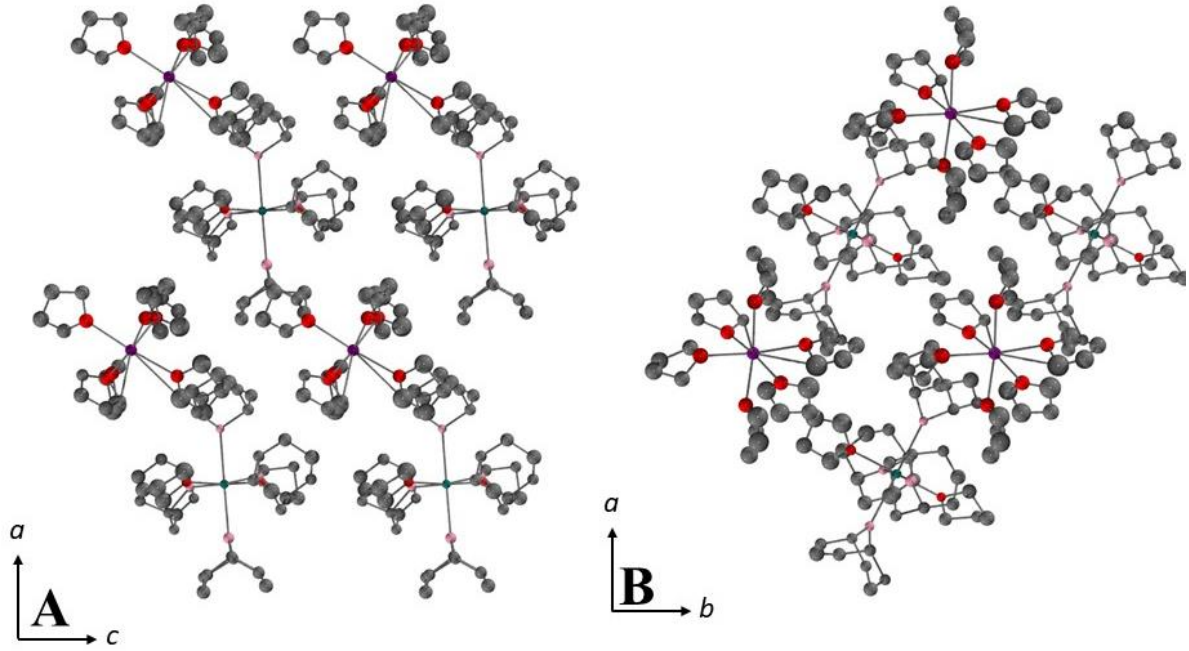

Figure 5.2 - Solid-state molecular packing in compound **5.1** viewed down the *b* (A), and *c* (**B**) crystallographic axes. Hydrogen atoms were removed for clarity. thermal ellipsoids were rendered at the 30 % probability level. Non-coordinating hydrogen atoms were removed for clarity. Colour code: dysprosium, teal; potassium, violet; oxygen, red; carbon, grey; boron, pink.

Compound **5.2** (**Fig. 5.3**) crystallises in the triclinic spacegroup P-1, with lattice parameters a = 15.20(7) Å, b = 17.71(8) Å, c = 19.05(8) Å, α = 82.87(7)°, β = 89.82(11)°, γ = 89.96(6)°, V = 5088(39) Å^3, and two crystallographically equivalent molecules in the unit cell. The complex comprises a dysprosium (III) ion bound to an η^4-Cb^{trans} ligand with Dy-Cb$_{Cg}$ = 2.294(7) Å, two κ^2-HBBN ancillary ligands, one of which shows a symmetric coordination mode with Dy-B$_1$ = 2.51(3) Å and a γ-agostic CH···Dy interaction at Dy-H$_{CH}$ 2.5(2) Å *via* a bridgehead proton, while the other shows an asymmetric coordination mode with Dy-B$_2$ = 2.85(5) Å. The noticeably longer Ln-B$_{HBBN}$ distance of the asymmetrically bound ligand and the agostic interaction are consistent with literature reports.[15] Finally, the coordination sphere is complete with a solvated THF molecule where Dy-O$_{THF}$ = 2.362(20) Å. The lithium counter-cation is coordinated to the opposing face of the ring with Li-Cb$_{cg}$ = 1.919(58) Å, consistent with the parent Li$_2$Cb^{trans} salt (2.070 Å)[16] and the polymer structures presented in Chapter **4** (**4.1** =, 1.897 Å, **4.2** = 1.911 Å,). Finally, the ∠Li-Cb-Dy angle is 178.1(17)°.

As described previously, all reported lanthanide cyclobutadienediide systems reported have formed coordination polymers in the solid state. **5.2** is therefore the first discrete lanthanide cyclobutadienediide complex, validating our design strategy. The two crystallographically equivalent molecules are related by a centre of inversion, with the closest intermolecular distance Dy-Dy$_{int}$ = 10.969(37) Å^3,

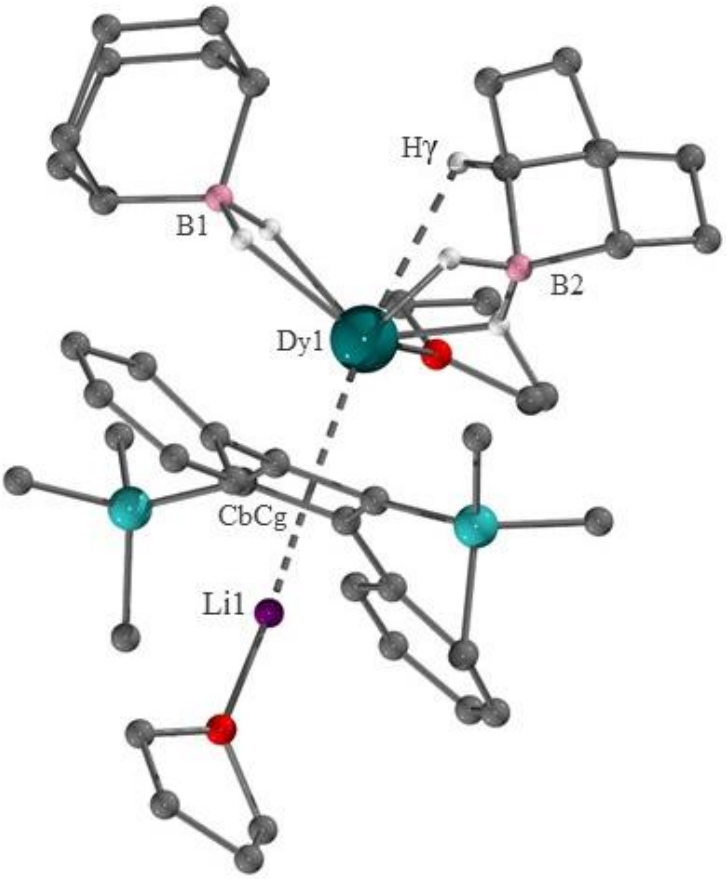

Figure 5.3 - Solid-state molecular structure of compound [Dy(κ^3-HBBN)(κ^2-HBBN)(THF)(μ-Cb^{trans})Li(THF)] **5.2** . Atoms were rendered as ball-and-sticks and non-interacting hydrogen atoms were removed for clarity. Colour code: dysprosium, teal; lithium, violet; oxygen, red; carbon, grey; boron, pink; silicon, aqua.

Table 5.2 - Selected interatomic distances in [Dy(κ^3-HBBN)(κ^2-HBBN)(THF)(μ-Cb^{trans})Li(THF)] compound **5.2.**

Label	**Distance (Å)**	**Label**	**Distance (Å) / Angle(º)**
Dy-Cb$_{cg}$	2.294(7)	Li1-Cb$_{cg}$	1.919(58)
Dy-B1	2.850(45)	Li1-O2	1.790(53)
Dy-B2	2.516(32)	Li1-Cb$_{cg}$-Dy1	178.4(16)
Dy-Hγ	2.464(162)	B1-Dy-B2	86.04(68)
Dy-O1	2.362(20)	B3-Dy-B4	93.44(86)

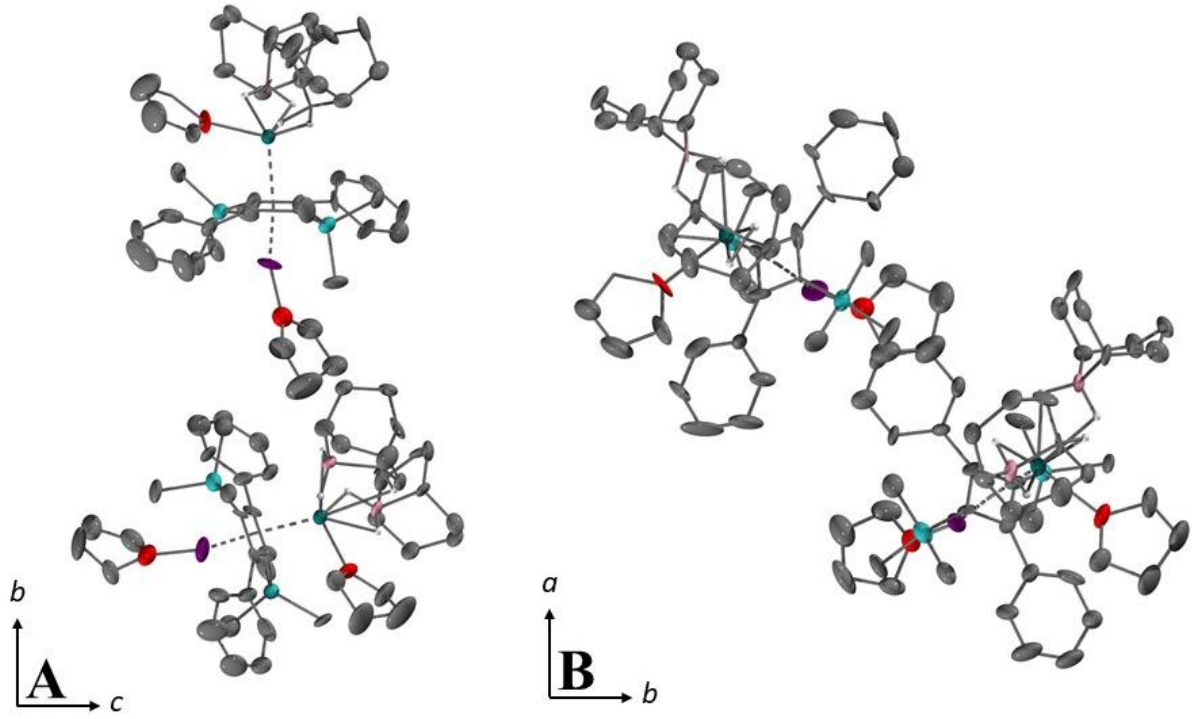

Figure 5.4 - Solid-state molecular packing of compound **5.2** viewed down the *a* (**A**) and *C* (**B**) crystallographic axes. Thermal ellipsoids were rendered at the 30 % probability level. Non-coordinating hydrogen atoms were removed for clarity. Colour code: dysprosium, teal; lithium, violet; oxygen, red; carbon, grey; boron, pink; silicon, aqua.

Compound **5.3** crystallises in the tetragonal spacegroup, $P4_2/n$, with cell parameters: $a = b = 24.786(2)$ Å, $c = 18.053(2)$ Å, $\alpha = \beta = \gamma = 90^o$, V = 11090(1) Å^3, and two tetramer [Dy(HBBN)$_2$(THF)(μ-Cb^{trans})K(THF)] molecules within the unit cell. The tetrameric units are composed of four crystallographically equivalent dysprosium (III) ions (**Figure 5.5, A**), bound to an η^4-Cb^{trans} ligand with Dy-Cb$_{Cg}$ = 2.3094(5) Å. Each centre has two κ^2-HBBN ancillary ligands, a terminal (symmetric) HBBN showing Dy-B$_{HBBN}$ = 2.567(5) Å and a γ-agostic CH$^{\cdots}$Dy interaction Dy-H$_{CH}$ = 2.781(49) Å *via* a bridgehead proton, and a potassium-bridging (asymmetric) HBBN with noticeably longer Dy-B$_{HBBN}$ = 2.741(5) Å; all of which are consistent with previous reports. Finally, the coordination sphere is complete with a solvated THF molecule Dy-O$_{THF}$ = 2.367(3) Å. The potassium counter-cations are coordinated to the opposite face of each cyclobutadienediide ring with K-Cb$_{cg}$ = 2.7401 Å, and interestingly have no coordinated solvent. Instead, they appears to be coordinatively satisfied by a number of short contacts (**Figure 5.5**, **B**): Si-Me$^{\cdots}$K interactions with the two *trans* SiMe$_3$ groups of the coordinated Cb ring between 2.756(64) - 3.199(54) Å, cation-π interactions with the ipso and ortho carbons of the nearest Cb ring's phenyl substituent K-C$_{ipso}$ = 3.302(4) Å, K-C$_{ortho}$ = 3.480(4) Å, further cation-π interactions with the para and meta substituents of a neighbouring Cb ring's phenyl substituents K-C$_{para}$ = 3.126(5) Å, K-C$_{meta}$ = 3.169(5) Å, and finally CH$^{\cdots}$K interactions with the bridgehead and methylene protons of a nearby HBBN unit of K-H$_{CH}$ = 2.754(50) Å, K-H$_{CH2}$ = 2.755(52) Å and K-HCH2 = 2.737(39) Å respectively. The potassium and dysprosium ions make an angle of ∠K-Cb$_{cg}$-Dy = 175.56(2)^o with the centroid of the Cb ring.

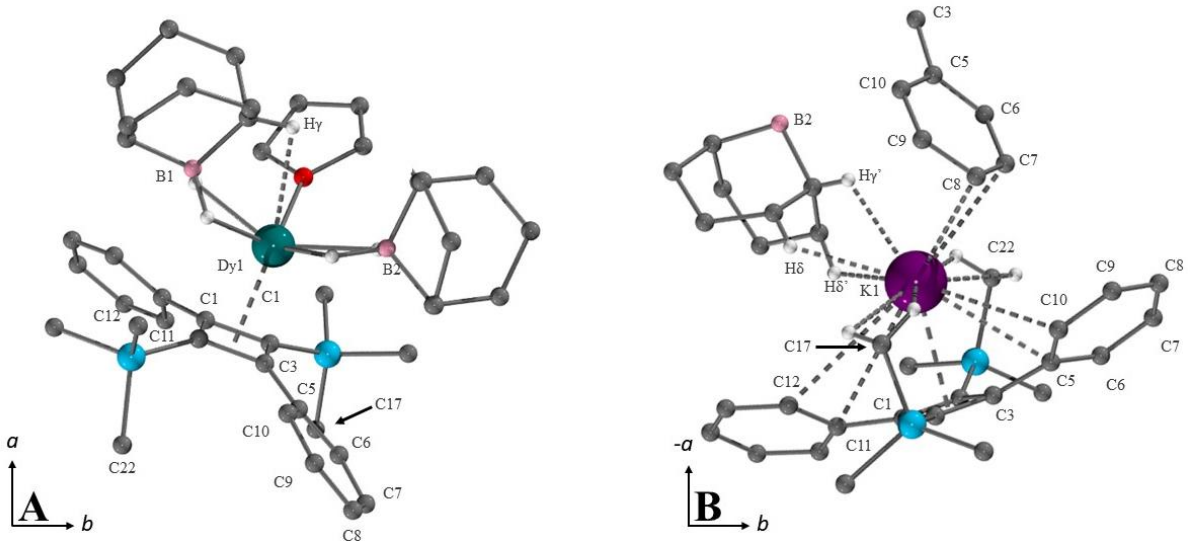

Figure 5.5 - Partial solid-state molecular structure of compound **5.3** [Dy(HBBN)$_2$(THF)(μ-Cb^{trans})K(THF)], displaying the Dy (**A**) and K (**B**) ions' coordination spheres. Atoms wree rendered as ball-and-sticks and non-coordinating hydrogen atoms were removed for clarity. Colour code: dysprosium, teal; lithium, violet; oxygen, red; carbon, grey; boron, pink; silicon, aqua. Non-interacting hydrogen atoms and lattice solvent molecules were removed for clarity.

Table 5.3 - Selected interatomic distances in compound **5.3** [Dy(HBBN)$_2$(THF)(μ-Cb^{trans})K(THF)]·4(C6H6)**.**

Label	**Distance (Å)**	**Label**	**Distance (Å) / Angle(º)**
Dy-Cb$_{cg}$	2.3094(5)	K1-C10	3.480(4)
Dy-B1	2.567(5)	K1-C11	3.360(4)
Dy-B2	2.741(5)	K1-C12	3.741(1)
Dy-Hγ	2.781(49)	K-C22	3.345(6)
Dy-O1	2.367(3)	K-C17	3.249(7)
K1-Cb$_{cg}$	2.740(1)	K1-Hγ'	2.737(39)
K1-C5	3.302(4)	K1-Hδ	2.754(48)
K1-C7	3.169(5)	K1-Hδ'	2.755(52)
K1-C8	3.126(5)	K-Cb$_{cg}$-Dy	175.56(2)

The crystallographically equivalent atoms in **5.3** are related *via* a four-fold screw axis (4_2) which lies on the centroid of the wheel structure (**Figure 5.6**). The four dysprosium ions lie on the corners of a distorted square on the periphery of the ring structure, with length Dy-Dy$_{intra}$ = 11.460(1) Å, diagonal Dy-Dy$_{diag}$ = 16.102(1) Å, and ∠Dy-Dy-Dy internal angle of 89.261(5)º. The four potassium ions similarly lie on the corners of a distorted square, here in

the centre of the ring structure with length K-K_{intra} = 7.284(2) Å, K-K_{diag} diagonal = 10.128(2) Å, and ∠K-K-K internal angle of 88.09(2)°.

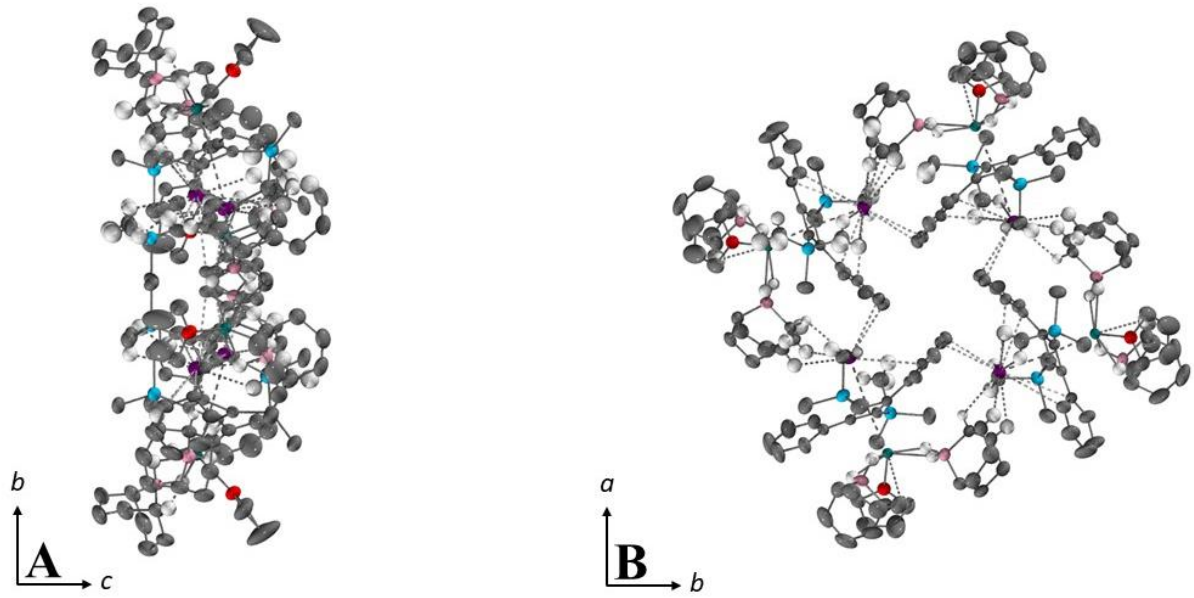

Figure 5.6 - Solid-state molecular structure of compound **5.3** [Dy(HBBN)$_2$(THF)(μ-Cb^{trans})K(THF)] viewed down *a* (**A**) and *c* (**B**) crystallographic axes. Thermal elipsoids were rendered at the 30 % probability level. Non-coordinating hydrogen atoms were removed for clarity. Colour code: dysprosium, teal; lithium, violet; oxygen, red; carbon, grey; boron, pink; silicon, aqua.

To analyse the packing of the tetramer units within the crystalline lattice, a Hirshfeld surface plot mapping d_{norm} for **5.3** were generated using CrystalExplorer21 and is displayed in **Figure 5.7**. Red areas on the d_{norm} surface indicate close-contacts, defined as when the weighted interatomic distance is shorter than the sum of the respective atoms' van der Waal radii. White regions indicate that the interatomic distance is at or around the sum of the van der Waal radii, and blue regions are where the interatomic distance is longer than the sum of the van der Waal radii. Looking at the d_{orrm} surface, we can see almost no close contacts from outside of the tetramer unit. The top and bottom faces show noticeably long contacts above the centroid of the tetramer, which can be understood by inspecting the crystallographic packing (*vide infra*). From the lack of short contacts, we can confirm that **5.3** does in fact form discrete tetrameric units.

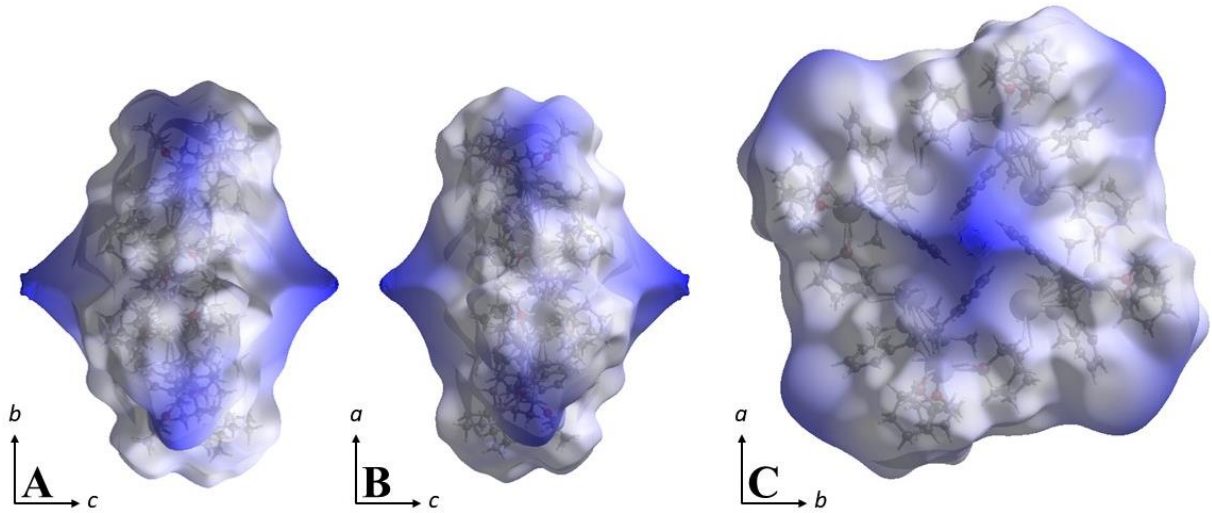

Figure 5.7 - Hirshfeld Surface plots of intermolecular interactions in compound **5.2** [Dy(HBBN)$_2$(THF)(μ-Cb^{trans})K(THF)] viewed down the *a* (**A**), *b* (**B**), and *c* (**C**) crystallographic axes. Atom colour code: dysprosium, teal; lithium, violet; oxygen, red; carbon, grey; boron, pink; silicon, aqua. Non-interacting hydrogen atoms were removed for clarity. Surface colour code: White, interatomic distance equal to sum of vdW radii; blue, interatomic distance greater than sum of vdW radii.

To analyse the types of interactions occurring, a fingerprint plot was created by generating a 2D histogram of interactions by their atomic distances **(Figure 5.7, A)**. The high symmetry and narrow plot confirm that intermolecular contacts are weak, likely because of the discrete tetrameric units packing in the unit cell. By breaking down the contributions by donor and acceptor atom identity we can observe that most of the close interatomic contacts are between protons, with H···H interactions dominating between 1.2 – 2.0 Å and C···H interactions taking place between 1.8 – 2.2 Å. Comparing the frequency of interactions as a percentage of total interactions (**Figure 5.7 B**), we can see that H···H interactions dominate, making up over 99 % of all total contacts. C···H and H···C interactions are the second most frequent, up less than 1 % of all interactions on the surface. Finally, C···C type are not observed. We would expect to see a red centroid around the vdW radius of carbon (1.8 Å) if significant π - π stacking was present, which we do not observe.

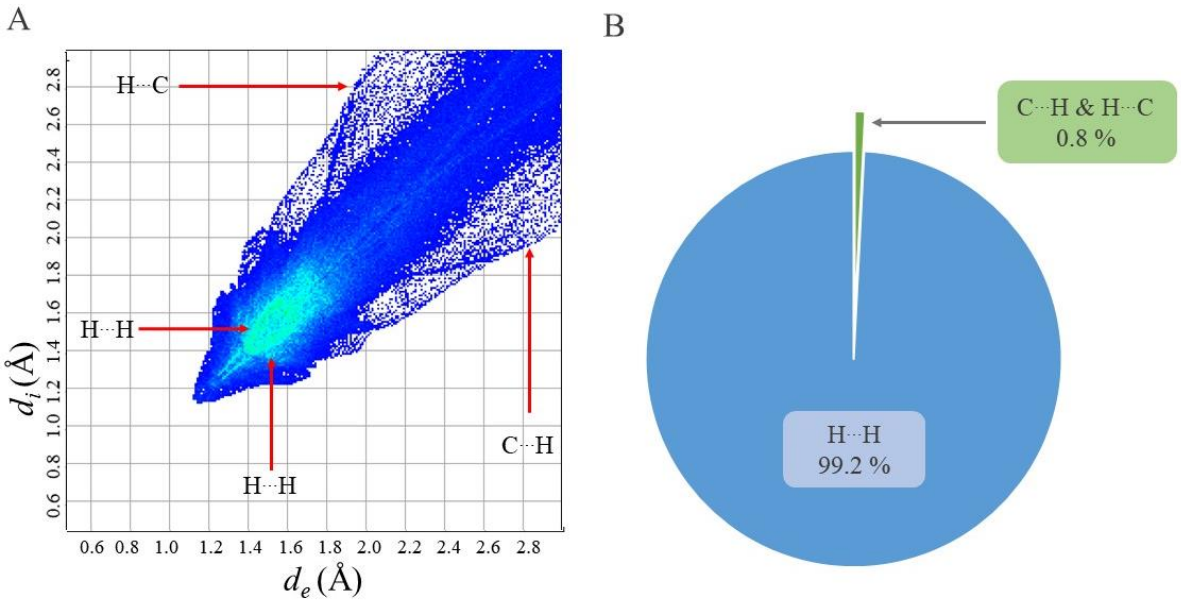

Figure 5.8 - Fingerprint plot of compound **5.3** [Dy(HBBN)$_2$(THF)(μ-Cb^{trans})K(THF)] showing the contacts as a function of distance (d_i and d_e) and frequency (**A**). Colour code: blue, least common; green, moderately common. (**B**) Pie chart showing interaction groups' frequency as a percentage of total interactions. Generated using CrystalExplorer21.

Finally, we can corroborate these results by analysing the crystallographic packing in 3.1 (**Figure 5.9**). We can see that the tetramer unit packs in sheets parallel to the plane of the ring, creating a distinct zig-zag packing motif in the lattice. Neighbouring tetramers are separated by C_g-C_g' 24.786(2) A between their centroids, and the planes are separated by 15.3318(2) A, which is in agreement with the paucity of intermolecular contacts described in the fingerprint plot.

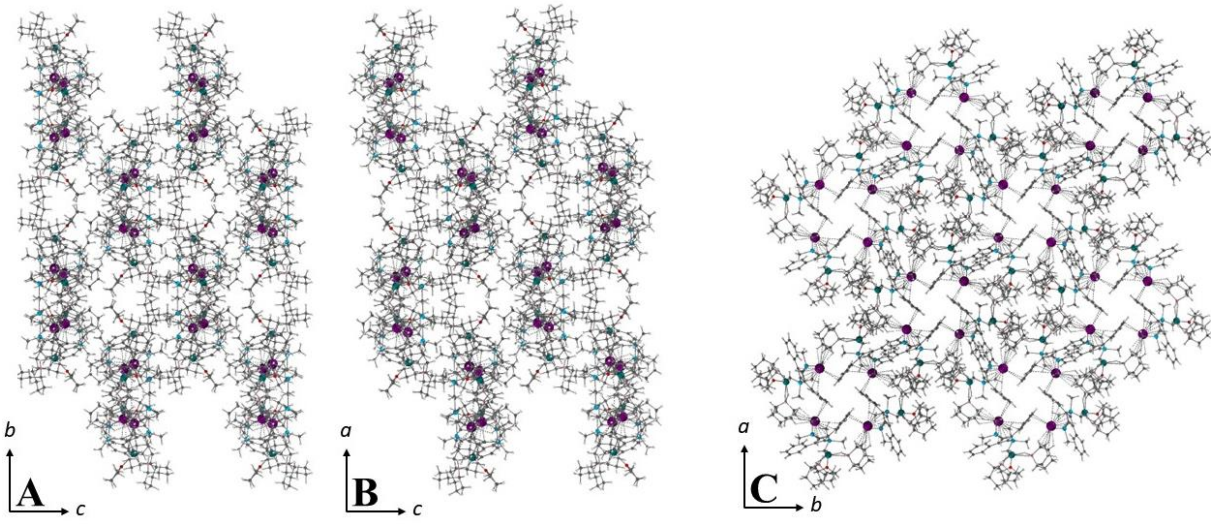

Figure 5.9 - Solid-state crystal packing of compound **5.3** [Dy(HBBN)$_2$(THF)(μ-Cb*trans*)K(THF)] down the *a* (**A**), *b* (**B**), and *c* (**C**) crystallographic axes. Thermal ellipsoids were rendered at the 30 % probability level. Non-coordinating hydrogens were removed for clarity. Colour code: dysprosium, teal; lithium, violet; oxygen, red; carbon, grey; boron, pink; silicon, aqua.

Discrete multinuclear dysprosium complexes have been highlighted by us and others as potential building blocks for spintronic and data storage applications. The tuneable nuclearity, from mono to tetranuclear complexes on changing from a lithium to potassium counterion, warrants further investigation. Investigations into larger Alkali metal cations, such as Rubidium or Caesium, and their effect on the complex nuclearity would provide valuable insight into the formation of cyclobutadienediide complexes.

Further characterisation of the compounds described was attempted using FTIR spectroscopy, however the extreme air and moisture sensitivity precluded the collection of clear data.

Further test reactions were carried out using the [Li_2Cb^{cis}] isomer described in chapter **4**, however no crystalline material was obtained.

5.3 Summary:

In this chapter we present the isolation of the first Ln(III) HBBN salt and investigated its reactivity with lithium cyclobutadienediide. Utilising these bulky co-ligands, we isolate for the first time a discrete cyclobutadienediide complex, verifying our design strategy. Additionally, we observed the formation of a distinct tetranuclear complex, bridged by potassium ions. These results demonstrate that careful choice of organometallic co-ligands allows for the development of discrete Cyclobutadienediide complexes for the first time and provides insight into the reactivity of the Cb^{trans} ligand.

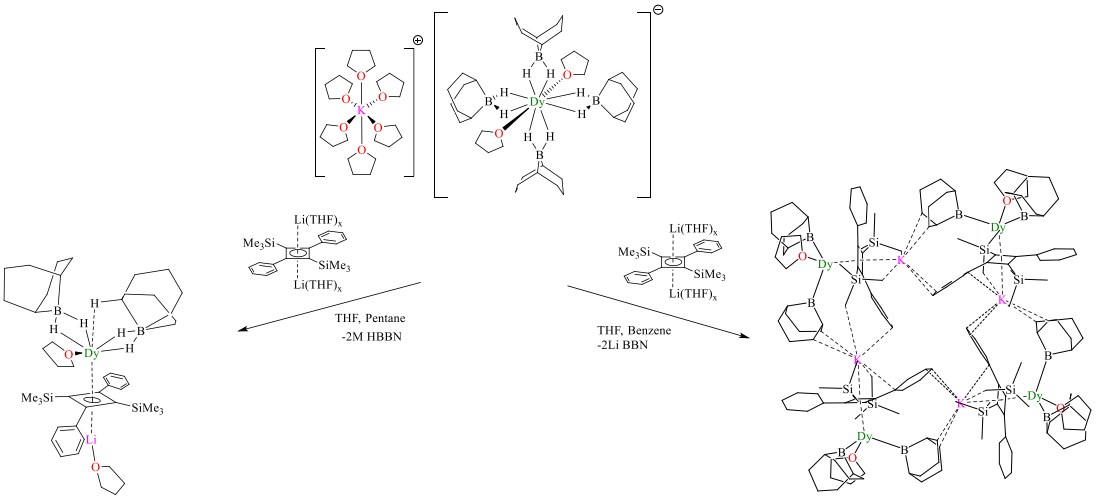

Scheme 5.4 - Synthetic scheme summarising reactions described in chapter 5.

5.4 Experimental:
Materials and methods

Caution: elemental alkali metals are extremely pyrophoric and should be handled with care.

All reactions and subsequent manipulations were performed under air-free and anhydrous conditions using standard Schlenk-line or nitrogen atmosphere glovebox techniques. Tetrahydrofuran, Toluene, Benzene, Hexanes, and pentane solvents were dried on columns of activated alumina using a J.C. Mayer solvent purification system, degassed with successive freeze-pump-thaw cycles, and stored over 4 Å molecular sieves in a nitrogen atmosphere glovebox prior to use. Celite® used for filtration was dried under vacuum while heating at 200 °C for 120 h, subsequently cooled under vacuum, and stored under nitrogen before use. 4 Å molecular sieves were activated by heating to 200 ºC under high vacuum for a week, slowly cooling to room temperature, and stored in a nitrogen atmosphere glovebox before use. 9-BBN dimer was purchased from Sigma Aldrich, degassed with successive freeze-pump-thaw cycles, and stored over 4 Å molecular sieves in a nitrogen atmosphere glovebox prior to use. [Li_2Cb^{trans}] was prepared as described in **Chapter 4**. Anhydrous $DyCl_3$ and YCl_3 were purchased from Strem Chemicals Inc at 99% purity and stored in a nitrogen atmosphere glovebox without further purification. Potassium hydride in a mineral oil suspension was purchased from Sigma Aldrich, washed thoroughly with hexanes, dried *in vacuo*, and stored under nitrogen prior to use.

Single-Crystal X-ray measurements: Full data was collected on a Bruker AXS SMART APEX-II CCD single-crystal diffractometer (graphite monochromated Mo-Kα radiation, λ = 0.71073 Å), at 200 K temperature. Absorption corrections were applied by using multi-scan of the SADABS[1] program. Structures were solved using direct methods with SHELXT[2] and refined by the full-matrix least-squares methods on F^2 with SHELXL-2018/3[3] in anisotropic approximation for all non-hydrogen atoms. Carbon-bound hydrogen atoms were included in calculated positions.

Synthesis of [K(THF)xHBBN]:

KHBBN was prepared using a modified literature method:[17]

To a -30 ºC rapidly stirred suspension of 2.1 g (51 mM) KH in 50 mL THF was added 5.0 g (20.5 mM) 9-BBN dimer diluted in 50 mL THF dropwise *via* cannula. The translucent suspension was allowed to warm to room temperature and stirred overnight. After allowing to settle, the off-white solution was filtered over Celite® and dried *in vacuo* to yield 4.5 g (27 mM 65 %) of KHBBN as an off-white powder.

Synthesis of $[K(THF)_6][Dy(HBBN)_4(THF)_2]$ 5.1:

30 mL of -30 ºC THF was added to a cooled Schlenk flask charged with 1.0 g (3.66 mM) $DyCl_3$ and 2.37 g (14.65 mM) KHBBN and a magnetic stir bar. The resulting suspension was allowed to heat to room temperature with stirring over an hour. Once at room temperature, the pale-yellow suspension was heated to 60 ºC and stirred for 72 hours. The resulting pale-yellow suspension was filtered through Celite®, which was washed with 3x mL THF. The

pale yellow solution was then concentrated to half volume and cooled to -27 ^{o}C to 2.4 g (2.17 mM, 61 %) of [K(THF)$_6$][Dy(HBBN)$_4$(THF)$_2$] as pale yellow needle crystals.

Synthesis of [Dy(κ^3-HBBN)(κ^2-HBBN)(THF)((μ-Cb^{trans})Li(THF)] 5.2:

A deep red solution of 50 mg (0.098 mM) [Li$_2$Cb^{trans}] in 5 mL benzene was added dropwise over five minutes to a stirred solution of 200 mg (0.196 mM) **5.1** in 5 mL benzene. The resulting orange suspension was stirred for 18 hours at room temperature, after which it was filtered through Celite®, and dried *in vacuo* to yield a tacky orange oil. Extracting this oil with 3 x mL hexanes yields a pale red solution that was cooled to -27 ^{o}C overnight to yield 10 mg red block crystals of **5.2**.

Synthesis of [Dy(κ^3-HBBN)(κ^2-HBBN)(THF)(μ-Cb^{trans})K(THF)]$_4$ 5.3:

After washing the crude product described in **5.2** with hexanes, the orange oil was washed with a further 3x mL benzene, which was filtered through Celite® to yield a deep red oil. Slow diffusion of room temperature pentanes into this solution yielded 15 mg red crystals of **5.3** after one week.

5.5 References:

1 M. Moore, S. Gambarotta and C. Bensimon, *Organometallics*, 1997, **16**, 1086–1088.

2 T. J. Woodman, M. Schormann, D. L. Hughes and M. Bochmann, *Organometallics*, 2003, **22**, 3028–3030.

3 C. E. Anson, W. Klopper, J. S. Li, L. Ponikiewski and A. Rothenberger, *Chem. Eur. J.*, 2006, **12**, 2032–2038.

4 G. R. Whittell, M. D. Hager, U. S. Schubert and I. Manners, *Nat. Mater.*, 2011, **10**, 176–188.

5 D. Errulat, B. Gabidullin, A. Mansikkamaki, and M. Murugesu, *Chem. Comm*., 2020, 56, 5937-5940.

6 P. Evans, D. Reta, C. A. P. Goodwin, F. Ortu, N. F. Chilton and D. P. Mills, *Chem. Commun.*, 2020, **56**, 5677–5680.

7 E. Clot and O. Eisenstein, in *Principles and Applications of Density Functional Theory in Inorganic Chemistry I*, eds. N. Kaltsoyannis and J. E. McGrady, Springer, Berlin, Heidelberg, 113th edn., 2004, pp. 1–36.

8 F. Feil, *Organometallics*, 2000, **19**, 5010–5015.

9 C. Eaborn, K. Izod and J. D. Smith, *J. Organomet. Chem.*, 1995, **500**, 89–99.

10 S. C. Roşca, E. Caytan, V. Dorcet, T. Roisnel, J. F. Carpentier and Y. Sarazin, *Organometallics*, 2017, **36**, 1269–1277.

11 G. B. Deacon, P. C. Junk and G. J. Moxey, *Chem. Asian J.*, 2009, **4**, 1309–1317.

12 M. F. Zuniga, G. B. Deacon and K. Ruhlandt-Senge, *Inorg. Chem.*, 2008, **47**, 4669–4681.

13 A. S. Novikov,*Crystals*, 2020, 10, 537, 8–11.

14 M. Morimoto, S. M. Bierschenk, K. T. Xia, R. G. Bergman, K. N. Raymond and F. D. Toste, *Nat. Catal.*, 2020, **3**, 969–984.

15 X. Chen, S. Lim, C. E. Plečnik, S. Liu, B. Du, E. A. Meyers and S. G. Shore, *Inorg. Chem.*, 2005, **44**, 6052–6061.

16 A. Sekiguchi, T. Matsuo and M. Tanaka, *Organometallics*, 2002, **21**, 1072–1076.

17 X. Chen, S. Liu, B. Du, E. A. Meyers and S. G. Shore, *Eur. J. Inorg. Chem.*, 2007, 5563–5570.

Chapter 6: Future Work and Perspectives

6.1 Multinuclear SMMs:

A long-standing goal in the molecular magnetism community has been the development of high-performance multinuclear Lanthanide SMMs. Systems with magnetic communication show stronger resistance to QTM and have been proposed as building blocks for spintronic systems. These can also offer valuable fundamental insights into the nature of bonding and exchange coupling interactions. We previously reported the use of Lanthanide COT complexes to build "multidecker" metallocenes as building blocks for high-nuclearity SMMs (**Scheme 6.1**).[1,2]

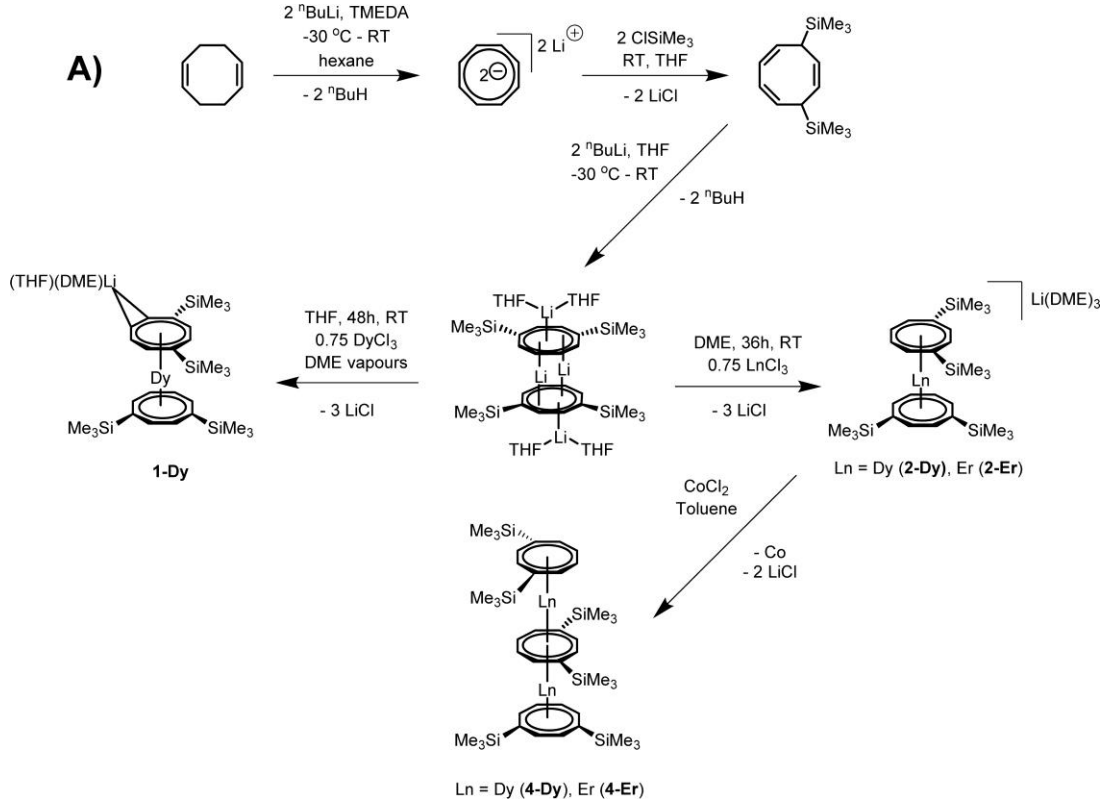

Scheme 6.1 - Synthetic scheme describing the preparation of Er COT multidecker sandwich complexes. Adapted from **ref. 1** with permission.

While COT based systems have given a number of valuable insights, they are fundamentally limited in their magnetic performance, as these ligands have been demonstrated to stabilise the prolate Lanthanide (III) ions, such as erbium (III), which have been recently shown *via ab initio* studies to be more susceptible to through-barrier relaxation as a result of strong transverse CF terms in their excited states.[3] As a result, SMMs based on prolate ions are unable to possess the same multistep, high energy barrier relaxation pathways seen in oblate ions like dysprosium (III) systems.[4] Indeed, for the development of high-performance multinuclear SMMs, dysprosium (III) ions appear to be the best candidates, and to this end, multi-decker cyclobutadienediide complexes are a promising target (**Scheme 6.2**).

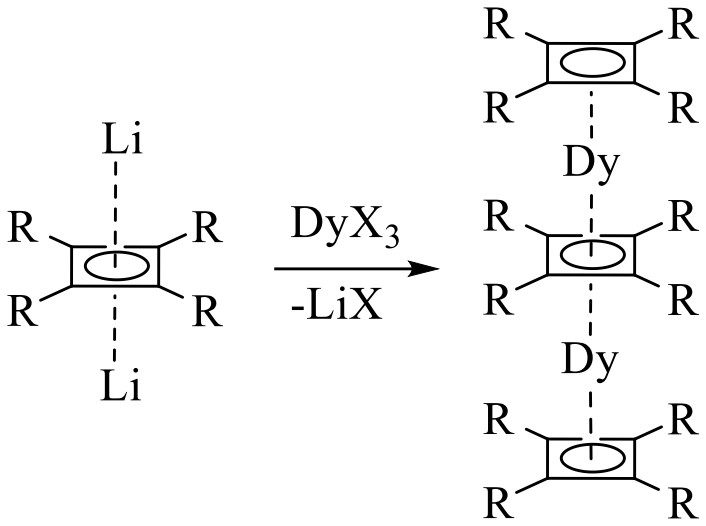

Scheme 6.2 - Synthetic scheme describing synthesis of a hypothetical multinuclear dysprosium (III) Cyclobutadienediide metallocene as a high-performing SMM.

To investigate the synthesis of Cb^{cis} and Cb^{trans} metallocenes, test reactions utilising the respective lithium salts and dysprosium chloride were investigated. Refluxing a deep red suspension of dysprosium Chloride and [Li_2Cb^{trans}] in benzene overnight yielded a deep-orange solution. Filtration of this solution through a pad of Celite® and concentration *in vacuo* yielded a deep orange oil. The orange oil was insoluble in hexanes and formed a deep-red solution in benzene. Multiple crystallisation routes were investigated; however, no crystalline material was obtained.

We explored the use of DyF_3 in place of $DyCl_3$, on the basis that the hard F^- counterion would provide a stronger driving force for the precipitation of LiX salts. A suspension of DyF_3 in THF and [Li_2Cb] was sonicated overnight in a Schlenk flask, however the extreme insolubility of DyF_3 lead only to intractable brown oils upon workup.

We employed triflate ($CF_3SO_3^-$) salts as an alternative to Fluoride, as they provide a strong driving force for metathesis yet maintain good solubility.[5] Anhydrous dysprosium triflate can be prepared by refluxing dysprosium oxide in an aqueous solution of triflic acid, before recrystallising from acetone and drying *in vacuo* at 220 ºC for 48 hours.[6] With anhydrous dysprosium triflate in hand, we explored its reactivity with lithium Cb. A deep red solution of [Li_2Cb] in THF was added dropwise to a pale-yellow stirred solution of [$Dy(Otf)_3$] in THF. The pale orange solution was stirred at room temperature overnight, after which it was filtered through Celite® and dried *in vacuo* to yield a deep red oil. Extraction of this oil into benzene and filtration through Celite® yielded a deep red solution. Diffusion of pentanes at room temperature yielded deep red needle crystals after one week, however their extreme air and moisture sensitivity has precluded characterisation thus far.

6.2 Sodium and potassium Salts of Cb:

As described in Chapters 1 and 4, Sekiguchi's elegant lithium-mediated reductive transmetallation route is the only known method to prepare Cb salts from TM-Cb complexes and is used in the preparation of sodium and potassium salts of Cb'''' (**Scheme 6.3**).[7] By oxidising the dilithio salt with a strong oxidant, such as a dihaloalkane, the naked cyclobutadiene moiety can reportedly be isolated by purification from the resultant LiX

salts.[8] The stability of metal-free neutral Cb species however is not well studied, and these species are known to undergo rapid Diels-Alder cyclisation in solution to reach thermodynamically stable aromatic electronic configurations.[9–14] The neutral Cb'''' can reportedly be purified in the solid state *via* vacuum sublimation, allowing the unstable species to be isolated.

Further reduction of the neutral cyclobutadiene with heavier Alkali or Alkaline Earth Metals allows access to a range of [M_nCb''''] salts (M = Li, Na, K n = 2; M = Mg, Ca, n = 1).[8] By changing counter-cation from lithium to potassium, which is larger and softer, we would expect to have a stronger driving force for metathesis reactions with metal salts. Indeed, for this reason potassium salts are the most often used ligand transfer reagents employed in organometallic chemistry.[15,16]

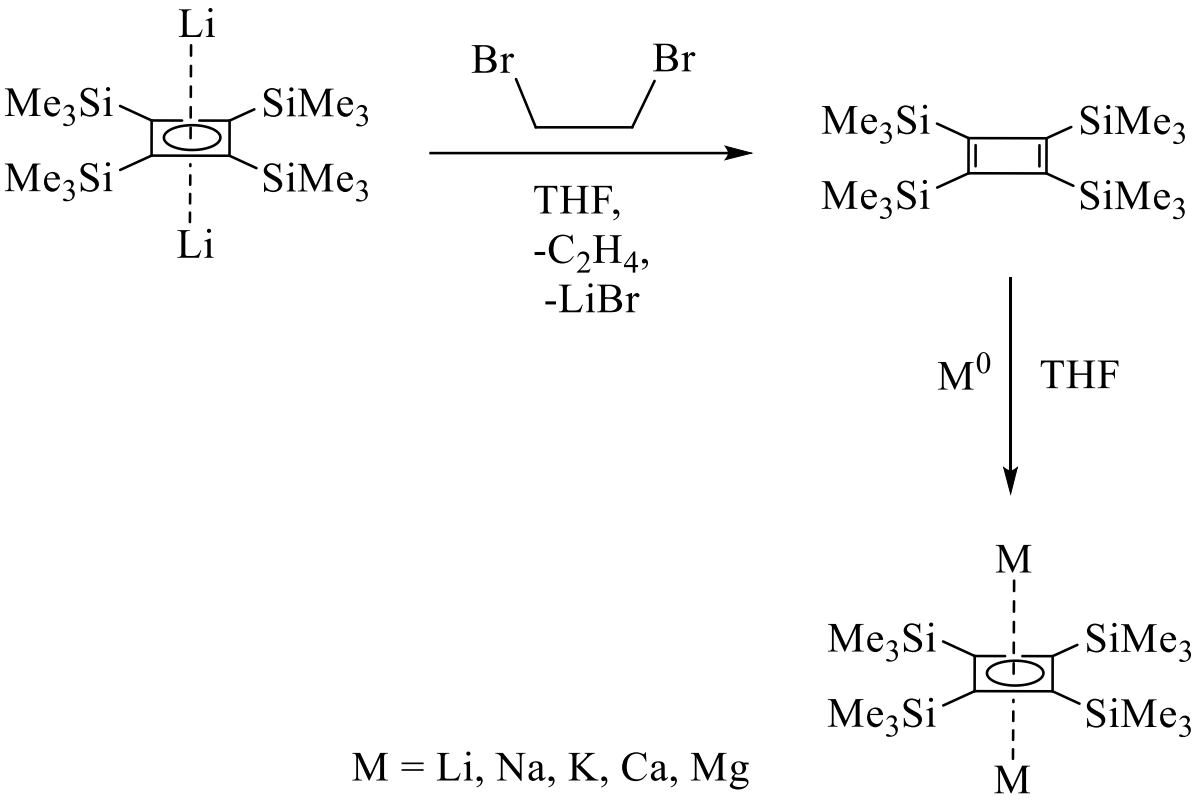

Scheme 6.3 - Synthetic scheme showing the only published route to [M_nCb] salts (M = Li, Na, K, Mg, Ca), described by Sekiguchi and co-workers. Oxidation of [Li_2Cb''''] with dibromoethane in THF. Note: this reaction is said to be completed after 2 minutes and then immediately dried *in vacuo*, highlighting the extremely poor stability of the neutral cyclobutadiene in solution. After purification via vacuum sublimation, the neutral cyclobutadiene is then reduced chemically via Alkali or Alkaline Earth Metal reductants and crystallised from Hexanes.

To this end, oxidation of [Li_2Cb^{trans}] was explored by adding a solution of 1,2-dibromoethane in THF to a rapidly stirred solution of [Li_2Cb^{trans}] in THF. Upon addition, the deep-red solution became translucent black almost immediately. After stirring for one minute, the THF solution was dried *in vacuo* to yield a tacky black oil which was taken up in hexanes, filtered through Celite®, and dried to a purple solid. Attempted reactions of this solid with

alkali metal reducing agents, such as sodium or potassium metal, were unsuccessful. ^{13}C NMR of the black powder in benzene showed no product peaks.

Until the chemistry of the cyclobutadiene dianion is further developed, the lithium-mediated reductive transmetallation and subsequent oxidation and reduction is the only known entry point to cyclobutadienediide organometallic chemistry. The development of NaCb and KCb salts may prove insights to the fundamental reactivity and stability of Cb systems.

6.3 Structure-activity relationships with Cb^{cis} and Cb^{trans} metallocenes

In the experiments described within this and the previous two chapters, we have reported structurally authenticated examples of Cb^{trans} only. Our reactions carried out in parallel utilising [LiCb^{cis}] qualitatively appeared to have caused a transformation, yet in all cases no crystalline material was formed. We tentatively suggest that, as the dianionic charge is expected to be delocalised over the two phenyl groups in Cb^{cis} and Cb^{trans}, we would expect Cb^{cis} complexes to be less stable due to the coulombic repulsion between the two aryl ligands.[17] If the Cb^{cis} moiety can be properly stabilised to isolate molecular complexes, then a comparison to the Cb^{trans} congener would offer a fascinating structure-property relationship between the two systems (**Scheme 6.4**). We would expect the two different local symmetries experienced by each ligand to have a significant effect on the orbital overlap in these complexes. Additionally, we would expect the differing bond-polarisations and electronic repulsions to lead to vastly different CF environments.[18] In this sense, cyclobutadienediides prepared from asymmetric acetylenes, such as Cb^{cis} and Cb^{trans}, may offer a route to novel magneto-structural correlations in high performance Lanthanide SMMs, which has been highlighted in advancing the frontier of this field.[19–22]

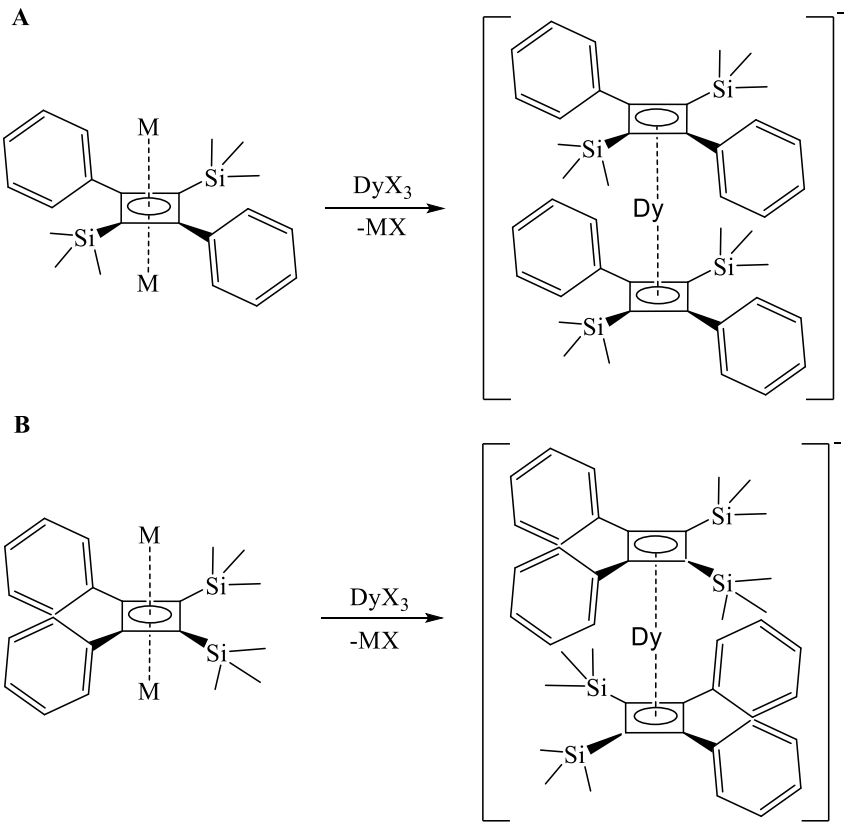

Scheme 6.4 - Synthetic scheme describing the synthesis of proposed $[DyCb^{trans}_2]^-$ (**A**) and $[DyCb^{cis}_2]^-$ (**B**) homoleptic metallocenes.

6.4 More Complex Cb Dianion Systems:

To the best of our knowledge, only the organometallic chemistry of the Cb*''''*, and now $Cb^{trans,}$ dianions have been explored. Fundamental understanding of this organometallic chemistry may be found by investigating Cb dianions with alternative frameworks. Due to the detailed investigations of Cb synthesis in the 20th century, a number of other candidate frameworks exist in the literature: the heavy Cb analogue, the tetrakis(di-*tert*-butylmethylsilyl)-1,2,3,4-tetrasilacyclobutadiene dianion (**Figure 6.1, A)** was reported by Sekiguchi and co-workers as a 6 πe aromatic dipotassium salt.[23] Investigations into its reactivity have yielded structurally-authenticated organometallic complexes of cobalt, Iron, and Ruthenium but no main group or f block metals.[24–28] It would appear therefore that the 4 and 5f organometallic chemistry of the cyclobutadienediides could gain great insight from the bonding in these non-traditional ligands; next, tetrakis(*tert*-butyl)cyclobutadiene (**Figure 6.1, B**) can be prepared by coupling bis(*iso*-propyl)acetylenes with cobalt Cp carbonyl utilising Nakamura and Higihara's method. Bulky alkyl groups are preferrable to silyl groups in organometallic SMM chemistry, as the C-Si bond is strongly polarised and can have a destabilising effect on the magnetisation axis, as highlighted in *ab initio* studies of $[Dy_2[COT'']_3]$ (**Scheme 6.1**)[1,29–31] The tetrakis(*tert*-butyl)cyclobutadienediide dianion could therefore act as an analogue to the Cp^R (R = ^{I}pr, ^{t}bu, Me) ligands used to prepare the record breaking Dysprosocenium class of SMMs (*vide infra*). No structurally authenticated alkyl-substituted cyclobutadienediide have been reported, though computational investigations have predicted that they can be stabilised by metal coordination;[12] Finally, a proposed heterocycle-substituted cyclobutadiene dianion, tetrakis(3-pyridyl)cyclobutadienediide

(**Figure 6.1, C)**. Several TM cyclobutadiene complexes with heterocyclic substituents have been reported, utilising Nakamura and Higihara's method to couple bis-aryl acetylenes with low-valent TMs,[32–34] though no investigation into these dianions has been conducted. The appeal of heterocyclic substituents is the possibility to design bifunctional linkers that can be utilised to prepare multinuclear systems. This was demonstrated by Brisbois and Greico, who reported barrel-shaped molecular cages comprising [CoCb^{pyr4}Cp] (Cb^{pyr4} = 1,2,3,4,-tetrakis(3-pyridyl)cyclobutadiene) nodes and [Pd(en)] (en = ethylenediamine) linker units, charge-balanced by nitrate anions within the lattice.[35] Through this methodology, we can envision a route to develop multinuclear SMM systems based on the Cb dianion while avoiding over-functionalisation of the metal centre, which leads to loss of point group symmetry and introduction of unwanted CF interactions.[36–38]

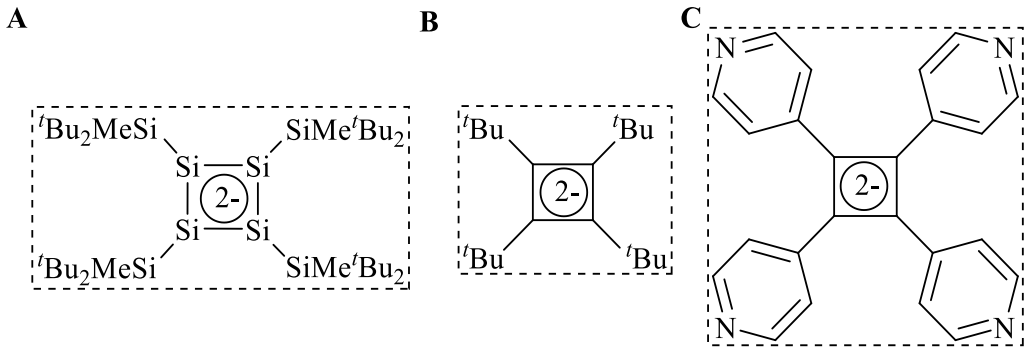

Figure 6.1 - Schematic representations of three cyclobutadiene moieties with unexplored organometallic chemistry. *tetrakis*(di-tert-butylmethylsilyl)-1,2,3,4-tetrasilacyclobutadiene dianion (**A**), tetrakis(*tert*-butyl)cyclobutadienediide (**B**), tetrakis(3-pyridyl)cyclobutadienediide (**C**).

It is clear therefore that the organometallic chemistry of the cyclobutadiene dianion is only now beginning in earnest, and that many interesting systems are within reach that may provide valuable insight into organometallic chemistry as a whole, as well as in the development of high-performance SMMs.

6.5 Functionalising Palladocene

The discovery of Ferrocene is said to be the revolution that modernised organometallic chemistry. Its exceptional stability, as a result of its stable 18*e* configuration and strongly bound aromatic cyclopentadieneide ligands. The discovery of the neutral palladium complex **3.1** is interesting in this context, as the neutral 4π cyclobutadiene ligand appears to be uniquely suited to preparing neutral low-valent group 10 organometallic complexes with 18 electrons, as the synergistic bonding and Dewar-Chatt-Duncanson backbonding stabilises both the antiaromatic ring and the reactive metal centre.[11,39,40] In light of this, complex **3.1** may be considered as a prototypical *Palladocene*. One of the most interesting aspects of Ferrocene's organometallic chemistry is its facile functionalisation *via* aromatic substitution reactions, such as acylations (**Scheme 6.5 A)**.[41–43] Ferrocene's robust chemical stability and functional group tolerance has led to its use in numerous diverse fields, from drug delivery[44], to charge-storage batteries[45] and solution-state electrochemistry[46], amongst others. No studies of the reactivity of cyclobutadiene metallocenes has been conducted,[47] however the reactivity of the mixed-sandwich [CoCbCp] system has been investigated, demonstrating that functionalisation of the Cb rings is comparable to ferrocene

(**Scheme 6.5 B**).[48] To this end, investigations into the reactivity of Palladocenes, such as towards acyl substitution (**Scheme 6.5 C**), could open the door to a new generation of Palladocene derivatives.

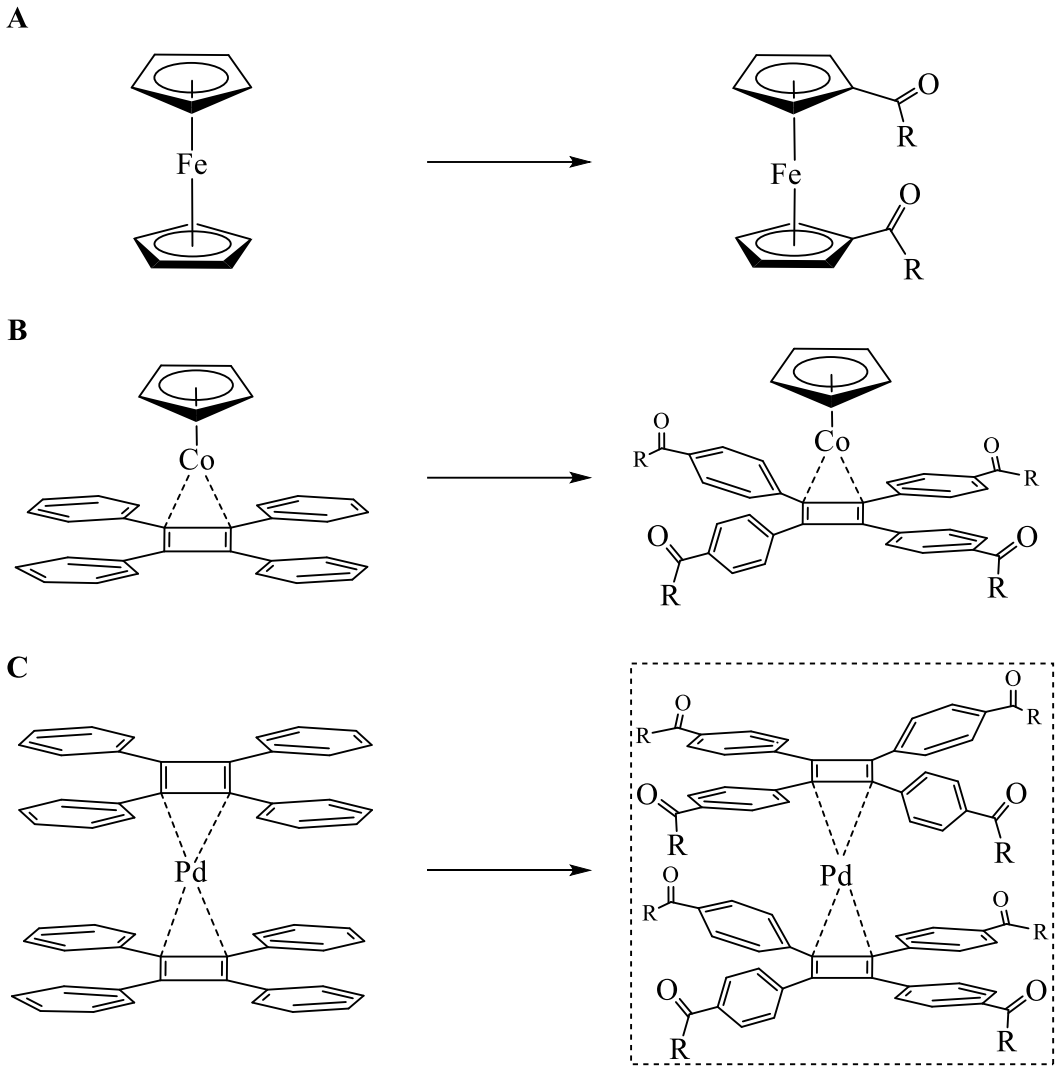

Scheme 6.5 - Synthetic scheme showing the acetylation of Ferrocene (**A**), cobalt cyclobutadiene cyclopentadieneide (**B**), and proposed reaction with Palladocene **3.1** (**C**).

6.6 Summary

In this chapter, we report investigations into Cb*trans* metallocenes and discuss attempts to isolate the neutral Cb*trans* species. We discuss past and present examples of cyclobutadiene complexes and show that the organometallic chemistry of the heavy main group, alkyl, or heterocyclic cyclobutadienediides is yet to be understood. Finally, we give perspective to the neutral palladium complex described in Chapter 3 and discuss its context with respect to Ferrocene, the archetypical organometallic complex, and its future studies.

6.7 Experimental

Materials and methods

Caution: elemental alkali metals are extremely pyrophoric and should be handled with care.

All reactions and subsequent manipulations were performed under air-free and anhydrous conditions using standard Schlenk-line or nitrogen atmosphere glovebox techniques. Tetrahydrofuran, Toluene, Benzene, Hexanes, and pentane solvents were dried on columns of activated alumina using a J.C. Mayer solvent purification system, degassed with successive freeze-pump-thaw cycles, and stored over 4 Å molecular sieves in a nitrogen atmosphere glovebox prior to use. Celite® used for filtration was dried under vacuum while heating at 200 °C for 120 h, subsequently cooled under vacuum, and stored under nitrogen before use. 4 A molecular sieves were activated by heating to 200 °C under high vacuum for a week, slowly cooling to room temperature, and stored in a nitrogen atmosphere glovebox before use. [Li_2Cb^{trans}] was prepared as described in **Chapter 4**. Anhydrous $DyCl_3$ and YCl_3 were purchased from Strem Chemicals Inc at 99% purity and stored in a nitrogen atmosphere glovebox without further purification.

Reaction between [Li_2Cb^{trans}] and [$DyCl_3$]:

To a rapidly stirred suspension of 51 mg (0.098 mM) $DyCl_3$ in 5 mL benzene was added 100 mg (0.197 mM) of Li_2Cb in 5 ml of benzene. The deep red solution was allowed to stir at room temperature for one hour, before heating to 80 °C for 16 hours. Once cool, the deep orange suspension was filtered through Celite® and dried *in vacuo* to yield 90 mg of tacky deep red oil insoluble in alkane solvents, soluble in aromatics and polar solvents. Attempted recrystallisation yielded no crystalline material.

Reaction between [Li_2Cb^{trans}] and [DyF_3]:

To a suspension of 22 mg (0.098 mM) DyF_3 in 5 mL THF was added 100 mg (0.197 mM) of [Li_2Cb^{trans}] in 5 ml of THF. The deep red suspension was sonicated overnight in a Schlenk flask at bath temperature of approximately 60°C to yield a brown suspension. After drying *in vacuo* and bringing inside a nitrogen atmosphere, the tacky brown oil was found to be insoluble in hexanes, benzene, and THF.

Preparation of anhydrous [$Dy(Otf)_3$]:

Anhydrous dysprosium Triflate was prepared via a modified literature route:[6]

A round bottom flask was charged with 10.0 g (26.88 mM) dysprosium oxide, 14 mL triflic acid (99 % triflic acid, 163 mM) in 14 mL water, a magnetic stir bar, and a condenser. The clear solution was refluxed at 100 °C for 16 hours, after which it had developed into an off-white turbid suspension. Filtration and drying *in vacuo* [$Dy(Otf)_3x(H_2O)$] as fluffy off-white powder. The powder was recrystallised by dissolving in minimal hot acetone (*ca.* 50 mL), hot filtering, and cooling to -5 °C overnight. The crystalline material was washed with cold acetone, transferred to a Schlenk flash with a heating mantle, and dried *in vacuo* at 220 °C for 48 hours to yield 12.97 g (21.3 mM, 81 %) of [$Dy(Otf)_3$] as a pale yellow powder.

Reaction between [Li_2Cb^{trans}] and [$Dy(Otf)_3$]:

To a suspension of 60 mg (0.098 mM) [$Dy(Otf)_3$] in 5 mL benzene was added 100 mg (0.197 mM [Li_2Cb^{trans}] in 5 mL benzene. Once addition was complete, the orange suspension was heated to reflux for 18 hours. After settling, the resultant red suspension was filtered through Celite® and dried *in vacuo* to 150 mg deep red oil, insoluble in alkane solvents, soluble in aromatics and polar solvents. Slow diffusion of pentane into a room temperature benzene solution of this powder yielded small deep red crystals after one week.

Oxidation of [Li_2Cb^{trans}] with Dibromoethane:

To a deep red solution of 50 mg (0.098 mM) of [Li_2Cb^{trans}] in 5 mL THF was added quickly 500 mg (2.96 mM) of dibromoethane in 2 mL THF. The red solution immediately became pale-violet then a deep opaque black. After 1 minute 5 mL of hexanes was added, and the suspension was filtered through Celite® and dried *in vacuo* to 30 mg of deep purple powder.

6.8 References

1 J. J. Le Roy, M. Jeletic, S. I. Gorelsky, I. Korobkov, L. Ungur, L. F. Chibotaru and M. Murugesu, *J. Am. Chem. Soc.*, 2013, **135**, 3502–3510.

2 K. L. M. Harriman and M. Murugesu, *Acc. Chem. Res.*, 2016, **49**, 1158–1167.

3 F. Lu, M. M. Ding, J. X. Li, B. L. Wang and Y. Q. Zhang, *Dalton Trans.*, 2020, **49**, 14576–14583.

4 L. Ungur and L. F. Chibotaru, *Inorg. Chem.*, 2016, **55**, 10043–10056.

5 N. E. Dixon, G. A. Lawrance, P. A. Lay, A. M. Sargeson and H. Taube, in *Inorganic Syntheses: Reagents for Transition Metal Complex and Organometallic Syntheses*, 1990, vol. 28, pp. 70–76.

6 D. Das and D. Seidel, *Encycl. Reagents Org. Synth.*, , DOI:10.1002/047084289x.rn01253.

7 A. Sekiguchi, M. Tanaka, T. Matsuo and H. Watanabe, *Angew. Chem. - Int. Ed.*, 2001, **40**, 1675–1677.

8 K. Takanashi, A. Inatomi, V. Y. Lee, M. Nakamoto, M. Ichinohe and A. Sekiguchi, *Eur. J. Inorg. Chem.*, 2008, 1752–1755.

9 C. Y. Lin and A. Krantz, *J. Chem. Soc. Chem. Commun.*, 1972, **0**, 1111–1112.

10 O. L. Chapman, C. L. Mcintosh and J. Pacansky, *J. Am. Chem. Soc.*, 1973, **614**, 614–617.

11 R. Pettit, *J. Organomet. Chem.*, 1975, **100**, 205–217.

12 M. Balci, M. L. McKee and P. von Ragué Schleyer, *J. Phys. Chem. A*, 2000, **104**, 1246–1255.

13 G. Ganguly, S. Pathak and A. Paul, *Phys. Chem. Chem. Phys.*, 2021, **23**, 16005–16012.

14 L. J. Karas and J. I.-C. Wu, *Antiaromatic compounds: a brief history, applications, and the many ways they escape antiaromaticity*, Elsevier Ltd., First Edit., 2021.

15 S. A. Johnson, J. J. Kiernicki, P. E. Fanwick and S. C. Bart, *Organometallics*, 2015, **34**, 2889–2895.

16 M. Schlosser, *Angew. Chem., Int. Ed.*, 1965, **4**, 362.

17 A. Sekiguchi, T. Matsuo and M. Tanaka, *Organometallics*, 2002, **21**, 1072–1076.

18 K. Randall McClain, C. A. Gould, K. Chakarawet, S. J. Teat, T. J. Groshens, J. R. Long and B. G. Harvey, *Chem. Sci.*, 2018, **9**, 8492–8503.

19 B. M. Day, F. S. Guo and R. A. Layfield, *Acc. Chem. Res.*, 2018, **51**, 1880–1889.

20 K. Randall McClain, C. A. Gould, K. Chakarawet, S. J. Teat, T. J. Groshens, J. R. Long and B. G. Harvey, *Chem. Sci.*, 2018, **9**, 8492–8503.

21 A. Castro-Alvarez, Y. Gil, L. Llanos and D. Aravena, *Inorg. Chem. Front.*, 2020, **7**, 2478–2486.

22 K. R. Meihaus, J. F. Corbey, M. Fang, J. W. Ziller, J. R. Long and W. J. Evans, *Inorg.*

Chem., 2014, **53**, 3099–3107.

23 V. Y. Lee, K. Takanashi, T. Matsuno, M. Ichinohe and A. Sekiguchi, *J. Am. Chem. Soc.*, 2004, **126**, 4758–4759.

24 V. Y. Lee, Y. Ito and A. Sekiguchi, *Russ. Chem. Bull.*, 2013, **62**, 2551–2553.

25 K. Takanashi, V. Y. Lee, M. Ichinohe and A. Sekiguchi, *Angew. Chem. - Int. Ed.*, 2006, **45**, 3269–3272.

26 V. Y. Lee, Y. Ito, H. Yasuda, K. Takanashi and A. Sekiguchi, *J. Am. Chem. Soc.*, 2011, **133**, 5103–5108.

27 K. Takanashi, V. Y. Lee, T. Matsuno, M. Ichinohe and A. Sekiguchi, *J. Am. Chem. Soc.*, 2005, **127**, 5768–5769.

28 V. Y. Lee and A. Sekiguchi, *Inorg. Chem.*, 2011, **50**, 12303–12314.

29 I. Haiduc and V. Popa, *Metal Complexes of pi-Ligands Containing Organosilicon Groups, Adv. Organomet. Chem.*, 1997, 15, 113-146.

30 J. T. M. Van Dijk, S. A. Steggerda, J. Lugtenburg and J. Cornelisse, *J. Phys. Org. Chem.*, 1999, **12**, 86–94.

31 M. Briganti, F. Santanni, L. Tesi, F. Totti, R. Sessoli and A. Lunghi, *J. Am. Chem. Soc.*, 2021, 143, 13633-13645.

32 D. C. Caskey, T. Yamamoto, C. Addicott, R. K. Shoemaker, J. Vacek, A. M. Hawkridge, D. C. Muddiman, G. S. Kottas, J. Michl, P. J. Stang, *J. Am. Chem. Soc.* 2008, 130, 7620–7628.

33 A. K. Wiegel, B. R. Rad, D. Herrmann and R. Wolf, *Zeitschrift fur Anorg. und Allg. Chemie*, 2015, **641**, 2065–2070.

34 B. Rezaei Rad, D. Herrmann, C. Lescop and R. Wolf, *J. Chem. Soc. Dalton Trans.*, 2014, **43**, 4247–4250.

35 S. C. Johannessen, R. G. Brisbois, J. P. Fischer, P. A. Greico and D. E. Counterman, *J. Am. Chem. Soc.*, 2001, **123**, 3818–3819.

36 J. D. Hilgar, M. G. Bernbeck and D. Rinehart, *J. Am. Chem. Soc.*, 2019, **141**, 1913–1917.

37 P. Evans, D. Reta, C. A. P. Goodwin, F. Ortu, N. F. Chilton and D. P. Mills, *Chem. Commun.*, 2020, **56**, 5677–5680.

38 D. Errulat, B. Gabidullin, A. Mansikkamaki and M. Murugesu, *Chem Comm*, 2020, **56**, 5937–5940.

39 B. E. Bursten, F. Richard, B. E. Bursten and R. F. Fenske, 1979, **18**, 1760–1765.

40 K. D. Warren and D. W. Clack, *J. Org. Chem.*, 1978, **161**, 55–58.

41 M. Vogel, M. Rausch and H. Rosenberg, *J. Org. Chem.*, 1957, **22**, 1016–1018.

42 K. Heinze and H. Lang, *Organometallics*, 2013, **32**, 5623–5625.

43 D. Astruc, *Eur. J. Inorg. Chem.*, 2017, **2017**, 6–29.

44 H. Gu, S. Mu, G. Qiu, X. Liu, L. Zhang, Y. Yuan and D. Astruc, *Coord. Chem. Rev.*, 2018, **364**, 51–85.

45 C. Orneias, J. Ruiz, C. Belin and D. Astruc, *J. Am. Chem. Soc.*, 2009, **131**, 590–601.

46 W. E. Geiger, *Organometallics*, 2007, **26**, 5738–5765.

47 C. Yu, W. X. Zhang and Z. Xi, *Organometallics*, 2018, **37**, 4100–4104.

48 D. Kumar, M. Deb, J. Singh, N. Singh, K. Keshav and A. J. Elias, *Coord. Chem. Rev.*, 2016, **306**, 115–170.

Appendix:

Table A.1 - Crystallographic tables for compounds described in chapter 2.

Compound reference	[DyCp*(κ^3-BH_4)$_2$(THF)] 2.1	[DyCp*(κ^3-BD_4)$_2$(THF)] 2.2
Chemical formula	$C_{14}H_{31}B_2DyO$	$C_{14}H_{23}B_2D_8DyO$
Formula mass	399.51	407.56
Crystal system	Orthorhombic	Orthorhombic
a/Å	13.980(2)	14.058(8)
b/Å	8.2594(13)	8.280(4)
c/Å	7.8182(11)	7.873(4)
α/°	90	90
β/°	90	90
γ/°	90	90
Unit cell volume/Å^3	902.7(2)	916.4(8)
Temperature/K	200(2)	200(2)
Space group	$Pmn2_1$	$Pmn2_1$
No. of formula units/unit cell, *Z*	2	2
Radiation type	Mo Kα	Mo Kα
Absorption coefficient, μ/mm^{-1}	4.127	4.065
No. of reflections measured	9824	7167
No. of independent reflections	1830	2288
R_{int}	0.0190	0.0157
Final R_1values (I> 2σ(I))	0.0226	0.0146
Final wR_2(F^2) values (I> 2σ(I))	0.0650	0.0359
Final R_1 values (all data)	0.0232	0.0153
Final wR_2(F^2) values (all data)	0.0653	0.0362
Goodness of fit on F^2	1.230	1.075
CCDC number	xxxxxx	xxxxxx

Table A.2 - Crystallographic table for Complex described in Chapter 3

Label	[η^4-Cb^{Ph4}]3.1
Empirical formula	$PdC_{56}H_{40}$
Formula weight	691.33
Temperature/K	202.15
Crystal system	monoclinic
Space group	$P2_1$
a/Å	10.6694(4)
b/Å	16.9322(7)
c/Å	11.1731(4)
α/°	90

β/°	102.3450(10)
γ/°	90
Volume/Å^3	1971.82(13)
Z	29
2Θ range for data collection/°	3.732 to 49.268
Reflections collected	36972
Goodness-of-fit on F^2	1.030
Final R indexes [I>=2σ (I)]	R_1 = 0.0302, wR_2 = 0.0597
Final R indexes [all data]	R_1 = 0.0402, wR_2 = 0.0642
Largest diff. peak/hole / e Å^{-3}	0.30/-0.49
Flack parameter	0.484(12)
CCDC number	xxxxx

Table A.3 - Crystallographic tables for complexes described in Chapter 4.

Label	[DyCb^{trans}(κ$_3$-BH_4)((μ-H)$_2$$BH_4$(Li(THF)$_3$))((μ-H)$_2$$BH_4$(Li(THF)$_2$))]$_\infty$ 4.1	[DyCp*$(BH_4)_2$((μ-H)$_2$$BH_4$(Li(THF)$_3$))] 4.2	[DyCb^{trans}$(THF)_2$(κ^3-BH_4)((μ-H)$_2$$BH_4$Li]$_\infty$ 4.3
Empirical formula	$DyC_{42}H_{80}B_3O_5Si_2Li_2$	$DyC_{22}H_{51}O_3B_3Li$	$DyC_{30}H_{52}B_2O_2Si_2Li$
Formula weight	930.08	567.36	691.17
Temperature/ K	203.15	203.15	203.15
Crystal system	monoclinic	Monoclinic	orthorhombic
Space group	$P2_{1/c}$	Pc	P212121
a/Å	11.356	9.622	10.6971
b/Å	19.677	28.64	16.541
c/Å	24.399	11.55	19.621
α/°	90	90	90
β/°	102	108.15	90
γ/°	90	90	90
Volume/Å^3	5319	3025	3471.6
Z	2	2	2
2Θ range for data collection/°	2.686 to 53.034	1.422 to 50.44	3.22 to 42.27
Reflections collected	98861	29598	15056
Goodness-of-fit on F^2	1.030	1.101	1.012
Final R indexes [I>=2σ (I)]	R_1 = 0.0411, wR_2 = 0.0993	R_1 = 0.0497, wR_2 = 0.0878	R_1 = 0.0330, wR_2 = 0.0613
Final R indexes [all data]	R_1 = 0.0668, wR_2 = 0.1115	R_1 = 0.1148, wR_2 = 0.1058	R_1 = 0.0490, wR_2 = 0.0657
Largest diff. peak/hole / e	1.62/-0.93	0.9/-1.2	0.58/-0.32

$Å^{-3}$			
Flack parameter	n/a	0.49(2)	0.004(13)
CCDC Number	xxxxxx	xxxxx	xxxxxx

Table A.4 - Crystallographic tables for complexes described in Chapter 5

Label	$[K(THF)_6][Dy(HBBN)_4(THF)_2]$ 5.1	$[Dy(HBBN)_2(THF)(\mu\text{-}Cb^{trans})K]_4$ 5.2	$[Dy(HBBN)_2(THF)(\mu\text{-}Cb^{trans})Li(THF)]$ 5.3
Empirical formula	$DyKB_4C_{64}H_{128}O_8$	$[DyKC_{42}H_{68}OB_2Si_2]_4$	$DyLiC_{46}H_{76}O_2B_2Si_2$
Formula weight	1270.56	3457.72	908.41
Temperature/K	203.15	293.15	273.15
Crystal system	triclinic	tetragonal	triclinic
Space group	P1	$P4_2/n$	P-1
a/Å	11.38	24.786(2)	15.20(7)
b/Å	11.58	24.786(2)	17.71(8)
c/Å	14.17	18.053(2)	19.05(8)
α/°	77.95	90	82.87(7)
β/°	79.92	90	89.82(11)
γ/°	77.94	90	89.96(6)
Volume/$Å^3$	1769	11091(2)	5088(39)
Z	2	2	2
2Θ range for data collection/°	2.966 to 49.224	4.312 to 59.714	2.154 to 42.526
Reflections collected	29105	240766	80631
Goodness-of-fit on F^2	1.019	0.999	1.046
Final R indexes [I>=2σ (I)]	$R_1 = 0.0660$, $wR_2 = 0.1773$.	$R_1 = 0.0379$, $wR_2 = 0.0780$	$R_1 = 0.1162$ $wR_2 = 0.2682$.
Final R indexes [all data]	$R_1 = 0.0671$, $wR_2 = 0.1783$	$R_1 = 0.0802$, $wR_2 = 0.0976$	$R_1 = 0.1978$, $wR_2 = 0.3228$.
Largest diff. peak/hole / e $Å^{-3}$	2.53/-0.62	2.30/-0.89	2.23/-1.97
Flack parameter	0.496(5)	n/a	n/a
CCDC Number	xxxxxx	xxxxxx	xxxxxx

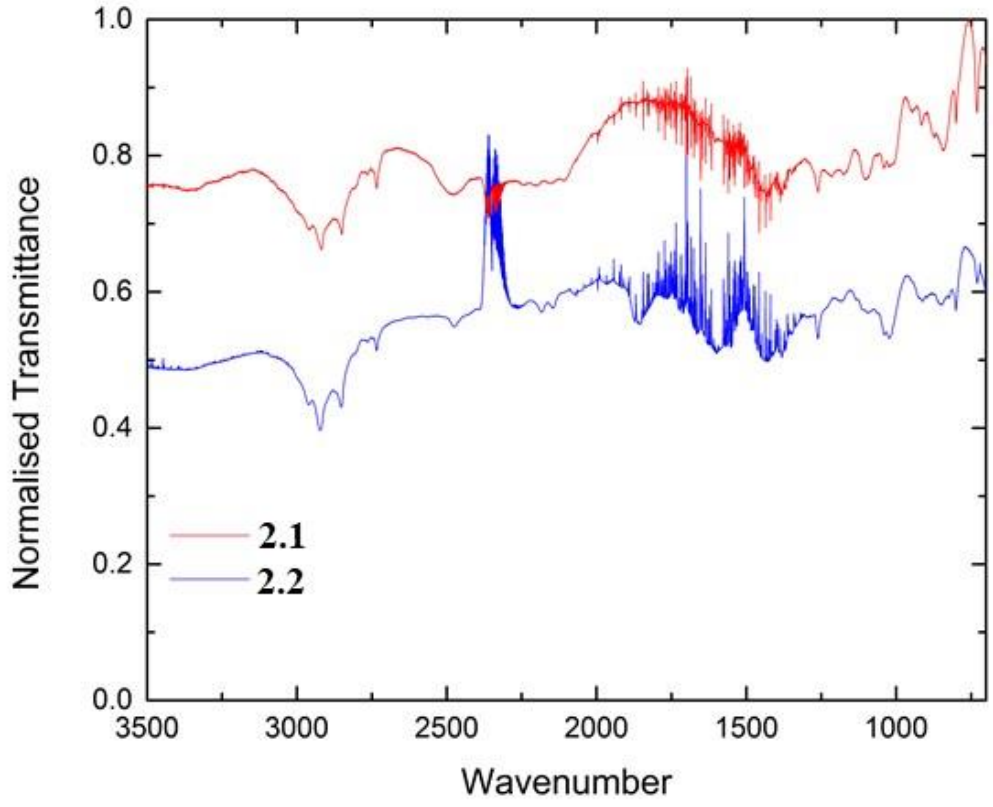

Figure A.1 - FTIR spectra of Compounds **2.1** (**red**) and **2.2** (**blue**) collected under N_2(g) between two transparent NaCl plates.

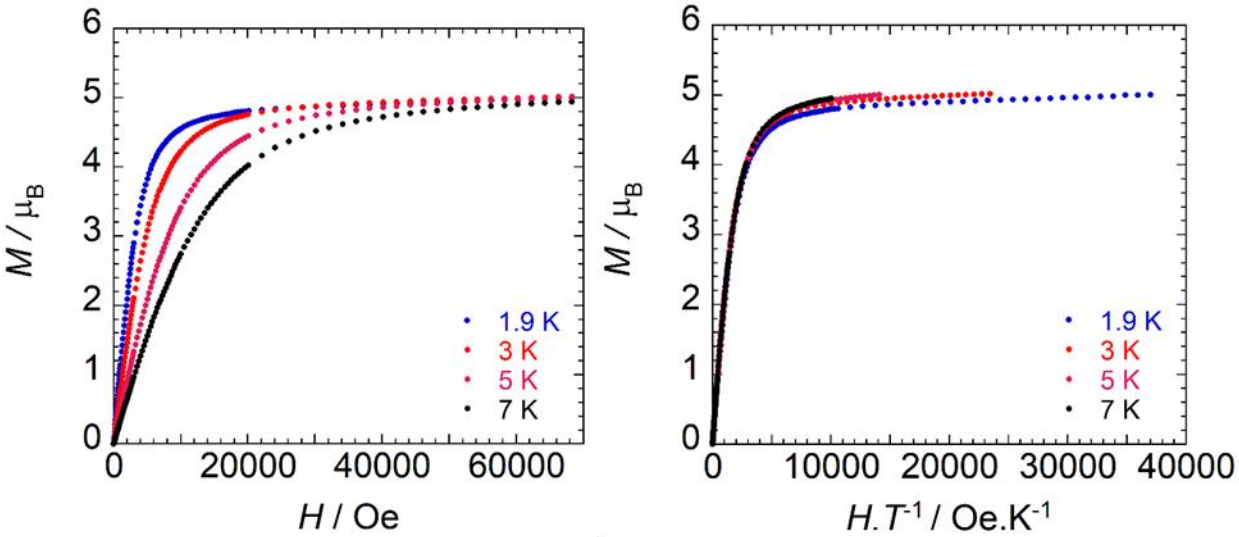

Figure A.2 - Field dependence of the magnetisation and reduced magnetisation of **2.1** at varying temperatures.

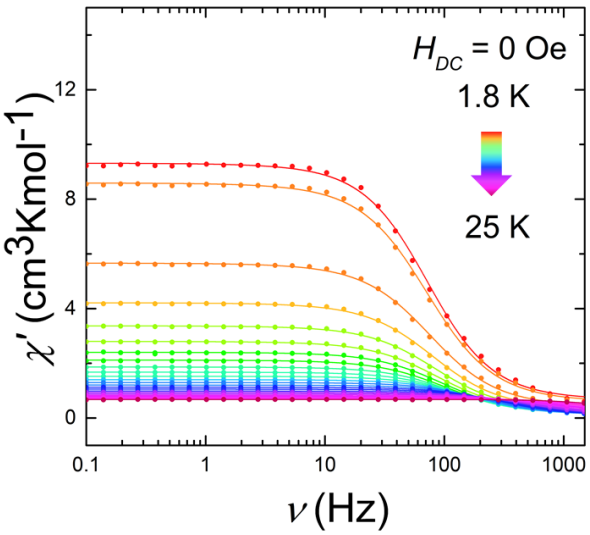

Figure A.3 - Frequency dependence of the in-phase magnetisation of **2.1** under zero field between 1.8 and 25 K. Dots are experimental data and lines are best-fits of the data using the generalised Debye law.

Table A.5 - Best-fit parameters from fitting the in-phase susceptibilities of **2.1** under zero field to the generalised Debye model.

T (K)	χS	χt	α	t (s)
1.8	0.65611	9.31366	0.09892	0.00221
2.0	0.57602	8.59074	0.10973	0.00223
3.0	0.39951	5.66042	0.11195	0.0021
4.0	0.31684	4.20967	0.11139	0.002
5.0	0.26741	3.36746	0.11115	0.00192
6.0	0.22826	2.79841	0.11275	0.00182
7.0	0.20485	2.40111	0.10939	0.00172
8.0	0.17301	2.1168	0.11535	0.00159
9.0	0.16872	1.86337	0.09468	0.00142
10.0	0.15478	1.67423	0.08768	0.00125
11.0	0.14035	1.52312	0.08534	0.00107
12.0	0.12842	1.39949	0.08223	9.15192E-4
13.0	0.11546	1.29348	0.08381	7.73804E-4
14.0	0.11258	1.20213	0.08489	6.55158E-4
15.0	0.10168	1.1239	0.09237	5.4926E-4
16.0	0.10589	1.05453	0.09433	4.70051E-4
17.0	0.13072	0.98548	0.07672	4.09739E-4
18.0	0.12479	0.93728	0.09907	3.40993E-4
19.0	0.16709	0.88828	0.07869	3.09687E-4
20.0	0.18349	0.8449	0.08531	2.60074E-4
21.0	0.24299	0.80278	0.05962	2.34193E-4
22.0	0.27524	0.76654	0.05053	2.00621E-4
23.0	0.31924	0.73326	0.02537	1.67553E-4
24.0	0.35158	0.70192	0.00411	1.3056E-4
25.0	0.34545	0.67562	0.02763	8.73896E-5

T (K)	χS	χt	α	t (s)

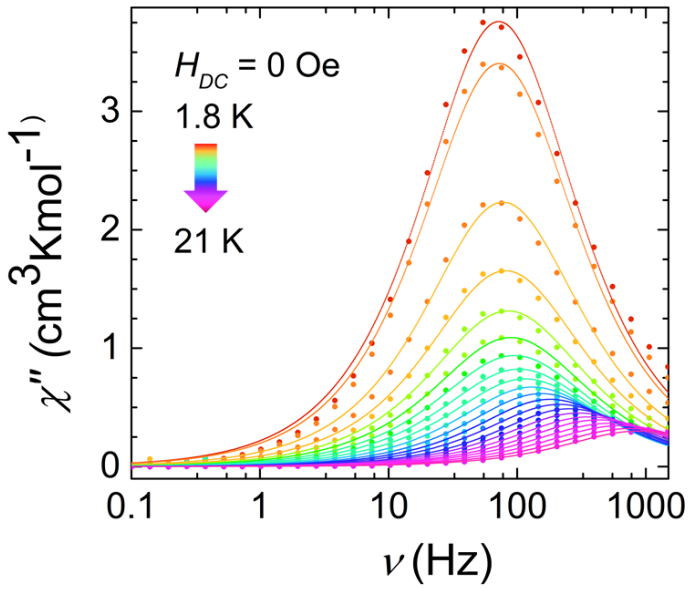

Figure A.4 - Frequency dependence of the out of phase magnetisation of **2.1** under zero field between 1.8 and 21 K. Dots are experimental data and lines are best-fits of the data using the generalised Debye law with parameters described in-text.

Table A.6 - Best-fit parameters from fitting the out-of-phase susceptibilities of **2.1** under zero field to the generalised Debye model.

1.8	5.52	14.58	0.13098	0.00221
2.0	5.93942	14.16058	0.13201	0.00219
3.0	7.34348	12.7565	0.13453	0.00205
4.0	8.0381	12.06009	0.13643	0.00196
5.0	8.45065	11.64935	0.13659	0.00188
6.0	8.72103	11.37873	0.13827	0.00178
7.0	8.91197	11.18803	0.1352	0.00167
8.0	9.05684	11.04316	0.13181	0.00154
9.0	9.16987	10.93013	0.12226	0.00138
10.0	9.25865	10.84135	0.11679	0.00121
11.0	9.33216	10.76783	0.10961	0.00103
12.0	9.38962	10.71038	0.1084	8.84039E-4
13.0	9.43567	10.66433	0.11252	7.46366E-4
14.0	9.4831	10.6169	0.10782	6.23482E-4
15.0	9.51559	10.58441	0.11924	5.29282E-4
16.0	9.54761	10.55239	0.1268	4.39439E-4
17.0	9.57721	10.52279	0.12758	3.68468E-4
18.0	9.60129	10.49871	0.14273	3.03341E-4
19.0	9.62906	10.47094	0.13735	2.5051E-4
20.0	9.66468	10.43532	0.12803	2.12722E-4
21.0	9.69685	10.40315	0.11633	1.80723E-4
22.0	9.73141	10.36859	0.09652	1.51368E-4

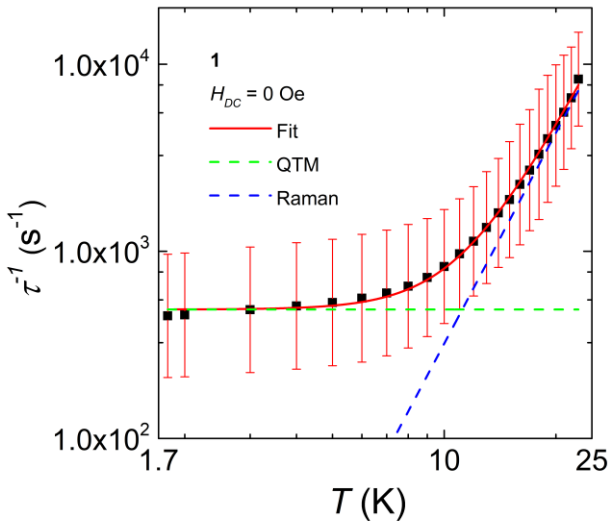

Figure A.5 - Temperature dependence of the relaxation rate of **2.1** extracted from the out-of-phase susceptibilities with zero field between 4.5 and 23 K. Dots are experimental data and lines are best-fits of the data using the generalised Debye law with parameters described in-text. The error bars on the relaxation times have been calculated from the α-parameters of the generalized Debye fits and the log-normal distribution described in reference.[2]

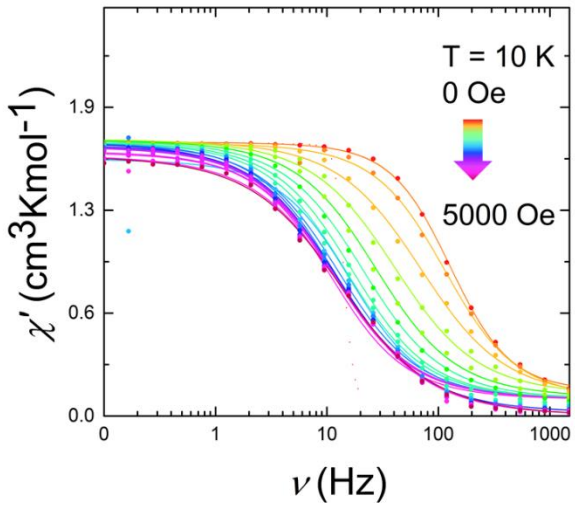

Figure A.6 - Field dependence of the in-phase magnetisation of **2.1** under increasing applied field at 10 K. Dots are experimental data and solid lines are best fits of the data using the generalised Debye law.

Table A.7 - Best-fit parameters from fitting the in-phase susceptibilities of **2.1** under increasing applied field at 10 K to the generalised Debye model. Red values are where parameters had to be fixed to yield physically meaningful values.

H (Oe)	χS	χt	α	t (s)
0	0.14987	1.67579	0.08953	0.00124
200	0.10779	1.67145	0.16304	0.00138
400	0.10795	1.68997	0.23267	0.00227
600	0.12627	1.69458	0.22788	0.00393
800	0.11212	1.69033	0.21121	0.00577
1000	0.1	1.68692	0.21002	0.00754
1200	0.1	1.67935	0.20038	0.00937
1400	0.1	1.67843	0.20614	0.01078
1600	0.1	1.57225	0.16972	0.00983
1800	0.1	1.66958	0.20785	0.01256
2000	0.1	1.67605	0.20164	0.01381
2200	0.1	1.67503	0.24044	0.01271
2400	0.1	1.66056	0.21003	0.01384
2600	0.1	1.65384	0.20848	0.01395
2800	0.1	1.65009	0.2134	0.014
3000	0.1	1.64838	0.21417	0.01411
3500	0.1	1.64838	0.21417	0.01411
4000	0.1	1.61367	0.18703	0.01468
4500	0.1	1.59748	0.2521	0.01204
5000	0.1	1.59402	0.26369	0.01199

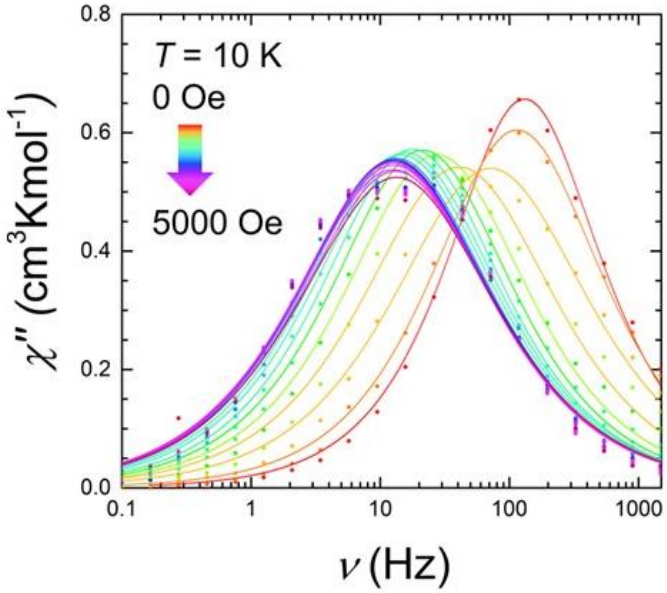

Figure A.7 - Field dependence of the out of phase magnetisation of **2.1** under increasing applied field at 10 K. Dots are experimental data and solid lines are best fits of the data using the generalised Debye law.

Table A.8 - Best-fit parameters from fitting the out-of-phase susceptibilities under increasing applied field at 10 K to the generalised Debye model.

H (Oe)	χS	χt	α	t (s)
0	9.26004	10.83996	0.1169	0.00121
200	9.24102	10.85898	0.18308	0.00138
400	9.233	10.867	0.25697	0.00223
600	9.24291	10.85709	0.24726	0.0039
800	9.24887	10.85113	0.22066	0.00578
1000	9.24267	10.85733	0.21683	0.00748
1200	9.2373	10.8627	0.21929	0.00889
1400	9.22301	10.87548	0.23506	0.01009
1600	9.13026	10.78874	0.24072	0.01102
1800	9.1323	10.78671	0.24631	0.01185
2000	9.12506	10.79394	0.25072	0.01203
2200	9.12545	10.79355	0.25337	0.01237
2400	9.1211	10.7979	0.25675	0.01249
2600	9.12543	10.79358	0.25371	0.01259
2800	9.12698	10.79202	0.25529	0.01262
3000	9.129	10.79	0.25637	0.01275
3500	9.13882	10.78018	0.2536	0.01257
4000	9.13091	10.7881	0.26765	0.01258
4500	9.15218	10.76682	0.2551	0.01207
5000	9.15638	10.76262	0.26335	0.01189

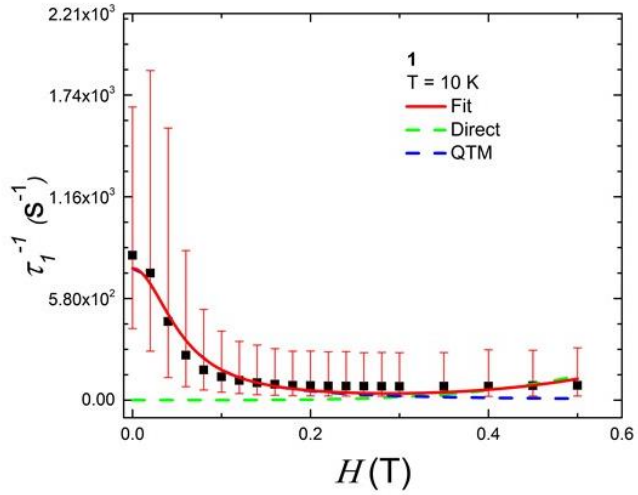

Figure A.8 - Field dependence of the relaxation rate of **2.1** extracted from the out-of-phase susceptibilities at 10 K under increasing applied field. Dots are experimental data and lines are best-fits of the data using the generalised Debye law with parameters described in-text. The error bars on the relaxation times have been calculated from the α-parameters of the generalized Debye fits and the log-normal distribution described in reference.[2]

Table A.9- Phonon frequencies (in cm^{-1}) computed with the optimised crystal structures.

	1	2
	0.000000	0.000000
	0.000000	0.000000
	0.000000	0.000000
	26.850355	26.481339
	34.675907	34.366712
	37.024260	36.644201
	37.997778	38.060181
	47.237411	46.591656
	51.634167	51.004605
	59.685186	58.887839
	63.728924	63.102546
	64.175912	63.361567
	69.390788	68.552200
	72.641898	70.973703
	76.280880	75.181421
	81.412331	80.984850
	87.879575	87.640285
	89.293865	88.102645
	104.045928	99.688328
	105.760994	103.734555
	107.983291	106.594273
	108.843964	107.562939
	109.803637	108.002361
	113.342036	109.277185
	116.185554	114.887724
	118.862645	115.325975
	119.766530	115.600065
	121.926711	116.197683
	122.340202	119.177275
	126.463072	119.850712
	131.473732	126.717219
	140.520266	129.158515
	143.761402	132.842360
	144.372713	140.877842
	148.067343	142.803843
	151.667878	143.723993
	154.213575	146.655557
	154.808802	150.050924
	160.094907	151.094501
	162.766360	152.444001
	165.468062	157.634349
	173.029449	160.456649
	176.772306	164.784604
	178.953174	170.711465
	182.114092	173.497905
	188.613373	174.102965
	189.769202	181.579467
	190.669431	182.581103
	191.603966	183.702475
	196.745264	185.508679
	203.840723	191.504729

	203.906498	191.779834
	205.830428	202.203847
	210.643209	203.463158
	222.833817	203.931185
	226.053697	207.085394
	265.143060	214.673379
	266.430323	217.496143
	269.713294	265.918456
	272.289996	266.106544
	274.254894	269.691949
	275.782136	272.101259
	276.735867	275.480333
	279.518146	275.771209
	291.064430	290.733706
	292.232930	291.812597
	296.638070	296.008408
	297.173280	296.725599
	328.770340	323.849527
	329.480345	327.840754
	388.243892	329.191145
	389.266570	332.433825
	389.847898	340.101965
	402.151075	342.858130
	408.711129	345.246986
	415.353232	353.523270
	425.337476	369.312106
	427.744157	377.949240
	457.052840	389.445227
	463.516135	389.610277
	477.038329	410.190161
	485.127095	411.436717
	541.459156	418.108127
	542.565497	418.212640
	544.608565	430.028337
	544.624997	432.204352
	545.410729	542.669502
	545.826032	543.572728
	558.096567	544.821230
	558.604282	544.920269
	573.270189	546.141160
	573.591315	546.455387
	587.714526	587.474768
	589.260583	588.634376
	617.140023	617.068728
	617.261627	617.200245
	623.642376	623.378136
	624.255791	623.992624
	628.551246	628.264155
	629.287312	629.073230
	656.745490	656.706043
	656.781888	656.729675
	791.594483	791.571716
	793.320598	793.236540
	796.372143	795.894763

	796.435861	796.070964
	800.537148	798.906764
	801.621201	799.690203
	834.992107	800.411879
	835.377300	801.455966
	856.849371	802.869429
	858.699891	803.653781
	898.627033	805.325855
	898.674115	805.994418
	923.884084	813.012906
	924.445895	813.816108
	936.530294	834.946577
	937.690653	835.270549
	939.646572	854.314598
	939.876806	855.054899
	949.192000	856.630353
	949.233656	857.853994
	992.140850	863.769362
	992.333564	864.993288
	1001.363757	867.002650
	1001.590894	867.635193
	1011.306679	875.186935
	1012.590925	875.949903
	1016.978094	897.883920
	1017.205903	897.957202
	1019.579261	898.882860
	1021.689294	898.920066
	1022.738681	908.357468
	1024.667118	909.322660
	1042.777022	924.628998
	1042.985075	925.332877
	1049.033422	936.602517
	1049.046455	937.803451
	1052.430421	939.744145
	1053.526479	939.919649
	1065.323372	949.315208
	1066.547606	949.546200
	1071.483909	992.164510
	1072.046069	992.577496
	1074.057443	1001.503481
	1074.236381	1001.669739
	1081.942784	1011.368374
	1084.072412	1012.719755
	1085.788607	1017.194746
	1086.762952	1017.353669
	1108.494484	1019.646671
	1109.544723	1021.769795
	1152.273689	1022.826317
	1152.612726	1024.680103
	1154.448824	1043.153344
	1154.509604	1043.478456
	1162.712255	1049.118853
	1164.047361	1049.174238
	1181.181852	1052.490172

	1184.219528	1053.619662
	1184.502740	1081.971865
	1186.154185	1084.321291
	1201.536153	1108.747670
	1202.350153	1109.425025
	1216.299849	1152.674653
	1217.949671	1152.820946
	1221.970685	1154.577379
	1223.061892	1154.770222
	1229.430109	1184.556852
	1230.017704	1184.829311
	1238.043296	1201.906144
	1239.404268	1202.044364
	1256.724491	1222.306801
	1256.846038	1223.200678
	1273.551380	1237.641907
	1274.126077	1238.486878
	1281.054508	1280.848443
	1281.158514	1280.995425
	1290.561582	1290.419164
	1290.837612	1290.711137
	1327.070923	1326.983624
	1327.271919	1327.199053
	1347.209181	1347.152503
	1348.415879	1348.313099
	1355.602036	1355.526728
	1356.070064	1356.002320
	1357.792788	1357.755752
	1358.218008	1358.174889
	1365.713418	1365.598226
	1367.548498	1367.460206
	1368.110553	1368.050557
	1372.966176	1372.922603
	1373.604915	1373.550785
	1380.281194	1380.266418
	1382.360734	1382.304996
	1383.651158	1383.587817
	1384.614583	1384.562633
	1385.458549	1385.394205
	1407.889363	1407.852658
	1408.022727	1408.010206
	1409.711633	1409.662604
	1411.575723	1411.526285
	1413.246237	1413.187479
	1414.063494	1413.962922
	1417.053600	1416.937771
	1417.167011	1416.990863
	1422.744799	1422.664619
	1424.470899	1424.425757
	1426.373714	1426.321313
	1426.745171	1426.727871
	1430.023324	1429.963803
	1430.242198	1430.202453
	1430.337638	1430.302045

	1433.920824	1433.865368
	1436.239922	1436.211369
	1437.903500	1437.849819
	1440.491114	1440.400071
	1443.046375	1442.989060
	1447.804312	1447.757853
	1448.463505	1448.424572
	1452.329353	1452.203664
	1454.824797	1454.739049
	1455.051787	1454.981848
	1455.090134	1454.995251
	1458.107349	1457.976935
	1458.294782	1458.246747
	1467.319268	1467.305029
	1467.964299	1467.874726
	1471.685330	1471.597564
	1471.732435	1471.684918
	1481.970969	1481.941058
	1482.188658	1482.151749
	2198.948366	1579.846399
	2200.892523	1581.085856
	2221.564225	1590.029512
	2222.379103	1590.614885
	2256.714722	1644.177331
	2257.084755	1644.465465
	2269.319737	1652.843602
	2269.686871	1652.944626
	2282.208928	1679.880323
	2283.568189	1680.320694
	2308.775867	1695.548136
	2309.147834	1695.813722
	2520.892008	1863.146120
	2522.050483	1863.965236
	2549.382565	1883.569256
	2551.385116	1885.217775
	2900.302031	2900.379271
	2900.731040	2900.808872
	2910.923087	2911.003632
	2911.835030	2911.919415
	2914.119623	2914.223342
	2914.522329	2914.631348
	2915.812575	2915.939613
	2916.283520	2916.420822
	2925.659514	2925.853292
	2925.787950	2926.001827
	2957.274963	2957.275500
	2957.385371	2957.385568
	2962.278320	2962.341095
	2962.459185	2962.528146
	2963.485988	2963.468631
	2963.576896	2963.569143
	2967.129470	2967.090269
	2967.182174	2967.188907
	2968.527845	2968.509402

	2968.674601	2968.670099
	2972.412277	2972.418850
	2972.592129	2972.601224
	2974.804732	2974.775912
	2974.859840	2974.807563
	2978.318665	2978.324096
	2978.441757	2978.469908
	2982.406450	2982.366329
	2982.418458	2982.431733
	3002.897149	3002.873339
	3003.279646	3003.250945
	3006.946025	3006.949646
	3006.979409	3006.983942
	3010.725249	3010.705309
	3010.769791	3010.744619
	3014.533967	3014.513018
	3014.602279	3014.577483
	3021.617183	3021.630332
	3021.676734	3021.680686
	3024.192613	3024.162556
	3024.272660	3024.246687
	3034.210767	3034.214632
	3034.242272	3034.249131
	3043.166159	3043.163449
	3043.234872	3043.236624
	3050.114051	3050.101642
	3050.294714	3050.279660

Table A.10 - CASSCF/RASSI energies and the corresponding g-tensors of the low-lying KD states using the Xray molecular structure of compound **2.1** (in cm^{-1}) upon removing ALL mixing between Dy and ligand's orbitals. Active space of the CASSCF method was CAS(9 in 7). 21×(S=5/2) + 128×(S=3/2) + 130×(S=1/2) roots were mixed by spin-orbit coupling in RASSI.

	Original CASSCF/RASSI calculation (as in Table S25 above)			No mixing between Dy and Ligand orbitals		
Basis set	MB	VDZP	VTZP	MB	VDZP	VTZP
	CASSCF	CASSCF	CASSCF	CASSCF	CASSCF	CASSCF
	0.0	0.00	0.00	0.00	0.00	0.00
	0.0	0.00	0.00	0.00	0.00	0.00
	164.33	153.08	164.33	74.82	74.26	74.24
	164.33	153.08	164.33	74.82	74.26	74.24
	205.63	174.89	185.92	132.59	131.62	131.59
	205.63	174.89	185.92	132.59	131.62	131.59
	225.97	252.91	262.07	199.63	198.63	198.59
	225.97	252.91	262.07	199.63	198.63	198.59
	273.52	301.47	309.78	270.20	269.46	269.42
	273.52	301.47	309.78	270.20	269.46	269.42
	342.53	348.33	357.85	340.79	340.75	340.71
	342.53	348.33	357.85	340.79	340.75	340.71
	415.84	439.35	451.18	428.40	428.58	428.52
	415.84	439.35	451.18	428.40	428.58	428.52
	444.94	498.80	508.06	452.92	453.47	453.41

	444.94	498.80	508.06	452.92	453.47	453.41
	3462.23	3657.85	3639.95	3411.11	3410.86	3410.85
	3462.23	3657.85	3639.95	3411.11	3410.86	3410.85
	…	…	…	…	…	…
	Main values of the g-tensor in low-lying states (gX, gY, gZ)					
KD-1	0.0012	0.0144	0.0115	0.0020	0.0021	0.0021
	0.0024	0.0262	0.0202	0.0027	0.0029	0.0029
	19.7719	19.7490	19.7618	19.8461	19.8442	19.8441
KD-2	0.0986	10.1605	10.0390	0.0779	0.0809	0.0809
	0.1075	9.6062	9.6960	0.0985	0.1023	0.1024
	18.0959	1.4184	1.3747	17.1118	17.1075	17.1074
KD-3	1.3576	8.7239	8.4816	0.4361	0.4398	0.4399
	3.4839	8.0390	8.2694	0.5265	0.5351	0.5353
	13.3757	2.0440	1.9604	14.3241	14.3212	14.3211
KD-4	1.6489	0.2740	0.4443	0.9194	0.9260	0.9263
	2.8726	0.7790	0.5266	1.6653	1.6830	1.6836
	10.7336	14.9644	15.1898	11.5232	11.5205	11.5203

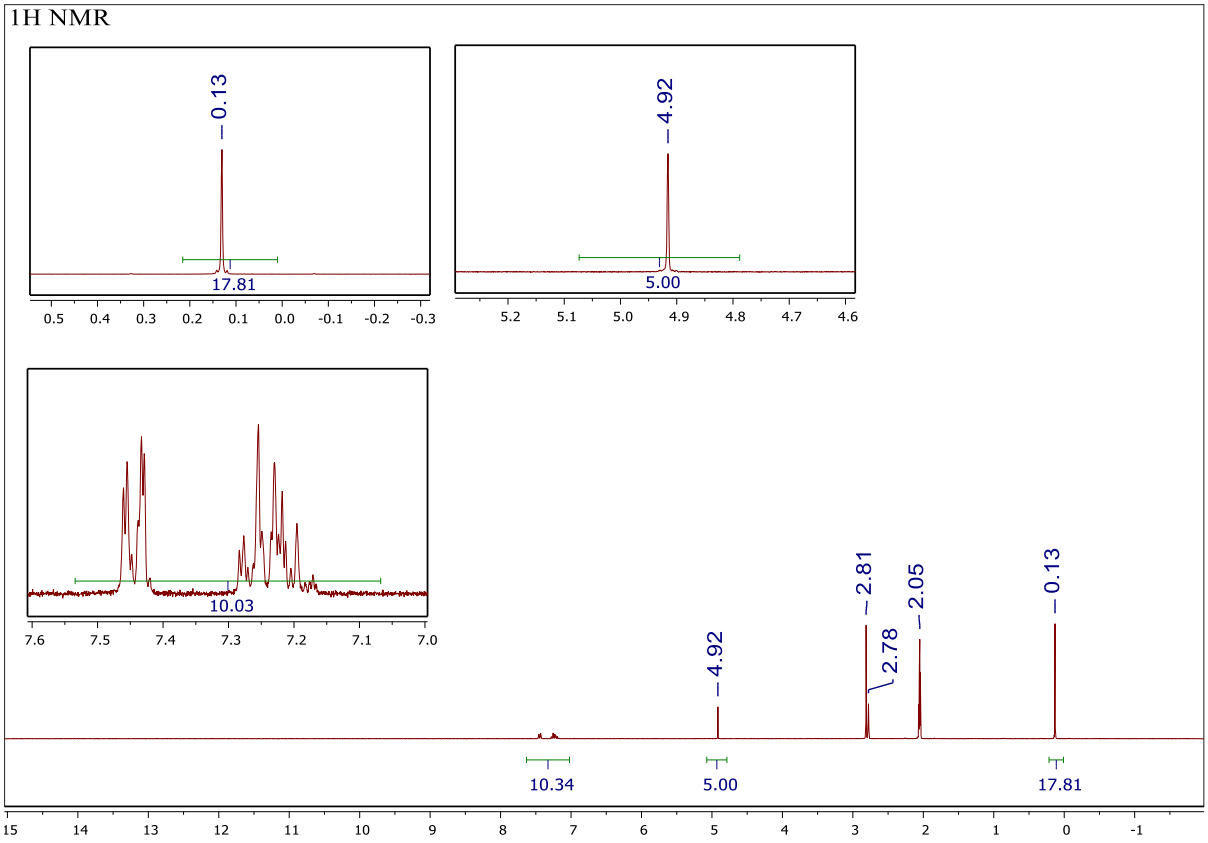

Figure A.9 - ^{1}H NMR of [CoCpCb^{trans}] in CD_3CO after purification by column chromatography. Insets highlight the single Si-Me$_3$ and Cp-H resonances (0.13 and 4.92 ppm respectively), indicating purity. The 10:18:5 integration matches the expected formula [Co(C_5H_5)(*trans*-C_4($SiMe_3$)$_2$$Ph_2$)]. Peaks between 2.81 – 2.05 ppm are due to solvent.

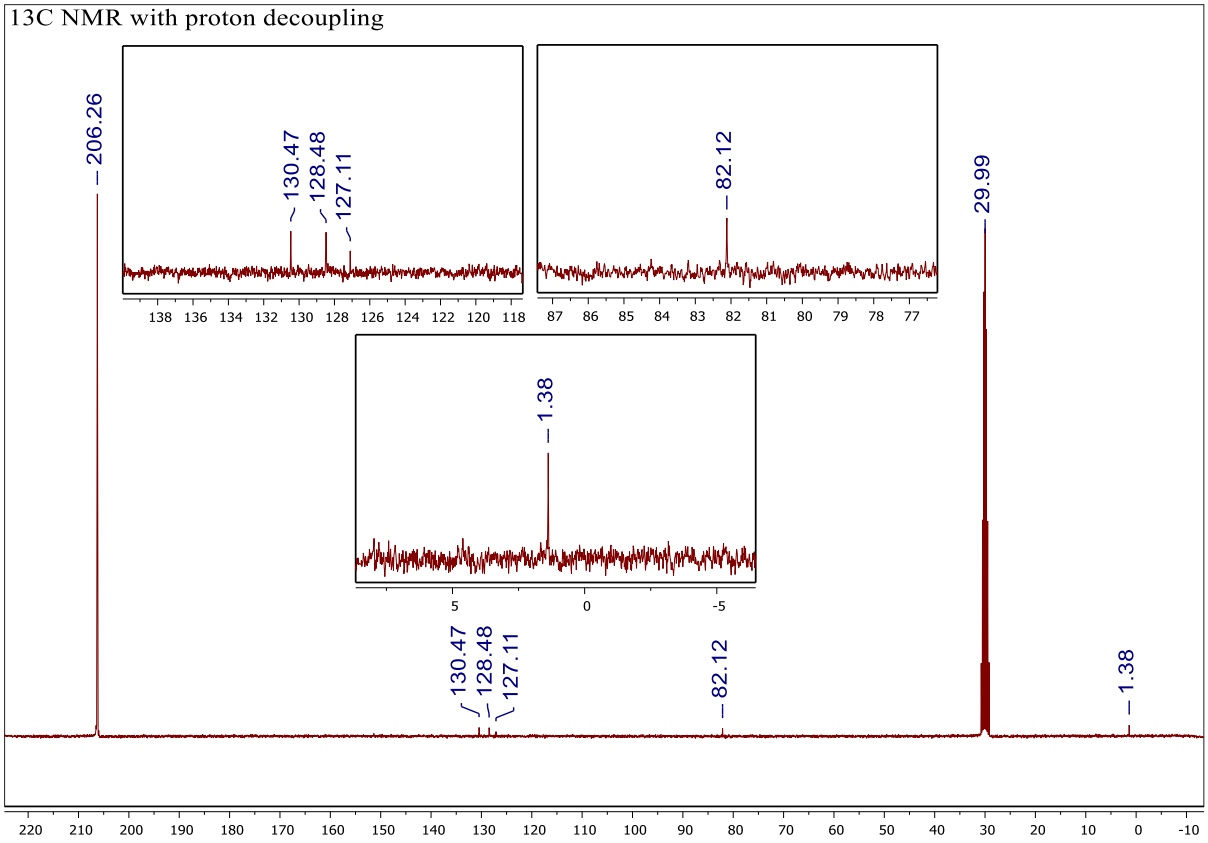

Figure A.10 - ^{13}C NMR of [CoCpCb^{trans}] in CD_3CO after purification by column chromatography. Insets highlight the three phenyl resonances (C_{ortho} = 130.47 ppm, C_{meta}= 128.48 ppm, C_{para} = 127.11 ppm,) single Cp resonance (82.12 ppm) and single $SiMe_3$ resonance (1.38 ppm). These assignments match the expected formula [Co(C_5H_5)(*trans*-$C_4(SiMe_3)_2Ph_2$)].

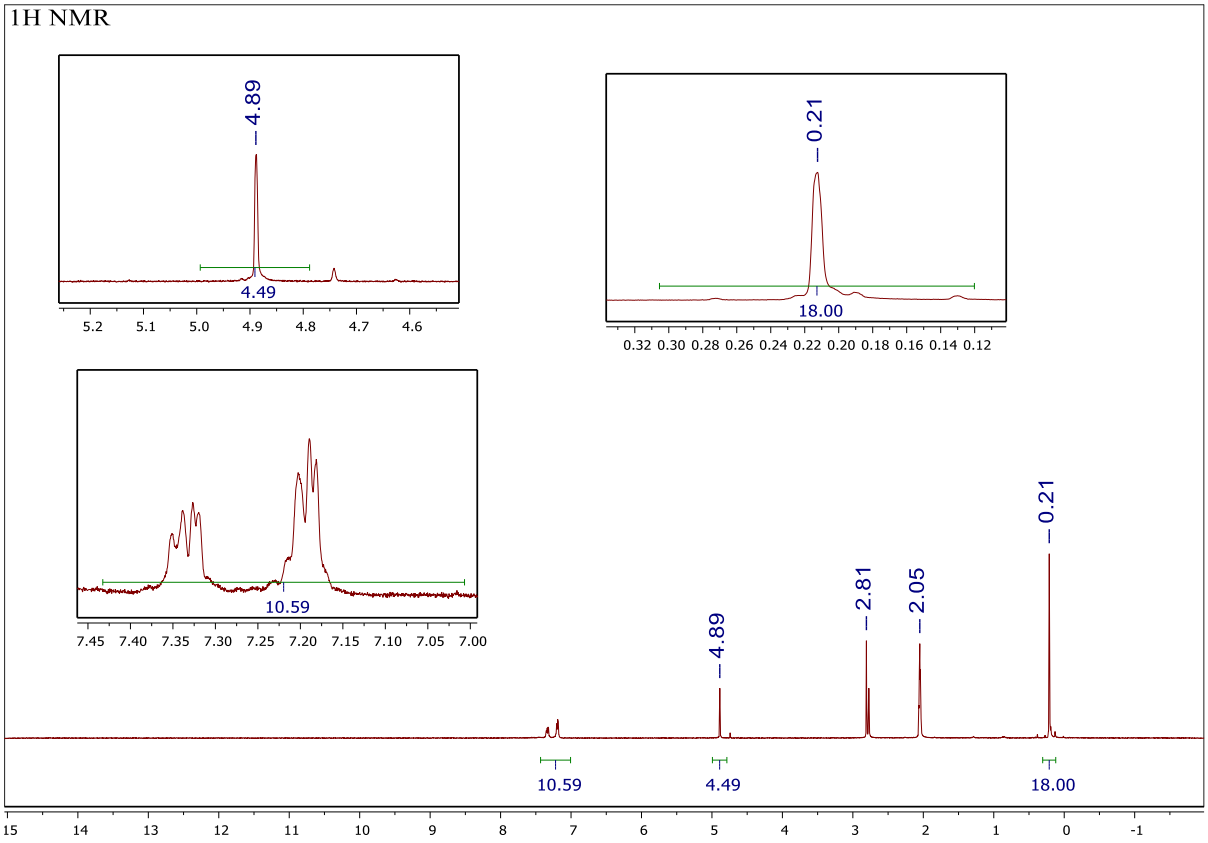

Figure A.11 - ^{1}H NMR of [CoCpCb^{cis}] in CD_3CO after purification by column chromatography. Insets highlight the single Si-Me$_3$ and Cp-H resonances (0.21 and 4.89 ppm respectively), indicating purity. The 10:18:5 integration matches the expected formula [Co(C_5H_5)(*cis*-$C_4(SiMe_3)_2Ph_2$)]. Peaks between 2.81 – 2.05 ppm are due to solvent.

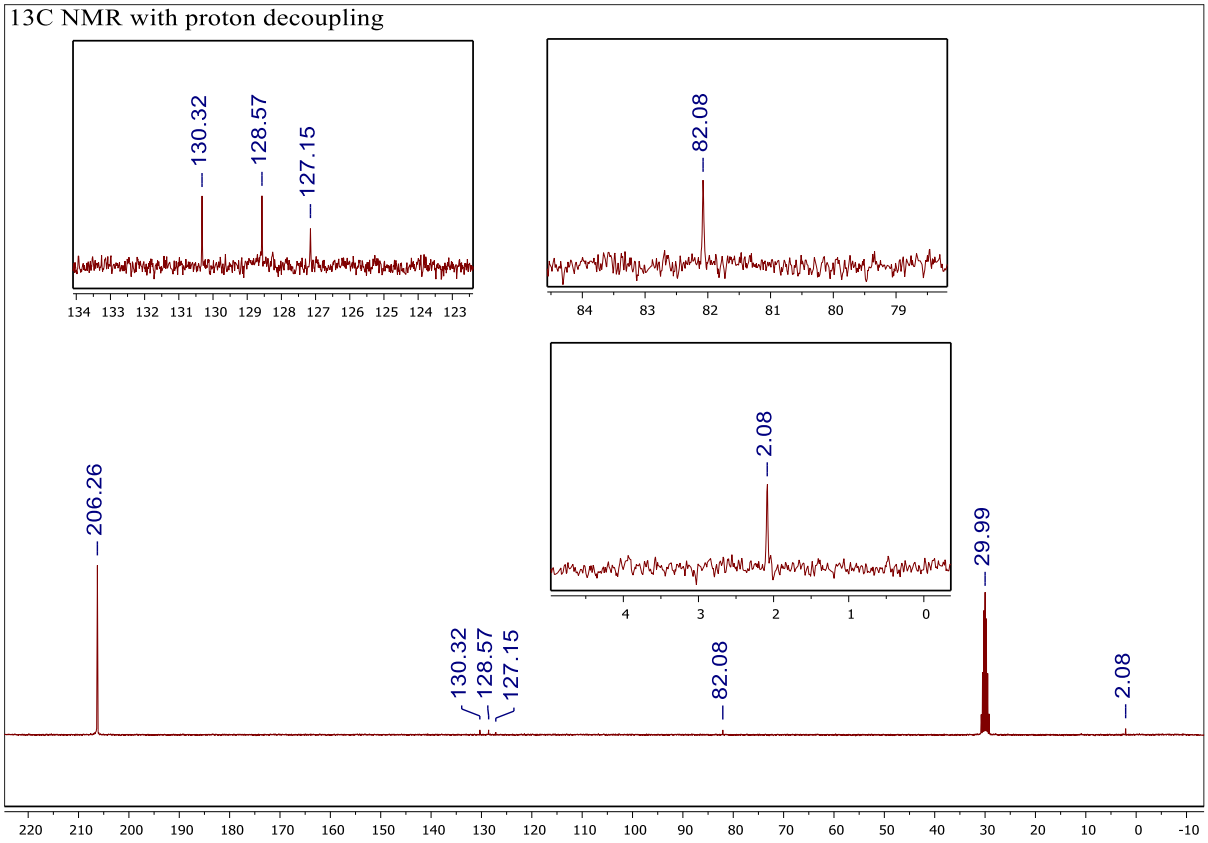

Figure A.12 - ^{13}C NMR of [CoCpCb^{cis}] in CD_3CO after purification by column chromatography. Insets highlight the three phenyl resonances (C_{ortho} = 130.32 ppm, C_{meta}= 128.57 ppm, C_{para} = 127.15 ppm,) single Cp resonance (82.08 ppm) and single $SiMe_3$ resonance (2.02 ppm). These assignments match the expected formula [$Co(C_5H_5)$(*cis*-$C_4(SiMe_3)_2Ph_2$)].

American Physical Society Reuse and Permissions License

10-Mar-2022

This license agreement between the American Physical Society ("APS") and Chris Bamforth ("You") consists of your license details and the terms and conditions provided by the American Physical Society and SciPris.

Licensed Content Information

License Number:	**RNP/22/MAR/051291**
License date:	10-Mar-2022
DOI:	10.1103/PhysRev.127.2058
Title:	Theoretical Investigation of Some Magnetic and Spectroscopic Properties of Rare-Earth Ions
Author:	A. J. Freeman and R. E. Watson
Publication:	Physical Review
Publisher:	American Physical Society
Cost:	USD $ 0.00

Request Details

Does your reuse require significant modifications: No

Specify intended distribution locations:	Canada
Reuse Category:	Reuse in a thesis/dissertation
Requestor Type:	Student
Items for Reuse:	Figures/Tables
Number of Figure/Tables:	1
Figure/Tables Details:	Radial probability function for Gadolinium (iii) ion
Format for Reuse:	Print and Electronic
Total number of print copies:	Up to 1000

Figure A.13 – Permission to reproduce **Figure 1.4** from publisher.

Thank you for your order!

Dear Dr. Christopher Bamforth,

Thank you for placing your order through Copyright Clearance Center's RightsLink® service.

Order Summary

Licensee:	Dr. Christopher Bamforth
Order Date:	Mar 10, 2022
Order Number:	5265510923058
Publication:	Trends in Chemistry
Title:	Magnetic Axiality: Design Principles from Molecules to Materials
Type of Use:	reuse in a thesis/dissertation
Order Total:	0.00 USD

View or print complete details of your order and the publisher's terms and conditions.

Sincerely,

Copyright Clearance Center

Figure A.14 – Permission to reproduce **Figure 1.7** from publisher.

Thank you for your order!

Dear Dr. Christopher Bamforth,

Thank you for placing your order through Copyright Clearance Center's RightsLink® service.

Order Summary

Licensee:	Dr. Christopher Bamforth
Order Date:	Mar 10, 2022
Order Number:	5265511187989
Publication:	Angewandte Chemie International Edition
Title:	Shining New Light on Multifunctional Lanthanide Single-Molecule Magnets
Type of Use:	Dissertation/Thesis
Order Total:	0.00 USD

View or print complete details of your order and the publisher's terms and conditions.

Sincerely,

Copyright Clearance Center

Figure A.15 – Permission to reproduce **Figure 1.8** from publisher.